

**NASA TECHNICAL
MEMORANDUM**

NASA TM X-73931

NASA TM X-73931

(NASA-TM-X-73931) THERMAL DESIGN AND
ANALYSIS OF A HYDROGEN-BURNING WIND TUNNEL
MODEL OF AN AIRFRAME-INTEGRATED SCRAMJET
(NASA) 83 p HC A05/MF A01

CSCL 21A

N77-15045

G3/07 Unclass
59666

THERMAL DESIGN AND ANALYSIS OF A HYDROGEN-BURNING
WIND TUNNEL MODEL OF AN AIRFRAME-
INTEGRATED SCRAMJET

by

Robert W. Guy

James N. Mueller

Shimer Z. Pinckney

Louise P. Lee



This informal documentation medium is used to provide accelerated or special release of technical information to selected users. The contents may not meet NASA formal editing and publication standards, may be revised, or may be incorporated in another publication.

**NATIONAL AERONAUTICS AND SPACE ADMINISTRATION
LANGLEY RESEARCH CENTER, HAMPTON, VIRGINIA 23665**

1. Report No. NASA TM X-73931		2. Government Accession No.		3. Recipient's Catalog No.	
4. Title and Subtitle THERMAL DESIGN AND ANALYSIS OF A HYDROGEN-BURNING WIND TUNNEL MODEL OF AN AIRFRAME- INTEGRATED SCRAMJET				5. Report Date	
				6. Performing Organization Code 37.450	
7. Author(s) R. W. Guy; J. N. Mueller; S. Z. Pinckney; L. P. Lee				8. Performing Organization Report No.	
				10. Work Unit No. 505-05-41-09	
9. Performing Organization Name and Address NASA Langley Research Center Hampton, VA 23665				11. Contract or Grant No.	
				13. Type of Report and Period Covered Technical Memorandum	
12. Sponsoring Agency Name and Address National Aeronautics and Space Administration Washington, D.C. 20546				14. Sponsoring Agency Code	
15. Supplementary Notes This is the final release of special information not suitable for formal publication which serves the following need: presents detailed thermal design information.					
16. Abstract An aerodynamic model of a hydrogen-burning, airframe-integrated scramjet engine has been designed, fabricated, and instrumented. This model is to be tested in an electric-arc-heated wind tunnel at a stream energy level duplicating Mach 7 flight at an altitude of 35.39 km (116,094 ft.) but with an inlet Mach number of 6 simulating precompression on an aircraft undersurface. The scramjet model is constructed from oxygen-free, high-conductivity copper and is a heat sink design except for water cooling in some critical locations. The model is instrumented for pressure, surface temperature, heat transfer rate, and thrust measurements. This report describes the analysis techniques which were used in the thermal design of the scramjet engine model. Calculated flow properties, heat transfer rates, and surface temperature distributions along the various engine components are included for the conditions stated above. For some components, estimates of thermal strain are presented which indicate significant reductions in plastic strain by selective cooling of the model. These results show that the 100 thermal cycle life of the engine was met with minimum distortion while staying within the 2669 N (600 lbf) engine weight limitation and while cooling the engine only in critical locations. Finally, the design of the hydrogen fuel injection system for the struts is presented in an appendix.					
17. Key Words (Suggested by Author(s)) <u>Fluid Mechanics and Heat Transfer</u> Scramjet engines Thermal design			18. Distribution Statement Unclassified - Unlimited		
19. Security Classif. (of this report) Unclassified		20. Security Classif. (of this page) Unclassified		21. No. of Pages 81	22. Price* \$5.00

THIS PAGE IS
OF HIGH QUALITY

THERMAL DESIGN AND ANALYSIS OF A HYDROGEN-BURNING
WIND TUNNEL MODEL OF AN AIRFRAME-
INTEGRATED SCRAMJET

Robert W. Guy, James N. Mueller,
Shimer Z. Pinckney, and Louise P. Lee

Langley Research Center

SUMMARY

An aerodynamic model of a hydrogen-burning, airframe-integrated scramjet engine has been designed, fabricated, and instrumented. This model is to be tested in an electric-arc-heated wind tunnel at a stream energy level duplicating Mach 7 flight at an altitude of 35.39km (116,094 ft) but with an inlet Mach number of 6 simulating precompression on an aircraft undersurface. The scramjet model is constructed from oxygen-free, high-conductivity copper and is a heat sink design except for water cooling in some critical locations. The model is instrumented for pressure, surface temperature, heat transfer rate, and thrust measurements.

This report describes the analysis techniques which were used in the thermal design of the scramjet engine model. Calculated flow properties, heat transfer rates, and surface temperature distributions along the various engine components are included for the conditions stated above. For some components, estimates of thermal strain are presented which indicate significant reductions in plastic strain by selective cooling of the model. These results show that the 100 thermal cycle life of the engine was met with minimum distortion while staying within the 2669 N (600 lbf) engine weight limitation and while cooling the engine only in critical locations. Finally, the design of the hydrogen fuel injection system for the struts is presented in an appendix.

INTRODUCTION

Preliminary analytical performance studies (ref. 1) have shown the airframe-integrated scramjet to be a viable candidate for propelling hypersonic aircraft. A more recent, but still preliminary, thermal-structural design and analysis study of a lightweight engine confirms that this scramjet concept is viable from both a structural weight and cooling requirement standpoint (refs. 2-3).

While such general performance studies continue and lend credence to the

airframe-integrated concept, basic research is also progressing on the various engine components such as the inlet (refs. 4-6), the fuel injection struts and the combustor (refs. 7-10), and the nozzle (ref. 11). The next step in the evolution of this scramjet engine is the testing in ground facilities of a hydrogen-burning model which uses the knowledge gained in the component tests. Such a model has been designed, fabricated, and instrumented. The thermal design and analysis of this model is the subject of this report.

Initial testing will be performed at conditions duplicating those in front of a scramjet mounted on the undersurface of an aircraft flying at a Mach number of 7 and a dynamic pressure of 19.0 kN/m^2 (397 lbf/ft^2). The test stream of NASA Langley's Scramjet Test Facility (ref. 12) has a total enthalpy duplicating a flight Mach number of 7. To simulate the compression caused by the aircraft forebody, the facility test stream Mach number is 6 and the dynamic pressure is 34.9 kN/m^2 (729 lbf/ft^2). The scramjet model designed for this Mach 7 ground facility environment is largely heat sink to avoid the complications and costs associated with either flightweight cooling concepts or total cooling of non-flightweight structures.

An earlier conceptual study (ref. 1) has resulted in aircraft scramjet engines typically having 3 to 6 side-by-side modules of the type discussed in this report. Depending upon the vehicle envisioned, the present model may represent performance of a full scale module for smaller vehicles or performance of a subscale module for larger vehicles.

SYMBOLS AND NOMENCLATURE

A	cross sectional area
B	fraction of scramjet throat area blocked by fuel injection struts
c	plate half-width in thermal stress equation, see eq. (6)
C_d	orifice discharge coefficient
C_f	skin friction coefficient
c_p	specific heat at constant pressure
d	orifice diameter
D_H	hydraulic diameter
dp	cooling channel depth
E	modulus of elasticity

g	effective gap width fueled by a row of orifices
h	static enthalpy
h_{fi}	film coefficient of heat transfer, see eq. (1)
H	total enthalpy
HT	engine height
k	thermal conductivity
l	distance between fuel injection orifices is plane perpendicular to cowl
\dot{m}	mass flow rate
M	Mach number
N_f	cycles to failure
N_{Pr}	Prandtl number
N_{Re}	Reynolds number
n	number of orifices per fuel injector row
p	pressure
q	dynamic pressure
\dot{q}	heat transfer rate
R	specific gas constant
RA	reduction in area
s	surface distance from leading edge
T	temperature
V	velocity
w	cooling channel width
WD	engine width
x	axis parallel to free stream flow (See fig. 2.)
y	axis perpendicular to free stream flow (See fig. 2.)

z	axis perpendicular to free stream flow and y axis (fig. 2)
α	coefficient of thermal expansion
β	shock wave angle
γ	ratio of specific heat at constant pressure to specific heat at constant volume
$\Delta\epsilon_t$	total strain range
δ	downflow angle behind a swept oblique shock
ϵ	strain
η	efficiency
θ	effective aircraft angle-of-attack (assuming conical flow)
μ	coefficient of viscosity
ρ	density
σ	stress
ϕ_f	fuel equivalence ratio

Superscripts

* sonic condition

Subscripts

a	air
act	actual
av	average
b	bulk
c	refers to engine geometric capture area
calc	calculated
cl	coolant
comb	scramjet combustor
cs	cross section

el	elastic
f	fuel
fi	film
H ₂	hydrogen
in	water in
inlet	scramjet inlet
KE	kinetic energy
le	leading edge
min	minimum
max	maximum
n	normal to leading edge
noz	scramjet nozzle
or	orifice
out	water out
pl	plastic
r	recovery
t,l	tunnel stagnation condition
t,f	fuel stagnation condition
tl	total
u	refers to ultimate tensile strength
w	wall condition
x	in x - direction
y	in y - direction
∞	free stream ahead of aircraft
1	upstream of scramjet inlet
2	engine throat or inlet exit
3	combustor exit
4	nozzle exit

MODEL DESCRIPTION AND DESIGN

General Description

The modular scramjet engine concept for effective integration with the aircraft undersurface has been presented in reference 1. A photograph of the concept is shown in figure 1 where the various engine components are labeled.

The subscale model of this scramjet shown in figures 2 and 3 has an inlet height of 20.32 cm (8 in.), an inlet width of 16.26 cm (6.4 in.), and an overall length of 151.1 cm (59.5 in.). Internal mold lines were obtained primarily from reference 5 for the inlet, from reference 1 for the combustor, and from a two-dimensional nozzle design program for the internal upper surface of the nozzle. The sidewall leading edges and the fuel injection struts are swept 48° relative to the flow ahead of the inlet and the cowl does not begin until the 55.37 cm (21.8 in.) engine station. The swept sidewall and strut leading edges cause downward flow to spill from the inlet. The amount of downward flow increases with decreasing Mach number, thus promoting engine starting at the lower Mach numbers. The engine aerodynamic contraction ratio is expected to be between 7 and 8 for the Mach 6 inlet condition (ref. 6) in the Scramjet Test Facility. The hydrogen fuel is injected perpendicular to the flow from each side of the three swept fuel injection struts (see the Appendix). The combustor exit-to-aerodynamic throat area ratio is 5.21 and the scramjet nozzle exit-to-inlet area ratio (geometric) is one with a proposed nozzle extension allowing this ratio to be increased to 2.8 (ref. 12).

The model is designed to allow substitution of components which vary in internal shape (fig. 3). For instance, the inlet, combustor, nozzle, and fuel injection struts could each be replaced without affecting the other components. Thus, this scramjet model can serve as a test bed for various engine component designs without having to completely rebuild the engine.

Parameters that are to be measured on the internal surfaces of this model are pressure, temperature, and heat transfer rate. In addition, total engine thrust will be measured with a one-component force balance. Later tests will include flow field surveys to measure pitot and static pressures and model exhaust gas composition. This survey data will also be used to determine the mass flow rate of the engine exhaust.

Design Constraints

The design constraints placed on the scramjet engine model were the following:

- (1) The model had to withstand at least 100 cycles (tests) of 30 seconds duration in the Scramjet Test Facility flow environment with minimum distortion.

- (2) Active cooling was to be avoided wherever possible, i.e., a completely heat sink model was most desirable. This approach was attractive since model construction would be less complex, instrumentation would be easier to install, and the model would be less expensive if coolant passages were absent.
- (3) Model weight had to be kept below 2669 N (600 lbf) to avoid over-taxing the model support and injection mechanism.

Materials Selection

In selecting the scramjet model construction material, the material performance parameters considered to be most important were fatigue life and distortion. In the selection procedure, the rating of ductile materials as outlined in reference 13 was not performed in detail, but the logic was employed to the extent possible with available property data.

The materials selection problem was approached with the knowledge that the dominant loading would be thermal. Thus, the principle of elastic strain invariance (ref. 13) was used with elastic strains being estimated and then assumed to be equal to the true total strain developed. Therefore, a primary objective was to minimize temperature differences where the structure was restrained and to minimize and linearize gradients (each reduces thermal strain) as well as to keep temperatures as low as possible. This approach tends to increase cycle life, minimize distortion, and maintain high strength. Thus, the required material should have a high ρC_p product to keep temperatures low and a high thermal conductivity to minimize thermal gradients. These considerations led to the choice of oxygen-free, high conductivity copper as the model material. The high thermal conductivity of copper was deemed especially important for leading edge regions and in areas where local hot spots could occur. Also, in the event that other areas might require cooling, less space could be devoted to cooling passages (because of the high thermal conductivity of copper) with more space thus available for instrumentation.

One problem with copper is its relatively low strength. The strength decreases severely at high temperature levels or if the copper must be annealed (as in a brazing cycle to install water tubes). Therefore, upon receipt of the oxygen-free, high-conductivity copper for the scramjet model, tensile tests were made at 295 K (531 R) on the as-received copper and on a specimen of the copper which had been annealed by undergoing a typical brazing cycle (temperature as high as 1117 K (2010 R)). The 0.2% offset yield strength of the as-received copper was found to be about 241.3 MN/m^2 (35,000 psi) while that of the annealed copper was 26.2 MN/m^2 (3800 psi). This is in essential agreement with reference 14 which presents properties of oxygen-free, high-conductivity copper. The stress-strain curves for the two specimens which were tested are shown in figure 4.

Although the strength of the annealed copper is very low, copper was felt to be the proper material for the scramjet model application for two reasons:

- (1) the dominance of thermal loading, and

- (2) the satisfactory performance of annealed copper under more severe conditions reported in reference 15.

Temperature and plastic strain distributions on the strut tested in reference 15 are shown in figure 5. Although the temperatures and plastic strains are large, the strut was undamaged and free of significant distortion after the 20 thermal cycles to which it was exposed.

Wall Thickness Sizing

The primary constraints on the wall thicknesses of the various engine components were the model weight limitation of 2669 N (600 lbf) and, as a first step to avoid cooling, a guideline to maintain internal surface temperatures below the approximate 667 K (1200 R) annealing temperature of the copper. In addition, drag resulting from increased frontal area exposed to the flow tended to limit the maximum thickness of engine components such as the cowl. At the opposite extreme, potential warpage problems limited the minimum thicknesses of the various engine components.

Calculations using the high heating rates in the combustor indicated that a basic wall thickness of 1.91 cm (0.75 inch) would maintain surface temperature below the 667 K (1200 R) limit. A one-dimensional, transient heat transfer analysis (ref. 16) was used in deriving this wall thickness. With this guideline, weight became the primary concern and reductions in wall thickness were permitted in regions of lower heating rates.

The actual mechanical design of the scramjet model included thin leading edges, supportive bulkheads, and other necessary mechanical design items which precluded strict adherence to uniform wall thickness (figs. 2 and 3). This factor as well as the need to determine temperature levels, thermal gradients, and approximate thermal strains indicated the need for an in-depth thermal analysis of the final mechanical design of the scramjet engine model.

THERMAL ANALYSIS TECHNIQUES

Estimates of cycle life (ref. 17) and plastic deformation, or distortion, of various engine components requires a knowledge of total strain range, plastic strain, and the temperature-dependent mechanical properties of oxygen-free, high-conductivity copper (ref. 14). Since the scramjet model loading was predominantly thermal, the principle of elastic strain invariance (ref. 13) was used to estimate the total strain. In this approach, the total strain was calculated using an elastic technique (ref. 18) for thermal stresses on a plate subjected to a nonlinear temperature distribution. To obtain the required temperature distribution along each engine component, the transient, finite-difference heat transfer program of reference 16 was applied to thermal models of the various engine components. This computer program required as input the aerodynamic heating rates and recovery temperatures along the engine components. These parameters were obtained using the integral boundary layer technique of

reference 19. To calculate the aerodynamic heating rates, detailed inviscid flow properties were required along the engine internal surfaces. These properties were obtained using separate computer programs for the inlet (ref.5), the combustor (ref. 15) and the nozzle (ref. 20). The calculation of the flow through the inlet also required a knowledge of properties in the facility test stream which was obtained using a method from reference 21. The following sections describe the techniques listed above in more detail.

Aerodynamic Heating

Tunnel environment.- The Scramjet Test Facility (ref. 12) uses an electric arc to heat the air and features a two-dimensional, contoured hot flow nozzle surrounded on the sides and bottom by cooler air flow (hot-core concept, ref. 22) as shown in figure 6. This scheme permits maximum model size without flow blockage while minimizing the power required to heat the hot-core to the Mach 7 total enthalpy required for the propulsion tests.

Typical tunnel stagnation chamber conditions are:

$$p_{t,1} = 3.04 \text{ MN/m}^2 \quad (30 \text{ atm})$$

$$T_{t,1} = 2222 \text{ K} \quad (4000 \text{ R})$$

$$H_{t,1} = 2.57 \text{ MJ/kg} \quad (1104 \text{ Btu/lbm})$$

With the assumption of equilibrium flow through the tunnel nozzle, test stream properties at the nozzle exit (ahead of the engine inlet) were calculated using the computer program described in reference 21 and are listed below.

$$M_1 = 6.0$$

$$p_1 = 1.39 \text{ kN/m}^2 \quad (29 \text{ lbf/ft}^2)$$

$$T_1 = 312 \text{ K} \quad (562 \text{ R})$$

$$\rho_1 = .0155 \text{ kg/m}^3 \quad (3.01 \times 10^{-5} \text{ slugs/ft}^3)$$

$$V_1 = 2123 \text{ m/s} \quad (6964 \text{ ft/sec})$$

$$h_1 = 0.314 \text{ MJ/kg} \quad (135 \text{ Btu/lbm})$$

$$\gamma_1 = 1.4$$

$$q_1 = 34.9 \text{ kN/m}^2 \quad (729 \text{ lbf/ft}^2)$$

$$N_{Re,1} = 1.73 \times 10^6/m \quad (5.27 \times 10^5/ft.)$$

These identical flow properties would occur at the inlet if the engine were mounted on an aircraft flying at the following conditions:

$$\begin{aligned} M_\infty &= 7.0 \\ \text{Altitude} &= 35.39 \text{ km} \quad (116094 \text{ ft.}) \\ \theta &= 7.67^\circ \\ q_\infty &= 19.0 \text{ kN/m}^2 \quad (397 \text{ lbf/ft}^2) \end{aligned}$$

In order to better simulate the viscous state of the flow that would exist on a full-size flightweight engine, boundary layer trips can be placed on the engine sidewalls to cause the transition to turbulent flow in the upstream portion of the inlet. The engine internal top surface will be aligned with the tunnel nozzle top surface (fig. 6) and the boundary layer will be a continuation of the already-turbulent tunnel nozzle boundary layer.

Engine flow.— The inviscid flow properties through the interior of the engine were calculated using an oblique swept shock computer program (ref. 5) for the inlet, a one-dimensional combustion program (ref. 15) for the combustor, and a two-dimensional characteristics program (ref. 20) for the nozzle. All computer programs used equilibrium real gas flow models.

A view of the wave system in the inlet is shown in a plane parallel to the cowl in figure 7. Note that the effective sidewall angle is assumed to be 6° (rather than the geometric 5.6°) to approximate the boundary layer displacement thickness. The calculated inviscid flow properties in the various wave bays of figure 7 are tabulated in Table I. The values of these flow properties do not include end effects caused by the presence of the top surface and the cowl.

Calculated inviscid flow properties through the combustor are tabulated in Table II as a function of distance from the fuel injection line. Since the combustor calculations are one-dimensional (ref. 15), this distribution can be applied to any combustor surface by starting the distribution zero point at the desired location on the swept fuel injection line which is swept parallel to the sidewall leading edge. In calculating these combustor properties, the following parameters were used:

$$\begin{aligned} \text{aerodynamic contraction ratio,} & \quad A_1/A_2 = 8.04 \\ \text{flow spillage parameter,} & \quad A_1/A_c = .929 \\ \text{inlet kinetic energy efficiency, } \eta_{KE, \text{ inlet}} & = .989 \\ \text{fuel equivalence ratio,} & \quad \phi_f = 1.0 \\ \text{combustor chemical efficiency,} & \quad \eta_{\text{comb}} = 1.0 \end{aligned}$$

combustor skin friction coefficient, $C_f = .0026$
combustor exit-to-aerodynamic throat area ratio, $A_3/A_2 = 5.21$

The combustor heat release distribution used in the calculations involves the assumption that all of the fuel was injected from the fuel injection struts at sonic velocities perpendicular to the air flow.

Calculated inviscid flow properties through the engine nozzle are tabulated in Table III for the top surface and for the cowl as a function of distance from the beginning of the nozzle. Note that the nozzle begins along a 48° sweep line with the top surface nozzle zero occurring at engine station 91.16 cm (35.89 in.) and the cowl nozzle zero occurring at engine station 106.9 cm (42.07 in.) In calculating these nozzle properties, the following parameters were used:

nozzle exit-to-engine inlet area ratio (geometric), $A_4/A_c = 1.0$

nozzle kinetic energy efficiency, $\eta_{KE, nozz} = .98$

Boundary layer flow along the engine top surface was turbulent from engine station zero (fig. 2) since the tunnel boundary layer was already turbulent. However, transition on the engine sidewalls was assumed to occur as a result of boundary layer tripping 10.16 cm (4 inches) downstream from the leading edge. On all other surfaces transition was assumed to begin either at a Reynolds number based on boundary layer momentum thickness of 1000, at the first glancing or impinging shock location, or at the fuel injection location.

Heat transfer rates.- Heat transfer rate distributions to the various engine components (except the leading edges) were calculated using the integral boundary layer method of reference 19. Heat transfer rates to the swept leading edges were calculated using a swept-cylinder method from reference 23. For all calculations, the surface temperatures were assumed to be 289 K (520 R).

Heat transfer distributions were calculated for each component along a representative surface path s_x in the direction of gas flow. (See fig. 2 for the coordinate system.) The component and the y or z location of the path are tabulated below:

Sidewall (y = 13.97 cm (5.5 in.))
Top Surface (z = 0)
Cowl (z = 0)
Center strut (y = 10.16 cm (4 in.))
Side strut-side passage (y = 10.16 cm (4 in.))
Side strut-center passage (y = 10.16 cm (4 in.))

The heating rate distributions and recovery temperature distributions for the paths listed above are plotted in figure 8. In figures 8d-8f, the dashed curves for T_r and \dot{q} represent $\phi_f=0$ conditions, i.e., no hydrogen fuel injection.

Stagnation line heating rates, recovery temperatures, and flow properties are tabulated in Table IV for the leading edges of the engine fuel injection struts, sidewalls, and cowl. The heat transfer rates and recovery temperatures calculated here will be used in the next section to derive heat transfer film coefficients.

The heating rates were also integrated over the internal surface areas of the various engine components to find the total heat load to the engine ($T_w = 520$ R). These results are tabulated in Table V.

Temperature Distributions

Heat transfer program.- Computer modeling of the entire scramjet model to determine the temperature distributions would be a difficult, time-consuming task involving three-dimensional, transient, heat transfer techniques. Therefore, the problem was attacked by applying the two-dimensional, transient heat transfer analysis program of reference 16 to various components and sections of the engine.

This heat transfer program employs a finite difference method for the solution of the temperature histories of one-dimensional, two-dimensional, and axisymmetric thermal models. The thermal model is divided into a number of small blocks or elements whose heat transfer mechanisms, dimensions, areas, volumes, and relationships to neighboring elements must be described. These elements may be of as many as 10 different materials with temperature-dependent properties.

Although several options are available for specifying the heat transfer to the thermal model, the technique chosen was to specify a film coefficient and recovery temperature for each element exposed to convective heating. Radiation heating either to or from the elements was neglected. The aerodynamic recovery temperatures and the heating rates to the various engine components were obtained using the integral boundary layer method of reference 19 and have been presented in figure 8. The film coefficients were calculated from

$$h_{fi,a} = \left[\frac{\dot{q}}{T_r - T_w} \right]_a \quad (1)$$

for a wall temperature of 289 K (520 R). No allowance was made for the effect of a variation in wall temperature on the local film coefficient since the effect is small over the present wall temperature range.

Some of the computer thermal models used to analyze the scramjet model included cooling water tubes, backside water channels, and hydrogen fuel manifolds. The film coefficients for surfaces exposed to these fluids were calculated using a method from reference 24 for turbulent flow ($N_{Re,D_H} > 2000$) in tubes where:

$$h_{fi,cl} = 0.023 \left[\frac{C_{p,b} \rho_{fi} V}{(N_{Pr,fi})^{2/3} \left(\frac{\rho_{fi} V D_H}{\mu_{fi}} \right)^{0.2}} \right]_{cl} \quad (2)$$

Fluid properties (except $C_{p,b}$) in equation (2) are evaluated at the film temperature

$$T_{fi} = \frac{T_{b,av} + T_w}{2} \quad (3)$$

where

$$T_{b,av} = \frac{T_{in} + T_{out}}{2} \quad (4)$$

For water flow, equation (2) may be simplified to (ref. 24):

$$h_{fi,cl} = 0.0333 \left[(1 + 0.013 T_{fi}) \frac{(V)^{.8}}{(D_H)^{.2}} \right]_{cl} \quad (5)$$

with

$$h_{fi} \text{ in } \frac{\text{BTU}}{\text{ft}^2 \text{ s R}}$$

$$T_{fi} \text{ in F}$$

$$V \text{ in ft/sec}$$

$$D_H \text{ in inches}$$

Since the film coefficients for the water channels depend on the film temperature, an iteration technique was used to arrive at the correct values of both film coefficient and film temperature. This procedure consisted of repeatedly running the program using the calculated film temperatures from the previous run to calculate a new film coefficient. This process was continued until no further change in the element temperature occurred. Normally 3 or 4 computer runs were required for convergence.

Output from the computer program consisted of time, element temperature, and heat transfer rate to the convective surfaces of the elements. This last factor was used to obtain the bulk temperature rise in each water channel which, in turn, was used in the iteration procedure above.

The element temperatures adjacent to the water channels were used to get a conservative estimate of the cooling water temperature immediately adjacent to the coolant channel wall. This information was used in the iteration technique discussed above and also to determine the minimum channel pressure levels that would be required to prevent boiling.

Thermal models.- In order to better define the temperature distributions in the 3-dimensional scramjet engine, the 2-dimensional heat transfer program (ref. 16) was applied to two types of thermal models. In one case, computer thermal models were made using axially cut sections of the sidewall, top surface, and cowl. However, these models did not account for the thermal effects of adjacent surfaces on each other or for the internal wetted aerodynamic heat

transfer area varying from the engine inlet to the exhaust (as can be seen in fig. 2a), thereby effectively creating "hidden" heat sinks, i.e., remote masses of copper not exposed to convective heating. To investigate the thermal effect of these two factors, computer models of 7 engine station sections (examples of which are shown at the bottom of fig. 2a) were set up.

Computer thermal models were also made of the side and center struts for struts both with and without hydrogen fuel injection manifolds. The strut computer models were derived from section cuts normal to the leading edge. This modeling was sufficient since the thermal gradients in the struts should be essentially 2-dimensional away from the strut ends. As mentioned previously, several portions of the scramjet model were found to require some water cooling, i.e., leading edges, struts, and parts of the sidewalls. Therefore, many of the computer models included convection surfaces representing backside water channels or leading edge cooling tubes.

Some sample computer thermal models of the axial sidewall section, engine station 66.55 cm (26.20 in.) section, and the center hydrogen strut section normal to the leading edge are shown in figure 9. The elements in figure 9a are not to scale; however, the element sizing can be determined from the tables on the figure. The elements in figures 9b and 9c are to scale. Rather large differences in element sizes will be noted in the models. The small elements were used to get accurate surface temperatures near convective surfaces. Justification for the large range of element sizes is the high conductivity of copper and the long times involved. Element shapes other than rectangular are necessary in some cases, especially on the fuel injection struts, but are used at the sacrifice of some accuracy.

The sidewall model shown (fig. 9a) is segmented so that the temperature distribution can be calculated with more precision. The sidewall leading edge segment, inlet segment, and combustor segment are also selectively cooled to linearize the sidewall temperature gradient as will be discussed later. Aerodynamic convective heating to the sidewall thermal models occurs only along surfaces labeled "hot flow" which correspond to the interior of the engine. Convective cooling by water takes place on the elements adjoining the shaded areas. All other exposed surfaces are assumed to be adiabatic.

The station section view model shown (fig. 9b) is completely heat sink. Only the internal surfaces of this model receive convective heating; other exposed surfaces are assumed to be adiabatic. Station 66.55 cm (26.2 in.) is at a location in the engine where both the cowl and top surface convective heating areas are small (fig. 2a) and therefore should provide a dramatic demonstration of the "hidden" heat sink effect mentioned earlier.

The computer model of the center hydrogen fuel injection strut (fig. 9c) includes three water cooling passages and two hydrogen fuel manifolds. The strut design will be discussed later. The center strut is shown cut along its longitudinal center line since the strut is symmetrical about this center line. Note that all exterior surfaces of the fuel injection struts receive aerodynamic heating.

Thermal Strains and Cycle Life

Since the scramjet model was predominately a heat sink model, temperature levels well above room temperature as well as temperature gradients were expected. These factors required that thermal stresses and strains and cycle life be considered in the design of the model.

The first effort at decreasing thermal stresses and strains was to allow the model to expand freely as the temperature increased. This was accomplished by such design features as: (1) oversized boltholes, (2) leaving slots in the cowl for the side struts to expand into, and (3) saw-cutting large unheated masses of copper in the nozzle top surface to allow them to grow independently of other surfaces (fig. 3). These cuts are not exposed to the flow and therefore do not increase engine drag.

Even when the model is unrestrained, thermal stresses and strains can occur as a result of nonlinear temperature gradients. The computer thermal models described previously were used to determine the temperature gradients along the scramjet model surfaces and a method from reference 18 was used as a guide to determine when steps should be taken to linearize these temperature gradients. The expression for the elastic thermal stresses on an unrestrained flat plate of width $2c$ in the x -direction with a temperature gradient in the x -direction is:

$$\sigma_y = -\alpha ET + \frac{1}{2c} \int_{-c}^{+c} \alpha ET \, dx + \frac{3x}{2c} \int_{-c}^{+c} \alpha ET x \, dx \quad (6)$$

This expression applies within the elastic limit and includes a restriction that the calculated stresses are only representative of the true stresses several multiples of $2c$ from the ends of the plate in the y -direction. Therefore, in the present case, the stresses can only be predicted with some sense of accuracy on the fuel injection struts. However, results of the stress calculations on other components are regarded as upper limits.

In the present study, the solution of eq. (6) was by computer. Input consisted of the required material properties (i.e., α and E as functions of temperature) and tabulated values of temperature and distance, x . The integrals above were evaluated numerically. Although the calculated elastic stresses were inapplicable if they were above the proportional limit, it was felt that the associated strain could be used as the true total strain according to the principle of elastic strain invariance (ref. 13). Therefore, the total strain was calculated from

$$\epsilon_{t\ell} = \frac{\sigma_{\text{calc.}}}{E} = \frac{\sigma_y}{E} \quad (7)$$

This total strain and the local temperature was used to find the actual stress, σ_{act} , from a family of stress-strain curves as shown in figure 10a for unannealed copper and in figure 10b for annealed copper. (These approximate stress-strain curves for various temperatures for unannealed and annealed copper were constructed from the room temperature tensile test data discussed previously with the temperature effect added using the elevated temperature data from reference 14.)

Plastic strain was calculated from:

$$\epsilon_{pl} = \epsilon_{tl} - \epsilon_{el} = \epsilon_{tl} - \frac{\sigma_{act}}{E} \quad (8)$$

In addition, total strain range, which is required for cycle life estimates, was calculated as follows (ref. 13):

$$\Delta\epsilon_t = \epsilon_{tl} + \frac{\sigma_{act}}{E} = 2\epsilon_{el} + \epsilon_{pl} \quad (9)$$

Cycle life is inherently difficult to predict. However, a technique that is often used is the universal slopes method (ref. 17) where:

$$\Delta\epsilon_t = \frac{3.5 \sigma_u}{E} N_f^{-0.12} + \left[\ln \frac{1}{1-RA} \right]^{0.6} N_f^{-0.6} \quad (10)$$

This method usually overestimates cycle life at elevated temperatures as shown in figure 11. (Fig. 11 is essentially a copy of fig. 17 from ref. 17 with the addition of the universal slopes prediction for annealed high-conductivity, oxygen-free copper at 811 K (1460 R) which was made using the property data from ref. 14.) The universal slopes prediction in figure 11 must be divided by a factor of approximately 10 to match the data for annealed copper (ref. 25) which was obtained by mechanical cycling at a temperature of 811 K (1460 R). This factor of 10 represents the "lower bound" prediction of the universal slopes method while the result from equation (10) represents the "upper bound" as outlined in reference 26. Although most isothermal, mechanically cycled fatigue data have been found to fall within these prediction limits, data from thermally fatigued specimens have generally been found to have significantly less cycle life than the mechanically fatigued specimens. This is illustrated by the data point shown in figure 11 which was reported in reference 17. Similar results reported in references 13 and 27 indicate that thermally fatigued specimens generally have one-half, or less, of the cycle life of the isothermal, mechanically cycled specimens. Thus, thermally fatigued specimens could have as little as 1/20 to 1/40 of the cycle life predicted by the universal slopes method depending upon how well the mechanical properties of the metal are shown.

Cycle life of hard drawn oxygen-free, high conductivity copper as a function of temperature for various total strain ranges is shown in figure 12. The universal slopes method was used for these estimates simply to demonstrate that cycle life may be lower at about 533 K (960 R) than at higher temperatures for total strain ranges exceeding .003. This is caused by a decrease in the reduction-of-area property of the copper near 533 K (960 R) and the dominance of the second term of equation (10) in the high strain, low cycle life regime. This phenomenon, if true, simply adds to the uncertainty of copper cycle life predictions at elevated temperatures.

RESULTS AND DISCUSSION

The results indicate that the scramjet model will meet the design constraints. Cycle life estimates show that the model will withstand considerably more than 100 cycles (perhaps 1000) of 30 seconds duration in the tunnel flow environment with minimum distortion. This was accomplished with an engine weight of 2509 N (564 lbf), which is below the design limit of 2669 N (600 lbf), while cooling the engine only in critical locations.

Results of the thermal analyses using the computer thermal models of the various components and sections of the scramjet engine model are shown in figures 13, 15, 16, 18, 19, 21 and 22, respectively, after 30 seconds of exposure to the calculated environment. Part "a" of each figure is the surface temperature distribution in the s_x -direction (see coordinate system, fig. 2) except in the case of the struts where the distance is normal to the strut leading edge. Plastic strain distributions, when presented, are the "b" parts of the figures. However, it is emphasized again that these are to be considered only as somewhat of a guide as to the severity of the thermal strains on a component because of the constraints discussed previously on the theoretical approach which was used to obtain the strain.

Component - Related Results

Sidewall.- The engine sidewall temperature distribution is shown in figure 13a. The dashed curve is the uncooled sidewall result from the axial model (fig. 9a), the symbols are the uncooled sidewall results 6.35 cm (2.5 in.) above the cowl obtained from the station models, and the solid curve is the result from the axial model using water cooling in selected areas (fig. 9a). On the uncooled sidewall, the leading edge temperature reaches a maximum of 631 K (1136 R) and a point on the combustor sidewall is also near this temperature. Most of the data from the station view thermal models (away from the sidewall leading edge) are in general agreement with this uncooled axial temperature distribution. The temperature gradients near the leading edge and near the combustor are of concern because of possible excessive thermal strains.

The plastic thermal strain distribution for the uncooled sidewall is shown by the dashed curve in figure 13b. The highest thermal strains occur near the sidewall leading edge and at the beginning of the combustor. The magnitude of these plastic strains as well as the total strain range and overall thermal growth of the model at the high temperatures in these regions were of concern since at least 100 thermal cycles with minimum distortion of the model were required. Life expectancy in terms of cycles (or tests) was difficult to define, as discussed previously, since the behavior of the thermal loadings is not identical to the reverse-cycle mechanical loadings of most laboratory test specimens.

Minimum life of the uncooled sidewall was estimated at the maximum temperature point of 631 K (1135 R) where the calculated total strain range was approximately 0.003. A lower limit on life of 1000 cycles was estimated by dividing

the universal slope prediction by 40 as discussed in the section of this report on thermal strains and cycle life.

While the life of the sidewall appears adequate, the decision was made to selectively cool the scramjet sidewall in an attempt to minimize growth and distortion by decreasing temperatures and by linearizing the temperature distribution to reduce plastic and total strain (note from eq.(6) that an unrestrained plate with a linear temperature gradient has zero thermal stresses). The decision to water-cool the sidewalls took into account the loss in strength of the copper (fig. 4) during the brazing cycle that would be required to install the water channels. An aid to making the decision was the successful experience with brazed copper reported in reference 15 (see fig. 5). In those tests, both the temperature levels and the plastic and total strains were more severe than in the present case.

The location of the water tube in the leading edge and the water channels in the remainder of the sidewall are shown in the sidewall model at the top of figures 13a and 13b and, in more detail, in figure 14. The locations and sizes of these coolant passages are the result of an iterative study to determine the best location for the channels, the proper value of film coefficients, and acceptable temperature rise levels of the cooling water. Flow control is via miniature valves on the downstream side of each channel. Each channel is part of a parallel flow circuit system from an inlet manifold to an outlet manifold (fig. 14).

The attempt to linearize the sidewall temperature gradient with a minimum of cooling channels was relatively successful as can be noted from the temperature distribution (fig. 13a) and also from the plastic strain distribution shown in figure 13b. The plastic strains with the cooled sidewall are generally reduced to more reasonable levels although they are increased in some areas relative to the values for the uncooled case. However, in all cases, the total strain and overall thermal growth is decreased by the water cooling. It is also interesting to note that a minimum life estimate for the cooled sidewall (based solely on the temperature distribution for an unrestrained plate) is approximately 25,000 cycles.

The design parameters for the sidewall cooling channels as well as for the cooling passages of all other components are listed in Table VI. Some of the parameters are channel dimensions, cooling water inlet and outlet temperatures, minimum pressure required to prevent boiling, and water flow rates.

The same type of approach to the problem of temperature level and gradients that was used on the sidewall is generally applicable to the other components. However, in some cases, factors such as accessibility for installation of cooling passages and expendability of the component were also considered.

Top surface.— The temperature distribution from the axial-cut thermal model of the uncooled top surface is shown as the dashed line in figure 15. The leading edge temperature is not high because the leading edge is shielded by the tunnel nozzle exit as shown in figure 6. This thermal model does indicate a rather severe gradient and a high temperature level at the combustor entrance.

However, the top surface temperature data obtained from the thermal models of the station views (symbols) show much less severe conditions in this region. In fact, top surface temperatures in the combustor area are of the same magnitude as those on the cooled sidewall in that area. This is due to the lowering of the top surface temperatures by the hidden heat sinks mentioned earlier which are created by a decrease in the convective heating area along this portion of the top surface (sidewalls converge to create a minimum flow width in this region as may be seen in figs. 2 and 7). The temperatures in this region will probably be reduced further by the sidewall water cooling.

These factors led to the omission of top surface water cooling except for the leading edge. While not required with the model in the position shown in figure 6, water cooling of the unswept top surface leading edge might be required if the model were to be lowered farther into the stream. Plastic strains were not calculated for the top surface since the actual temperature gradient on the top surface would be affected by the sidewall cooling. However, the level of temperature and the temperature gradients are less than in the case of the uncooled sidewall.

Cowl.- The temperature distribution from the axial-section thermal model of the uncooled cowl is shown as the dashed line in figure 16. The temperature level of the entire cowl is high, with the leading edge temperature nearing the melting point of the copper. Results from the station view thermal models show that the temperatures near the combustor inlet are significantly lower than predicted from the axial-section model. This is again because of decreased convective heating areas in this region. The effect of sidewall water-cooling will be to further reduce the cowl temperatures.

Clearly, the cowl leading edge requires water-cooling. In addition, without cooling downstream of the cowl leading edge, a mismatch in temperature exists between the forward cowl and the sidewall. However, it was decided that the cowl was of sufficiently simple construction to risk leaving it uncooled except for the leading edge. Plastic strains were not calculated in detail for the cowl section. However, the leading edge cooling and the hidden heat sink effect (fig. 16) imply that a gradient similar to that on the uncooled sidewall will exist on the forward cowl. On this basis, a minimum life of about 1000 cycles would be anticipated. The forward part of the cowl is thus expected to be the region of least cycle life.

Struts.- Two sets of struts have been designed for use in the scramjet engine model. In one set, no hydrogen fuel manifolds are included and the purpose of these struts is to measure surface static pressures. The other set of struts was designed for the perpendicular injection of hydrogen fuel.

Without hydrogen fuel injection: Diagrams of these struts illustrating the cooling water routing are shown in figures 17a and 17b. Temperature distributions along the chord perpendicular to the leading edge are shown for the cooled and uncooled struts in figures 18 and 19. Cooling is required since the temperatures of both uncooled struts lie between 830-1111 K (1500-2000 R). Without cooling, the copper experiences severe strength losses (fig. 10a) caused by the high temperatures.

Water cooling brings the temperature levels of the struts within more reasonable limits of 306-444 K (550-800 R). Although the copper is annealed because of the brazing cycle required for fabrication of the coolant channels, the strength is greater (fig. 10b) than for the uncooled, unannealed copper. In addition, the lower temperatures cause less thermal growth and the total and plastic thermal strains will be less.

With hydrogen fuel injection: The design of these struts (figs. 20a and 20b) coupled the requirement of surviving the thermal environment with the requirement of injecting the fuel properly. Details of the strut design are reported in the Appendix and only the salient features relating to the thermal analysis are presented here.

Basically, the factors resulting in the designs shown in figures 20a and 20b were: (1) cross-sectional area of the fuel manifolds had to be sufficiently large that the hydrogen Mach number was lower than 0.2 to prevent an excessive pressure drop in the manifolds; (2) manifold span had to be kept to a minimum (depending on strut wall thickness) so that pressure stresses were within acceptable limits, $<10.3 \text{ MN/m}^2$ (1500 psi); (3) since hydrogen temperature is measured only at the manifold entrance, water-cooling had to be placed close to the hydrogen manifolds so that the hydrogen bulk temperature would not increase significantly over the strut length (this enhances the accuracy of the calculation of the mass flow rate from each orifice).

The temperature distributions for these fuel injection struts are shown in figures 21a and 22 and the plastic thermal strains on the center strut are shown in figure 21b. The temperatures of the struts with no water cooling are less than those on the other set of struts (figs. 18 and 19) because the flowing hydrogen in the manifolds is cooling the struts. This means, however, that the hydrogen is increasing in temperature as it flows down the strut, thereby making individual orifice mass flow rate determination more difficult. Even with this hydrogen cooling, surface temperatures and plastic thermal strains are excessive.

Water cooling decreases the heat flow to the hydrogen fuel and also decreases the strut surface temperatures below 472 K (850 R). Gradients still exist near the leading edges of the struts and between the hydrogen channels on the side strut. However, it appears from the geometry of the strut that further water cooling is impractical. The plastic strain levels in the cooled struts are significantly lower than in the uncooled struts (fig. 21a). In addition, the total strain levels are greatly reduced and minimum life should exceed 2,500 cycles.

Test Time Effects

The temperature levels and distributions and the thermal strains on the components just presented were all based upon the 30 second test time constraint mentioned earlier. For future engine models, it is of interest to know if the complexity of water-cooling could be avoided if lesser test times were required, for instance, 15 seconds. The answer to this appears to be that one would still need to cool the struts as well as the leading edges of the top surface, sidewall, and cowl. However, the sidewall cooling might be eliminated. A comparison of the uncooled sidewall temperature distributions after 15 and 30 seconds

of exposure to the calculated tunnel environment is shown in figure 23. Both the temperature levels and the temperature gradients are decreased for the shorter test time and the highest temperature is no longer bordering on the annealing temperature of the copper.

CONCLUDING REMARKS

An aerodynamic model of a hydrogen-burning, airframe-integrated scramjet engine has been designed and fabricated for testing in an electric arc-heated wind tunnel at a stream energy level duplicating Mach 7 flight at an altitude of 35.39 km (116,094 ft). The scramjet inlet Mach number is 6 to simulate the pre-compression which would occur on an aircraft undersurface. Local flow properties as well as heating rates throughout the scramjet were calculated and are presented.

The results indicate that the scramjet model will meet the design constraints of at least 100 cycles with minimum distortion, minimum cooling, and a model weight of less than 2669 N (600 psi). Total and plastic strains resulting from thermal gradients were reduced in the engine by a selective cooling arrangement and a minimum life of 1000 cycles on one engine component is expected. Other components should have longer lives. The total engine weight was 2509 N (564 lbf). In addition, the water-cooled fuel injection struts were designed to withstand the necessary fuel injection pressures while successfully maintaining the hydrogen fuel Mach number in the strut manifolds below 0.2. The design and analysis techniques presented herein for the partially cooled, heat-sink, copper structure provide a basis for future design of similar test components and engines for high temperature, high Mach number research.

APPENDIX

Design of the Hydrogen Fuel Injection Struts

Proper design of the hydrogen fuel injection struts from a propulsion viewpoint required a determination of the following:

- (1) The distribution of the captured airflow in the fuel injection region,
- (2) The number of fuel injection orifices and their spacing,
- (3) The required strut fuel manifold pressure,
- (4) The injector orifice sizes and the fuel manifold cross-sectional area.

The design from the propulsion viewpoint involved trade-offs with structural considerations and with heat transfer considerations to avoid excessive stresses and temperatures.

Distribution of Captured Airflow in Fuel Injection Region

According to reference 4, the ratio of the captured streamtube flow area to the projected engine capture area, A_1/A_c , is 0.93 at an inlet Mach number of 6. Therefore, the captured air mass flow rate for the scramjet engine in the Scramjet Test Facility is

$$\dot{m}_a = \rho_1 V_1 A_c \left(\frac{A_1}{A_c} \right) = 1.011 \frac{\text{kg}}{\text{s}} \left(2.228 \frac{\text{lbm}}{\text{s}} \right) \quad (\text{A1})$$

and the total mass flow rate of hydrogen fuel is

$$\dot{m}_{\text{H}_2} = 0.0293 \phi_f \dot{m}_a = 0.0296 \frac{\text{kg}}{\text{s}} \left(0.06528 \frac{\text{lbm}}{\text{s}} \right) \quad (\text{A2})$$

for stoichiometric ($\phi_f=1$) combustion.

The next step in designing the fuel injection struts is to determine the distribution of the air flow in the passages between the struts and between the struts and the sidewall so that the proper distribution of hydrogen fuel can be injected. In reference 4, results of experiment at an inlet Mach number of 6 indicated that 1/3 of the captured air flow passes through the side passages between the side struts and the engine sidewall while the remaining 2/3 passes through the center passages between the side struts and the center struts. Since the side passages are to be fed by one row of perpendicular sonic injection orifices while the center passages are to be fed by 2 rows of these orifices, it is logical to assume that 1/6 of the air flow is fed by each row of orifices.

To detail the airflow distribution further, it is necessary to know the local distribution of the air flow from the top surface to the cowl in the side and center passages. Such a distribution is affected by the boundary layers on the struts, sidewall, cowl, and engine top surface and by the cowl shock. Local air mass flow rate per unit area, ρV , was measured at the throats between the struts at an inlet Mach number of 6 and reported in reference 4. These data, corrected to the inlet ρV of the Scramjet Test Facility are shown in figure 24 for the center and the side passages. The hydrogen fuel must be injected according to this ρV distribution if a uniform fuel equivalence ratio is to be achieved.

Number of Fuel Injection Orifices and Their Spacing

The next step in the design process involves determining the number of orifices and their spacing so that the volume of flow area fed by each orifice may be determined. At the inlet throat the width between the engine sidewalls is approximately

$$WD_2 \approx 0.3 HT_c = 6.20 \text{ cm (2.4 in)} \quad (A3)$$

where HT is the inlet projected height. Likewise, the height of the engine at the inlet throat location is approximately

$$HT_2 \approx 0.9 HT_c = 18.29 \text{ cm (7.2 in.)} \quad (A4)$$

In addition, the projected flow blockage by the struts on the minimum width between the scramjet sidewalls, i.e., WD_2 , is

$$B \approx 60\%$$

With 1 row of orifices feeding each $1/6$ of the air flow, the effective gap width fed by each row of orifices is

$$g = \frac{(1 - B) WD_2}{6} = 0.406 \text{ cm (0.16 in.)} \quad (A5)$$

Experiments have shown that for proper fuel penetration and lateral mixing, the ratio of the orifice spacing (normal to the flow direction) to the effective gap width should be about

$$\ell/g = 3.125. \quad (A6)$$

Therefore, $\ell = 1.27 \text{ cm (0.5 in.)}$. From this, the number of orifices per row is:

$$n = \frac{HT_2}{\ell} \approx 14 \quad (A7)$$

Using this number of orifices for each injection row together with the required

external strut geometry, the orifices were placed to inject hydrogen as shown by the arrows in figure 25. The flow volumes to be fed by each of the orifices are assumed equal and symmetrical around each orifice except near the top surface and the cowl. As seen on the figure, the shortened geometry of the center strut (the strut is cantilevered from the scramjet top surface) dictated that only 13 orifices could be placed on each side. In addition, some area in the cowl region was neglected in determining the flow area to be fed by hydrogen in order to decrease the possibility of choking in this region. With the volume of air to be fed by each orifice specified, the mass flow rate of hydrogen required (for the desired fuel equivalence ratio) from each orifice can be determined.

Strut Fuel Manifold Pressure

The dynamic pressure ratio of the fuel at the injection orifices to that of the undisturbed air free stream should be at least 0.6 to insure that the hydrogen orifice flow is sonic. Therefore,

$$\frac{q_f}{q_a} = 0.6 \text{ was used for } \phi_f = 0.5$$

in the proposed tests in the Scramjet Test Facility (ϕ_f ranging from .5 to 2). The ratio of fuel dynamic pressure at $M = 1$ and $\gamma = 1.4$ to fuel total pressure is (ref. 28):

$$\frac{q_f}{p_{t,f}} = 0.3698 \quad (A8)$$

Therefore, the fuel manifold pressure is:

$$p_{t,f} = \frac{p_{t,f}}{q_f} \frac{q_f}{q_a} q_a = 2.704 \frac{q_f}{q_a} q_a \quad (A9)$$

From equation (A2),

$$\phi_f = \frac{1}{.0293} \frac{\dot{m}_f}{\dot{m}_a} = \frac{1}{.0293} \frac{V_a}{\sqrt{\gamma R T_f}} \frac{q_f}{q_a} \frac{A_{or} C_d}{g \ell} \quad (A10)$$

Therefore, for a given set of airflow conditions just upstream of the fuel injection orifices, fuel total temperature, gap width, orifice spacing, and for a given discharge coefficient, q_f/q_a is directly proportional to ϕ_f . Consequently, for the tests in the Scramjet Test Facility, the following conditions apply when $q_f/q_a = 0.6$ is specified at $\phi_f = 0.5$.

ϕ_f	$\frac{q_f}{q_a}$	$\frac{P_{t,f}}{q_f}$	q_a		$P_{t,f}$	
			$\frac{kN}{m^2}$	$\frac{lbf}{in^2}$	$\frac{kN}{m^2}$	$\frac{lbf}{in^2}$
.5	.6	2.70	240.	34.9	390.	56.5
1.0	1.2	⋮	⋮	⋮	779.	113.0
1.5	1.8	⋮	⋮	⋮	1169.	169.5
2.0	2.4	⋮	⋮	⋮	1558.	226.0

Orifice Size and Fuel Manifold Cross-Sectional Area

The equation for the mass flow rate of hydrogen from an orifice is

$$\dot{m}_{or} = \rho^* v^* A^* = \rho^* v^* A_{or} C_d \quad (A11)$$

or upon rearranging,

$$d_{or} = \sqrt{\frac{4}{\pi} \frac{\dot{m}_{or}}{\rho^* v^* C_d}} = 19.11 (T_{t,f})^{0.25} \left(\frac{\dot{m}_{or}}{P_{t,f}} \right)^{0.5} \quad (A12)$$

where the * quantities are at Mach 1 and C_d has been assumed to be 0.8. Therefore, the only unknown in this equation is $T_{t,f}$ which depends on the static hydrogen temperature at each orifice and upon the velocity of the hydrogen at that point in the fuel manifold. Assuming constant specific heats,

$$T_{t,f} = T_f + \frac{V_f^2}{2C_p} = T_f \left(1 + \frac{\gamma-1}{2} M_f^2 \right) \quad (A13)$$

The equation above contains V_f which is doubly important because it contributes not only to the fuel total temperature but also to any pressure drops in the fuel manifold. It is desirable to minimize the pressure drop in the manifold so that each orifice will see the same injection pressure. This was accomplished by keeping the cross-sectional area of the manifold as large as was practical so that the manifold fuel Mach number never exceeded 0.2 and therefore $p_f/p_{t,f}$ was $> .9725$ (ref. 28). In addition, it can be seen from reference 28 for $M = 0.2$ that

$$A/A^* = 2.9635 = \frac{A_{\text{manifold}}}{A_{\text{orifices, total}}}$$

To obtain an estimate of the required manifold area, the incoming hydrogen temperature was assumed to be 289 K (520 R) and the manifold Mach number to be 0.2. Therefore, from equation (A13),

$$T_{t,f} = 291 \text{ K (524.2 R)}$$

Now, $1/14 \times 1/6$ of the total engine hydrogen flow rate is assumed to pass from each orifice in the side struts and $1/13 \times 1/6$ through each orifice in the center strut. Therefore, from equation (A12), the average orifice size in the side strut is $d_{or} = .1074 \text{ cm (.0423 in.)}$ and in the center strut $d_{or} = .1115 \text{ cm (.0439 in.)}$. This means that the total orifice area in each strut is $.254 \text{ cm}^2$ (0.03935 in^2). Therefore, the manifold area in each strut for $M = 0.2$ should be $.752 \text{ cm}^2$ (0.1166 in^2). This is actually somewhat conservative since geometric rather than effective orifice diameters were used to determine the area and therefore the actual hydrogen Mach number in the manifolds will be < 0.2 .

Using this manifold area as a guide, the hydrogen manifolds were designed consistent with cooling water channel locations and with the constraint on hydrogen channel span to keep mechanical stresses below 10.34 MN/m^2 (1500 psi). These constraints, particularly the latter one, in combination with the requirement that the manifold Mach number be less than 0.2 dictated that the hydrogen channels be split as shown in figures 20a and 20b, so that no one channel received all of the hydrogen flow for that particular strut. This design limited the span of metal exposed to the manifold pressure and decreased the total mass flow of hydrogen through the individual channels.

With the hydrogen manifolds designed and with the orifices located as shown in figure 20, calculations were performed to determine local hydrogen manifold flow conditions at each orifice. These calculations were performed by dividing the hydrogen channel into segments between the orifices. Thus, loss of hydrogen at the orifices was included as well as heat input to the hydrogen from the external flow. The heat input to the hydrogen was estimated using the computer thermal models discussed in the main text. These calculations provided the hydrogen total temperature at each orifice.

Therefore, with the mass flow rate for each orifice known and with the fuel pressure and temperature as well as the orifice discharge coefficient known, the required orifice diameter was calculated using equation (A12). These diameters were rounded off to the nearest drill size and are listed in the tables on figures 20a and 20b.

REFERENCES

1. Henry, John R.; and Anderson, Griffin Y.: Design Considerations for the Airframe-Integrated Scramjet. NASA TM X-2895, Dec. 1973.
2. Wieting, Allan R.; and Guy, Robert W.: Preliminary Thermal-Structural Design and Analysis of an Airframe-Integrated Hydrogen-Cooled Scramjet. AIAA Paper No. 75-137, Jan. 1975.
3. Wieting, Allan R.; and Guy, Robert W.: Thermal-Structural Design/Analysis of an Airframe-Integrated Hydrogen-Cooled Scramjet. Journal of Aircraft, Vol. 13, No. 3, March 1976, pp. 192-197.
4. Trexler, Carl A.: Performance of an Inlet for an Integrated Scramjet Concept. Journal of Aircraft, Vol. 11, No. 9, Sept. 1974, pp. 589-591.
5. Trexler, Carl A.; and Souders, Sue W.: Design and Performance at a Local Mach Number of 6 of an Inlet for an Integrated Scramjet Concept. NASA TN D-7944, Aug. 1975.
6. Trexler, C. A.: Inlet Performance of the Integrated Langley Scramjet Module (Mach 2.3 to 7.6). Presented at the AIAA/SAE 11th Propulsion Conference. Anaheim, CA. Sept. 29-Oct. 1, 1975.
7. Beach, H. Lee, Jr.: Supersonic Mixing and Combustion of a Hydrogen Jet in a Coaxial High-Temperature Test Gas. AIAA Paper No. 72-1179, Nov.-Dec. 1972.
8. Rogers, R. Clayton; and Eggers, James M.: Supersonic Combustion of Hydrogen Injected Perpendicular to a Ducted Vitiated Airstream. Paper presented at the AIAA/SAE Ninth Propulsion Conference (Las Vegas, Nevada), Nov. 1973.
9. Anderson, Griffin Y.; and Gooderum, Paul B.: Exploratory Tests of Two Strut Fuel Injectors for Supersonic Combustion. NASA TN D-7581, Feb. 1974.
10. Anderson, Griffin Y.: An Examination of Injector/Combustor Design Effects on Scramjet Performance. Paper presented at the 2nd International Symposium on Air Breathing Engines (Sheffield, England), March 25-29, 1974.
11. Sebacher, Daniel I.; and Lee, Louise P.: Cross Flow in Two-Dimensional Asymmetric Nozzles. NASA TN D-7999, Aug. 1975.
12. Boatright, William B.; Sabol, Alexander P.; Sebacher, Daniel I.; Pinckney, Shimer Z.; and Guy, Robert W.: Langley Facility for Tests at Mach 7 of Subscale, Hydrogen-Burning, Airframe-Integratable, Scramjet Models. AIAA Paper No. 76-11, Jan. 1976.
13. Manson, S. S.: Thermal Stress and Low-Cycle Fatigue. McGraw-Hill Book Co., New York, 1966.

14. OFHC Brand Copper - A Survey of Properties and Applications. AMAX, Inc. 1974. (Lib. of Congress Catalog Card Number: 74-80767).
15. Pinckney, S. Z.; Guy, R. W.; Beach, H. L.; and Rogers, R. C.: Subscale, Hydrogen-Burning, Airframe-Integrated Scramjet Engine: Experimental and Theoretical Evaluation of a Water-Cooled Strut Leading Edge. NASA TM X-72682, May, 1975.
16. Garrett, Bernard L.; and Pitts, Joan I.: A General Transient Heat-Transfer Computer Program for Thermally Thick Walls. NASA TM X-2058. Aug. 1970.
17. Miller, Roy W.: Cyclic Fatigue Analysis of Rocket Thrust Chambers. Volume I-OFHC Copper Chamber Low Cycle Fatigue. NASA CR-134641, June, 1974.
18. Timoshenko, S.; and Goodier, J. N.: Theory of Elasticity. McGraw-Hill Book Company, Inc., New York, 1951.
19. Pinckney, S. Z.: Turbulent Heat Transfer Prediction Method for Application to Scramjet Engines. NASA TN D-7810, Nov. 1974.
20. Dash, S.; Del Guidice, P.; and Kalber, P.: Analysis of Three-Dimensional Supersonic Nozzles. NASA CR-132350, Vol. I and NASA CR-132351, Vol. II, 1972.
21. Lordi, J. A.; Mates, R. E.; and Moselle, J. R.: Computer Program for the Numerical Solution of Nonequilibrium Expansions of Reacting Gas Mixtures. CAL Report No. AD-1689-A-6, Oct. 1965.
22. Anders, John B.; Sebacher, Daniel I.; and Boatright, William B.: Fluid Flow Analysis of a Hot-Core Hypersonic-Wind-Tunnel Nozzle Concept. NASA TN D-6768, May, 1972.
23. Cohen, Nathaniel B.: Boundary-Layer Similar Solutions and Correlation Equations for Laminar Heat-Transfer Distributions in Equilibrium Air at Velocities Up to 41,000 Feet Per Second. NASA TR R-118, 1961.
24. McAdams, William H.: Heat Transmission. McGraw-Hill Book Company, Inc. New York, 1954.
25. Conway, J. B.; Stentz, R. H.; and Berling, J. T.: High Temperature, Low-Cycle Fatigue of Copper-Base Alloys in Argon; Part I - Preliminary Results for 12 Alloys at 1000^oF (538^oC). NASA CR-121259, Jan. 1973.
26. Manson, S. S.; and Halford, G.: A Method of Estimating High-Temperature Low Cycle Fatigue Behavior of Materials. Thermal and High-Strain Fatigue, The Metals and Metallurgy Trust, c. 1967, pp. 154-170.
27. Conway, J. B.; Stentz, R. H.; and Berling, J. T.: High Temperature, Low Cycle Fatigue of Copper-Base Alloys in Argon; Part III - Zirconium-Copper. Thermal-Mechanical Strain Cycling, Hold-Time and Notch Fatigue Results. NASA CR-121261, Dec. 1973.

28. Ames Research Staff: Equations, Tables, and Charts for Compressible Flow.
NACA Report 1135, 1953.

TABLE I. - INLET FLOW PROPERTIES

a. Parameters in International System of Units (SI)

Bay	M	p	T	ρ	V	h	H	γ	q	δ	β
		(kN/m ²)	(K)	(kg/m ³)	(m/s)	(MJ/kg)	(MJ/kg)		(kN/m ²)	(deg)	(deg)
											Between Bays
1	6.000	1.39	312	0.0155	2123	0.3138	2.566	1.399	34.9	0.	
2	5.183	3.18	402	.0276	2079	.4068		1.396	59.7	1.644	1, 2=14.56
3	4.563	6.51	496	.0457	2029	.5091		1.388	94.0	2.783	2, 3=10.22
4	4.075	12.11	593	.0711	1973	.6206		1.377	138.5	4.833	3, 4=18.96
5	4.239	9.91	558	.0618	1994	.5788		1.381	122.9	4.265	3, 5=17.10
6	3.808	17.60	657	.0933	1935	.6927		1.369	174.7	5.808	4, 6=13.19
7	4.764	5.18	462	.0391	2047	.4719		1.391	81.8	2.744	2, 7=20.89
8	5.413	2.45	373	.0229	2095	.3742		1.397	50.2	1.670	7, 8=19.15
9	4.068	9.94	595	.0577	1982	.6020		1.377	113.2	5.435	8, 9=18.42
10	3.313	27.06	800	.1185	1846	.8624		1.353	202.1	11.512	9, 10=21.69
11	4.563	6.51	496	.0457	2029	.5091		1.388	94.0	2.783	2, 11=10.22
12	4.075	12.11	593	.0711	1973	.6206		1.377	138.5	4.833	11, 12=18.96
13	3.808	17.60	657	.0933	1935	.6927		1.369	174.7	5.808	12, 13=13.19
14	3.569	24.78	722	.1196	1896	.7694		1.362	214.9	7.393	13, 14=24.02

TABLE I. - CONCLUDED.

b. Parameters in the English system of Units

Bay	M	p (lb/ft^2)	T (R)	ρ ($\frac{\text{slugs}}{\text{ft}^3}$)	V (ft/sec)	h ($\frac{\text{Btu}}{\text{lbm}}$)	H ($\frac{\text{Btu}}{\text{lbm}}$)	γ	q ($\frac{\text{lb}}{\text{ft}^2}$)	δ (deg)	β (deg)
							1104				Between Bays
1	6.000	29.0	561	0.301×10^{-4}	6964	135		1.399	730	0.	
2	5.183	66.5	723	0.536	6820	175		1.396	1247	1.644	1, 2=14.56
3	4.563	135.9	893	0.886	6656	219		1.388	1963	2.783	2, 3=10.22
4	4.075	253.0	1068	1.380	6474	267		1.377	2892	4.833	3, 4=18.96
5	4.239	206.9	1004	1.200	6541	249		1.381	2567	4.265	3, 5=17.10
6	3.808	367.6	1183	1.810	6350	298		1.369	3649	5.808	4, 6=13.19
7	4.764	108.2	832	0.758	6715	203		1.391	1709	2.744	2, 7=20.89
8	5.413	51.2	672	0.444	6872	161		1.397	1048	1.670	7, 8=19.15
9	4.068	207.6	1071	1.119	6502	259		1.377	2365	5.435	8, 9=18.42
10	3.313	565.2	1440	2.300	6058	371		1.353	4220	11.512	9, 10=21.69
11	4.563	135.9	893	0.886	6656	219		1.388	1963	2.783	2, 11=10.22
12	4.075	253.0	1068	1.380	6474	267		1.377	2892	4.833	11, 12=18.96
13	3.808	367.6	1183	1.810	6350	298		1.369	3649	5.808	12, 13=13.19
14	3.569	517.6	1299	2.321	6219	331		1.362	4488	7.393	13, 14=24.02

TABLE II. - COMBUSTOR FLOW PROPERTIES, $\phi_f = 1$

a. Parameters in International System of Units (SI)

$x_{\text{comb.}}$	M	p	T	ρ	V	h	H	γ	q	ϕ_f	$\eta_{\text{comb.}}$	A/A ₂
(cm)		(kN/m ²)	(K)	(kg/m ³)	(m/s)	(MJ/kg)	(MJ/kg)		(kN/m ²)			
0.0	3.324	32.13	809	0.1385	1863	0.830	2.566	1.353	240.4	0.	0.0	1.000
0.51	3.324	32.13	809	.1385	1863	.830	2.566	1.353	240.4	0.	.208	1.000
1.50	2.042	58.41	1343	.1134	1683	1.929	3.345	1.318	160.6	1.0	.208	1.391
2.49	2.033	49.65	1458	.0899	1728	2.101	3.594	1.309	134.2		.285	1.710
3.51	2.010	43.95	1581	.0742	1763	2.287	3.842	1.300	115.4		.363	2.029
4.50	1.984	39.88	1708	.0631	1792	2.483	4.089	1.291	101.4		.440	2.348
5.51	1.916	39.79	1865	.0583	1791	2.731	4.335	1.282	93.6		.517	2.542
6.50	1.823	42.28	2039	.0574	1765	3.012	4.570	1.274	89.4		.595	2.622
7.49	1.752	44.15	2193	.0563	1746	3.268	4.791	1.267	85.8		.672	2.702
8.51	1.703	45.25	2321	.0551	1733	3.494	4.995	1.261	82.8		.750	2.782
9.50	1.720	43.57	2326	.0530	1750	3.503	5.035	1.261	81.2		.763	2.861
10.49	1.736	42.04	2331	.0511	1766	3.510	5.070	1.260	79.8		.776	2.941
11.51	1.751	40.55	2336	.0493	1782	3.519	5.107	1.259	78.3		.789	3.021
12.50	1.766	39.21	2341	.0477	1796	3.529	5.142	1.259	76.9		.803	3.101
13.51	1.780	37.97	2346	.0461	1811	3.538	5.177	1.258	75.6		.816	3.181
14.50	1.793	36.77	2352	.0446	1824	3.547	5.211	1.258	74.3		.829	3.261
15.49	1.805	35.67	2357	.0433	1837	3.556	5.244	1.257	73.1		.842	3.341
16.51	1.819	34.57	2359	.0420	1850	3.561	5.274	1.256	71.8		.853	3.421
17.50	1.834	33.47	2358	.0407	1864	3.559	5.295	1.256	70.7		.861	3.501
18.49	1.849	32.46	2356	.0395	1877	3.556	5.316	1.256	69.6		.869	3.581
19.51	1.862	31.46	2355	.0384	1889	3.554	5.337	1.256	68.5		.877	3.661
20.50	1.876	30.55	2354	.0374	1901	3.552	5.358	1.255	67.6		.885	3.740
21.49	1.889	29.69	2353	.0363	1913	3.549	5.379	1.255	66.5		.893	3.820
22.50	1.901	28.87	2353	.0354	1924	3.549	5.400	1.255	65.5		.900	3.900
23.50	1.913	28.11	2352	.0345	1935	3.547	5.418	1.254	64.5		.908	3.980
24.51	1.925	27.39	2352	.0337	1945	3.547	5.439	1.254	63.6		.916	4.060
25.50	1.936	26.67	2352	.0328	1955	3.547	5.458	1.254	62.7		.924	4.140
26.49	1.947	26.05	2351	.0321	1965	3.547	5.476	1.254	61.9		.932	4.220
27.51	1.958	25.38	2351	.0313	1974	3.545	5.495	1.253	61.0		.940	4.300
28.50	1.969	24.75	2348	.0306	1984	3.540	5.509	1.253	60.1		.945	4.380
29.49	1.981	24.13	2345	.0299	1993	3.535	5.521	1.253	59.4		.950	4.460
30.51	1.992	23.56	2342	.0292	2003	3.529	5.535	1.253	58.6		.956	4.540
31.50	2.003	23.03	2339	.0286	2011	3.524	5.546	1.253	57.8		.961	4.619
32.51	2.013	22.50	2337	.0280	2020	3.519	5.560	1.252	57.1		.966	4.699
33.50	2.024	21.98	2334	.0274	2028	3.515	5.572	1.252	56.4		.972	4.779
34.49	2.034	21.50	2332	.0269	2036	3.510	5.583	1.252	55.7		.977	4.859
35.51	2.043	21.02	2329	.0263	2046	3.505	5.595	1.252	54.9		.982	4.939
36.50	2.053	20.59	2327	.0258	2052	3.501	5.607	1.252	54.2		.987	5.019
37.49	2.062	20.16	2324	.0253	2060	3.496	5.618	1.252	53.7		.993	5.099
38.51	2.072	19.73	2322	.0248	2067	3.491	5.627	1.252	53.0	V	.998	5.179

TABLE II. - CONCLUDED

b. Parameters in the English System of Units.

$x_{\text{comb.}}$ (in.)	M	p (lbf/ft ²)	T (R)	ρ (slugs/ft ³)	V (ft/sec)	h ($\frac{\text{Btu}}{\text{lbm}}$)	H ($\frac{\text{Btu}}{\text{lbm}}$)	γ	q (lbf/ft ²)	ϕ_f	$\eta_{\text{comb.}}$	A/A ₂
0.	3.324	671	1456	2.688 x 10 ⁻⁴	6112	357	1104	1.353	5021	0.	0	1.000
0.20	3.324	671	1456	2.688	6112	357	1104	1.353	5021	0.	0.208	1.000
0.59	2.042	1220	2418	2.201	5521	830	1439	1.318	3354	1.0	0.208	1.391
0.98	2.033	1037	2624	1.744	5670	904	1546	1.309	2803		0.285	1.710
1.38	2.010	918	2845	1.440	5785	984	1653	1.300	2410		0.363	2.029
1.77	1.984	833	3075	1.225	5880	1068	1759	1.291	2118		0.440	2.348
2.17	1.916	831	3357	1.132	5875	1175	1865	1.282	1954		0.517	2.542
2.56	1.823	883	3670	1.113	5792	1296	1966	1.274	1867		0.595	2.622
2.95	1.752	922	3947	1.093	5728	1406	2061	1.267	1793		0.672	2.702
3.35	1.703	945	4177	1.069	5687	1503	2149	1.261	1729		0.750	2.782
3.74	1.720	910	4186	1.029	5742	1507	2166	1.261	1696		0.763	2.861
4.13	1.736	878	4195	0.992	5795	1510	2181	1.260	1666		0.776	2.941
4.53	1.751	847	4204	0.957	5846	1514	2197	1.259	1635		0.789	3.021
4.92	1.766	819	4213	0.925	5894	1518	2212	1.259	1607		0.803	3.101
5.32	1.780	793	4223	0.895	5941	1522	2227	1.258	1579		0.816	3.181
5.71	1.793	768	4233	0.866	5985	1526	2242	1.258	1551		0.829	3.261
6.10	1.805	745	4242	0.840	6028	1530	2256	1.257	1526		0.842	3.341
6.50	1.819	722	4247	0.814	6071	1532	2269	1.256	1500		0.853	3.421
6.89	1.834	699	4244	0.790	6115	1531	2278	1.256	1477		0.861	3.501
7.28	1.849	678	4241	0.767	6157	1530	2287	1.256	1454		0.869	3.581
7.68	1.862	657	4239	0.745	6198	1529	2296	1.256	1431		0.877	3.661
8.07	1.876	638	4238	0.725	6238	1528	2305	1.255	1411		0.885	3.740
8.46	1.889	620	4236	0.705	6275	1527	2314	1.255	1388		0.893	3.820
8.86	1.901	603	4235	0.687	6312	1527	2323	1.255	1369		0.900	3.900
9.25	1.913	587	4234	0.669	6347	1526	2331	1.254	1348		0.908	3.980
9.65	1.925	572	4233	0.653	6381	1526	2340	1.254	1329		0.916	4.060
10.04	1.936	557	4233	0.637	6414	1526	2348	1.254	1310		0.924	4.140
10.43	1.947	544	4232	0.622	6446	1526	2356	1.254	1292		0.932	4.220
10.83	1.958	530	4232	0.607	6477	1525	2364	1.253	1273		0.940	4.300
11.22	1.969	517	4226	0.593	6509	1523	2370	1.253	1256		0.945	4.380
11.61	1.981	504	4221	0.580	6540	1521	2375	1.253	1240		0.950	4.460
12.01	1.992	492	4216	0.567	6570	1518	2381	1.253	1224		0.956	4.540
12.40	2.003	481	4211	0.555	6599	1516	2386	1.253	1208		0.961	4.619
12.80	2.013	470	4206	0.543	6627	1514	2392	1.252	1192		0.966	4.699
13.19	2.024	459	4202	0.532	6655	1512	2397	1.252	1178		0.972	4.779
13.58	2.034	449	4197	0.521	6681	1510	2402	1.252	1163		0.977	4.859
13.98	2.043	439	4193	0.510	6708	1508	2407	1.252	1147		0.982	4.939
14.37	2.053	430	4188	0.500	6733	1506	2412	1.252	1133		0.987	5.019
14.76	2.062	421	4184	0.491	6758	1504	2417	1.252	1121		0.993	5.099
15.16	2.072	412	4180	0.481	6782	1502	2421	1.252	1106		0.998	5.179

TABLE III. - NOZZLE FLOW PROPERTIES

a. Parameters in International System of Units (SI)

$x_{noz.}$ (cm)	Surface	M	p (kN/m ²)	T (K)	ρ (kg/m ³)	V (m/s)	h (MJ/kg)	H (MJ/kg)	γ	q (kN/m ²)	ϕ_f	$\eta_{comb.}$				
0 → 16.59	Cowl ↓	2.072	19.74	2322	0.02481	2067	3.491	5.627 ↓	1.252	52.96	1.0 ↓	1.0 ↓				
17.65		2.090	19.09	2308	.02414	2080	3.466		1.252	52.19						
19.20		2.105	18.57	2297	.02360	2090	3.445		1.254	51.57						
20.75		2.121	18.07	2285	.02307	2100	3.422		1.254	50.90						
22.33		2.136	17.57	2273	.02256	2110	3.401		1.255	50.23						
23.95		2.152	17.08	2261	.02205	2120	3.380		1.255	49.60						
25.58		2.167	16.60	2248	.02154	2131	3.359		1.256	48.89						
27.25		2.183	16.12	2235	.02105	2141	3.336		1.258	48.26						
28.93		2.199	15.65	2222	.02056	2152	3.315		1.258	47.59						
31.55		2.224	14.96	2201	.01983	2167	3.280		1.258	46.59						
34.21		2.249	14.30	2179	.01914	2183	3.247		1.261	45.58						
36.96		2.275	13.65	2156	.01846	2198	3.212		1.263	44.62						
39.78		2.302	13.01	2132	.01781	2214	3.178		1.265	43.62						
41.71		2.321	12.60	2114	.01738	2224	3.157		1.267	43.00						
44.68		2.349	12.00	2087	.01677	2240	3.119		1.270	42.04						
0 → 6.10		Top ↓	2.072	19.74	2322	0.02481	2067		3.491	5.627 ↓			1.252	52.96	1.0 ↓	1.0 ↓
6.71			2.085	19.28	2313	.02432	2076		3.473				1.250	52.43		
8.92	2.100		18.76	2301	.02378	2086	3.452	1.251	51.76							
11.13	2.115		18.24	2289	.02324	2097	3.431	1.252	51.09							
13.36	2.131		17.73	2277	.02271	2107	3.408	1.252	50.42							
15.62	2.146		17.22	2264	.02219	2118	3.387	1.255	49.75							
17.91	2.162		16.72	2252	.02167	2128	3.363	1.255	49.08							
20.22	2.179		16.23	2238	.02115	2139	3.340	1.256	48.36							
22.56	2.196		15.74	2224	.02065	2149	3.319	1.256	47.69							
24.92	2.213		15.26	2211	.02014	2160	3.296	1.257	46.97							
27.31	2.230		14.79	2196	.01965	2171	3.270	1.259	46.30							
30.35	2.253		14.21	2176	.01904	2185	3.243	1.261	45.44							
35.31	2.290		13.30	2143	.01810	2206	3.194	1.264	44.05							
40.39	2.329		12.42	2107	.01719	2229	3.145	1.268	42.71							
45.59	2.372		11.56	2066	.01632	2251	3.094	1.272	41.37							
50.95	2.417		10.73	2018	.01552	2274	3.045	1.279	40.12							
56.46	2.464		9.94	1975	.01467	2296	2.992	1.283	38.69							
59.97	2.491	9.46	1956	.01411	2310	2.959	1.283	37.63								

TABLE III. - CONCLUDED.

b. Parameters in English System of Units

$x_{noz.}$ (in.)	Surface	M	p (lbf/ft ²)	T (R)	ρ (slugs/ft ³)	V (ft/sec)	h (Btu/lbm)	H (Btu/lbm)	γ	q (lbf/ft ²)	ϕ_f	$\eta_{comb.}$	
0 → 6.53	Cowl ↓	2.072	412.3	4180	4.814×10^{-5}	6782	1502	2421	1.252	1106	1.0	1.0	
6.95		2.090	398.7	4155	4.683	6823	1491		1.252	1090			
7.56		2.105	387.9	4134	4.580	6857	1482		1.254	1077			
8.17		2.121	377.3	4113	4.477	6891	1472		1.254	1063			
8.79		2.136	366.9	4091	4.378	6924	1463		1.255	1049			
9.43		2.152	356.7	4069	4.279	6958	1454		1.255	1036			
10.07		2.167	346.6	4047	4.180	6991	1445		1.256	1021			
10.73		2.183	336.6	4023	4.084	7025	1435		1.258	1008			
11.39		2.199	326.9	3999	3.990	7059	1426		1.258	994			
12.42		2.224	312.5	3962	3.848	7110	1411		1.258	973			
13.47		2.249	298.6	3922	3.714	7161	1397		1.261	952			
14.55		2.275	285.0	3881	3.582	7212	1382		1.263	932			
15.66		2.302	271.8	3837	3.455	7263	1367		1.265	911			
16.42		2.321	263.2	3806	3.373	7296	1358		1.267	898			
17.59		2.349	250.6	3757	3.254	7348	1342		1.270	878			
0 → 2.40		Top ↓	2.072	412.3	4180	4.814×10^{-5}	6782	1502	2421	1.252	1106	1.0	1.0
2.64			2.085	402.7	4163	4.719	6811	1494		1.250	1095		
3.51	2.100		391.8	4142	4.614	6845	1485		1.251	1081			
4.38	2.115		381.0	4121	4.510	6879	1476		1.252	1067			
5.26	2.131		370.3	4099	4.407	6913	1466		1.252	1053			
6.15	2.146		359.7	4076	4.305	6948	1457		1.255	1039			
7.05	2.162		349.3	4053	4.204	6982	1447		1.255	1025			
7.96	2.179		339.0	4029	4.104	7017	1437		1.256	1010			
8.88	2.196		328.8	4004	4.006	7052	1428		1.256	996			
9.81	2.213		318.8	3979	3.908	7087	1418		1.257	981			
10.75	2.230		308.9	3952	3.813	7123	1407		1.259	967			
11.95	2.253		296.7	3917	3.695	7168	1395		1.261	949			
13.90	2.290		277.7	3857	3.512	7239	1374		1.264	920			
15.90	2.329		259.3	3792	3.336	7312	1353		1.268	892			
17.95	2.372		241.4	3718	3.167	7385	1331		1.272	864			
20.06	2.417		224.2	3632	3.011	7459	1310		1.279	838			
22.23	2.464		207.5	3555	2.847	7534	1287		1.283	808			
23.61	2.491	197.5	3521	2.737	7580	1273		1.283	786				

TABLE IV. - STAGNATION LINE PROPERTIES AND HEAT TRANSFER RATES

a. Parameters in International System of Units (SI)

Component	M	p	T	ρ	V	h	H	γ	q	T_w	h_w	T_r	h_r	\dot{q}
		(kN/m ²)	(K)	(kg/m ³)	(m/s)	(MJ/kg)	(MJ/kg)		(kN/m ²)	(K)	(MJ/kg)	(K)	(MJ/kg)	(kW/m ²)
Sidewall	2.301	29.90	1241	0.0840	1577	1.321	2.566	1.320	104.5	289	0.2901	2056	2.380	4394
Side strut	2.319	47.64	1231	.1349	1584	1.311	2.566	1.321	169.2	289	.2901	2054	2.378	5517
Center strut	2.293	73.97	1240	.2080	1572	1.331	2.566	1.320	256.8	289	.2901	2042	2.362	6781
Cowl	2.321	63.87	1230	.1809	1585	1.310	2.566	1.321	227.2	289	.2901	2054	2.376	6364

TABLE IV. - CONCLUDED.

b. Parameters in English System of Units.

Component	M	p	T	ρ	V	h	H	γ	q	T_w	h_w	T_r	h_r	\dot{q}
		$\left(\frac{\text{lbf}}{\text{ft}^2}\right)$	(R)	$\left(\frac{\text{slugs}}{\text{ft}^3}\right)$	$\left(\frac{\text{ft}}{\text{sec}}\right)$	$\left(\frac{\text{Btu}}{\text{lbm}}\right)$	$\left(\frac{\text{Btu}}{\text{lbm}}\right)$		$\left(\frac{\text{lbf}}{\text{ft}^2}\right)$	(R)	$\left(\frac{\text{Btu}}{\text{lbm}}\right)$	(R)	$\left(\frac{\text{Btu}}{\text{lbm}}\right)$	$\left(\frac{\text{Btu}}{\text{ft}^2 \text{sec}}\right)$
Sidewall	2.301	624.5	2233	1.630×10^{-4}	5175	568.6	1104	1.320	2183	520	124.8	3700	1024	387.2
Side strut	2.319	995.0	2216	2.617	5197	564.2	1104	1.321	3534	520	124.8	3698	1023	486.1
Center strut	2.293	1545.0	2232	4.035	5156	572.5	1104	1.320	5363	520	124.8	3675	1016	597.5
Cowl	2.321	1334.0	2214	3.511	5199	563.6	1104	1.321	4745	520	124.8	3697	1022	560.8

TABLE V. - SUMMARY OF INTERNAL HEAT LOADS
 TO THE SCRAMJET MODEL COMPONENTS
 ($T_w = 289$ K (520 R), $\phi_f = 1.0$)

Component	Heat Load*	
	kW	BTU/s
Inlet		
Top surface	3.6	3.4
Sidewalls (2)	32.7	31.0
Cowl	3.4	3.2
Center Strut	8.4	8.0
Side Struts (2)	22.9	21.7
Combustor		
Top Surface	24.3	23.0
Sidewalls (2)	95.5	90.6
Cowl	30.6	29.0
Center Strut	16.8	15.9
Side Struts (2)	32.3	30.6
Nozzle		
Top Surface	34.7	32.9
Sidewalls (2)	78.1	74.1
Cowl	37.1	35.2

* Heat loads include blunt leading edge values.

TABLE VI. - SCRAMJET COOLING CIRCUIT INFORMATION

a. - Parameters in International System of Units

Component	Location	Cooling Circuit	w	dp	Acs	D _H	V	m	N _{Re,D_H}	T _{in}	T _{out}	T _{b,av.}	T _{w,av.}	T _{w,max}	T _{fi}	h _{fi}	p _{min}
			(cm)	(cm)	(cm ²)	(cm)	(m/s)	(kg/s)		(K)	(K)	(K)	(K)	(K)	(K)	(kW/m ² K)	(kN/m ²)
Sidewall ↓ ↓	Leading edge	1	0.1651	dia.	0.0214	0.1651	12.770	0.0272	32455	288.9	341.1	314.9	352.8	380.0	333.9	66.53	129.3
		2	.9525	0.2540	.2419	.4013	.914	.0220	4142	288.9	309.3	299.1	370.9	384.1	355.1	6.58	149.1
	Inlet ↓ Combustor ↓	3	.9525	.2540	.2419	.4013	.914	.0220	4356	288.9	313.7	301.3	386.6	400.7	343.9	6.58	250.5
		4	.6350	.5080	.3226	.5639	1.524	.0489	9037	288.9	303.9	296.4	371.4	385.3	333.9	9.17	154.7
		5	.6350	.5080	.3226	.5639	3.048	.0978	17697	288.9	302.2	295.6	371.8	385.6	333.7	16.02	156.1
		6	.6350	.5080	.3226	.5639	7.315	.2347	40393	288.9	298.1	293.5	361.8	379.6	327.7	31.11	127.3
		7	.6350	.5080	.3226	.5639	4.572	.1467	25756	288.9	299.7	294.3	372.1	389.9	333.2	22.51	178.6
		8	.9525	.5080	.4839	.6629	2.286	.1100	15140	288.9	299.8	294.3	387.2	402.7	340.8	13.34	267.5
		9	.9525	.5080	.4839	.6629	1.524	.0733	10317	288.9	301.6	295.2	399.8	418.1	347.6	10.15	416.0
Top surface Cowl	Leading edge	10	.1651	dia.	.0214	.1651	12.770	.0272	19427	288.9	292.8	290.8	300.3	314.7	295.6	45.72	8.0
	Leading edge	11	.1651	dia.	.0214	.1651	12.770	.0272	42692	288.9	376.5	332.7	411.1	462.2	371.9	87.72	1231.0
Center fuel injection strut	Trailing edge	12	.2642	.6045	.1600	.3683	13.530	.2147	50942	288.9	301.6	295.2	342.4	360.2	318.8	51.05	62.4
	Middle	13	.3048	.3175	.0968	.3099	19.480	.1875	75078	301.6	305.8	303.7	320.5	325.5	312.1	66.64	13.8
	Leading edge	14	.1651	dia.	.0214	.1651	12.770	.0272	32524	301.6	328.7	315.5	346.8	376.9	331.0	64.55	115.1
Side fuel injection strut	Middle	15	.8255	.2540	.2097	.3886	9.632	.2006	36608	288.9	298.0	293.4	331.9	347.9	312.7	36.65	38.1
	Trailing edge	16	.3810	.2413	.0923	.2972	18.890	.1734	75046	298.0	316.2	307.1	348.8	368.0	327.9	76.52	83.8
	Leading edge	17	.1651	dia.	.0214	.1651	12.770	.0272	33021	298.0	334.4	316.2	352.5	386.0	334.3	66.43	158.2
Center strut	Middle	18	.8255	.2540	.2097	.3886	3.901	.0813	14660	288.9	297.1	293.0	327.9	339.7	310.4	17.28	26.6
	Trailing edge	19	.2540	.1524	.0387	.1905	14.050	.0541	30774	297.1	302.3	299.7	312.0	319.3	305.9	53.00	10.2
	Leading edge	20	.1651	dia.	.0214	.1651	12.770	.0272	31464	297.1	328.1	312.6	353.8	383.9	333.2	61.39	148.0
Side strut	Middle	21	.9525	.2540	.2419	.4013	3.383	.0813	15404	288.9	309.7	299.3	358.0	376.5	328.7	18.22	113.6
	Trailing edge	22	.2540	.1524	.0387	.1905	14.050	.0541	47541	309.7	340.1	324.7	361.3	380.8	343.1	74.69	133.0
	Leading edge	23	.1651	dia.	.0214	.1651	12.770	.0272	40111	309.7	348.6	329.1	367.9	400.6	348.6	70.68	249.0

TABLE VI. - CONCLUDED

b. - Parameters in English System Of Units

Component	Location	Cooling Circuit	w	dp	Ac_s	D _H	V	m	N _{Re,DH}	T _{in}	T _{out}	T _{b,av.}	T _{w,av.}	T _{w,max}	T _{fi}	h _{fi}	p _{min}
			(in.)	(in.)	(in. ²)	(in.)	(ft/sec)	(lbm/sec)	(R)	(R)	(R)	(R)	(R)	(R)	(R)	($\frac{\text{Btu}}{\text{ft}^2 \cdot \text{sec} \cdot \text{R}}$)	(psia)
Sidewall ↓ ↓	Leading edge Inlet	1	0.065	dia.	0.0033	0.065	41.9	0.0600	32455	520.0	613.9	566.9	635.0	684.0	601.0	3.257	18.75
		2	.375	.100	.0375	.158	3.0	.0485	4142	↓	556.7	538.3	667.7	691.4	603.1	.322	21.62
	Combustor ↓ ↓	3	.375	.100	.0375	.158	3.0	.0485	4356	↓	564.6	542.3	695.8	721.3	619.0	.322	36.33
		4	.250	.200	.0500	.222	5.0	.1078	9037	↓	547.0	533.5	668.6	693.5	601.1	.449	22.44
		5	.250	.200	.0500	.222	10.0	.2156	17697	↓	543.9	532.0	669.2	694.0	600.6	.784	22.64
		6	.250	.200	.0500	.222	24.0	.5174	40393	↓	536.5	528.3	651.3	683.3	589.8	1.523	18.47
		7	.250	.200	.0500	.222	15.0	.3234	25756	↓	539.5	529.8	669.7	701.8	599.7	1.102	25.91
		8	.375	.200	.0750	.261	7.5	.2426	15140	↓	539.7	529.8	697.0	724.9	613.4	.653	38.80
		9	.375	.200	.0750	.261	5.0	.1617	10317	↓	542.9	531.4	719.7	752.5	625.6	.497	60.33
Top surface Cowl	Leading edge	10	.065	dia.	.0033	.065	41.9	.0600	19427	520.0	527.0	523.5	540.5	566.5	532.0	2.238	1.16
	Leading edge	11	.065	dia.	.0033	.065	41.9	.0600	42692	520.0	677.7	598.9	740.0	831.9	669.4	4.294	178.50
Center fuel injection strut	Trailing edge	12	.104	.238	.0248	.145	44.4	.4734	50942	520.0	542.8	531.4	616.4	648.4	573.9	2.499	9.05
	Middle	13	.120	.125	.0150	.122	63.9	.4134	75078	542.8	550.5	546.6	577.0	585.9	561.8	3.262	2.00
	Leading edge	14	.065	dia.	.0033	.065	41.9	.0600	32524	542.8	591.6	567.2	624.3	678.4	595.8	3.160	16.69
Side fuel injection strut	Middle	15	.325	.100	.0325	.153	31.6	.4423	36608	520.0	536.4	528.2	597.5	626.2	562.8	1.794	5.52
	Trailing edge	16	.150	.095	.0143	.117	62.0	.3823	75046	536.4	569.1	552.8	627.8	662.4	590.3	3.746	12.16
	Leading edge	17	.065	dia.	.0033	.065	41.9	.0600	33021	536.4	602.0	569.2	634.5	694.8	601.8	3.252	22.95
Center strut	Middle	18	.325	.100	.0325	.153	12.8	.1793	14660	520.0	534.7	527.4	590.2	611.4	558.8	.846	3.86
	Trailing edge	19	.100	.060	.0060	.075	46.1	.1193	30774	534.7	544.2	539.5	561.6	574.8	550.6	2.594	1.48
	Leading edge	20	.065	dia.	.0033	.065	41.9	.0600	31464	534.7	590.6	562.7	636.9	691.0	599.8	3.005	21.47
Side strut	Middle	21	.375	.100	.0375	.158	11.1	.1793	15404	520.0	557.4	538.7	644.4	677.7	591.6	.892	16.47
	Trailing edge	22	.100	.060	.0060	.075	46.1	.1193	47541	557.4	612.1	584.8	650.3	685.4	617.6	3.656	19.29
	Leading edge	23	.065	dia.	.0033	.065	41.9	.0600	40111	557.4	627.4	592.4	662.3	721.0	627.4	3.460	36.12

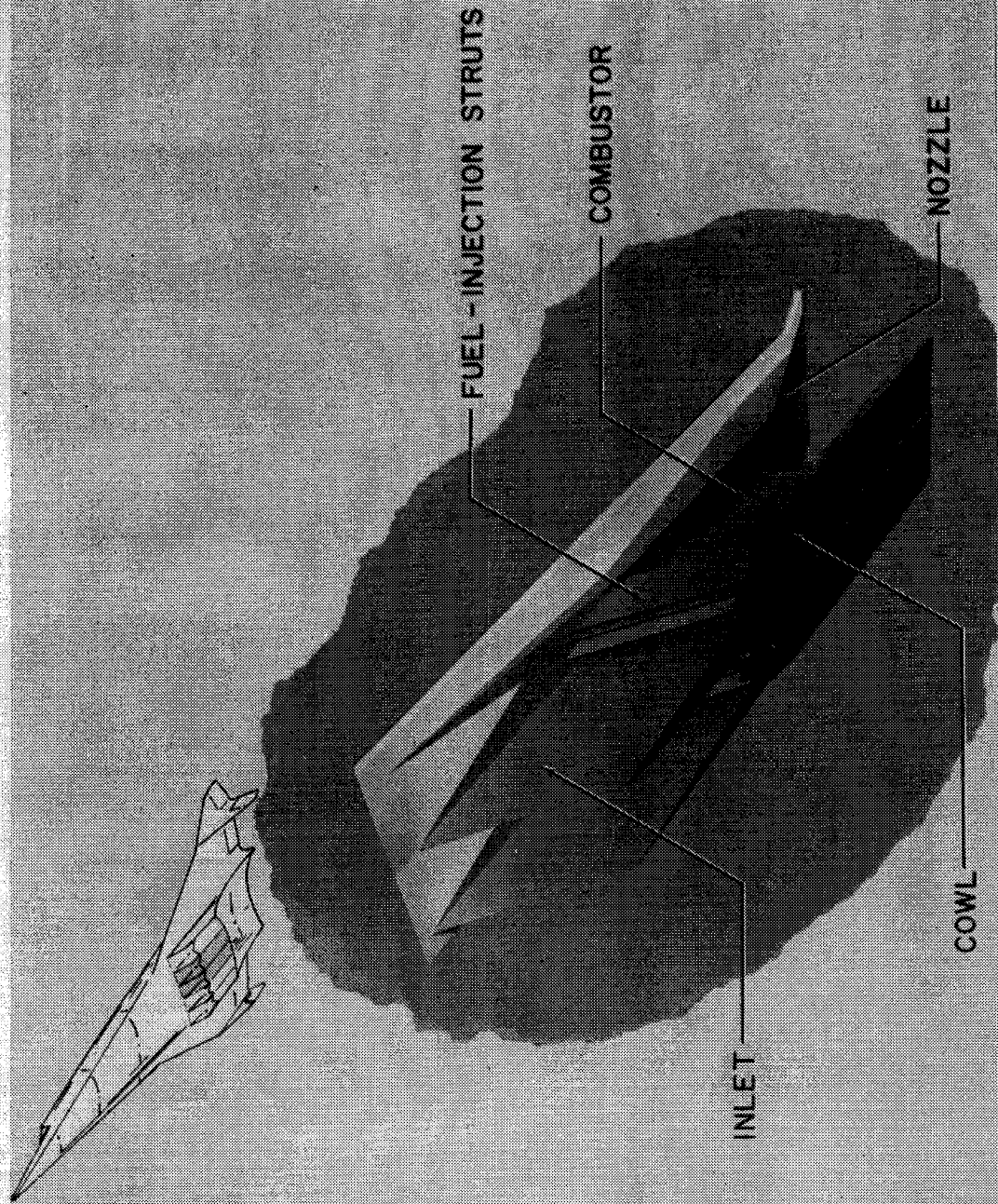
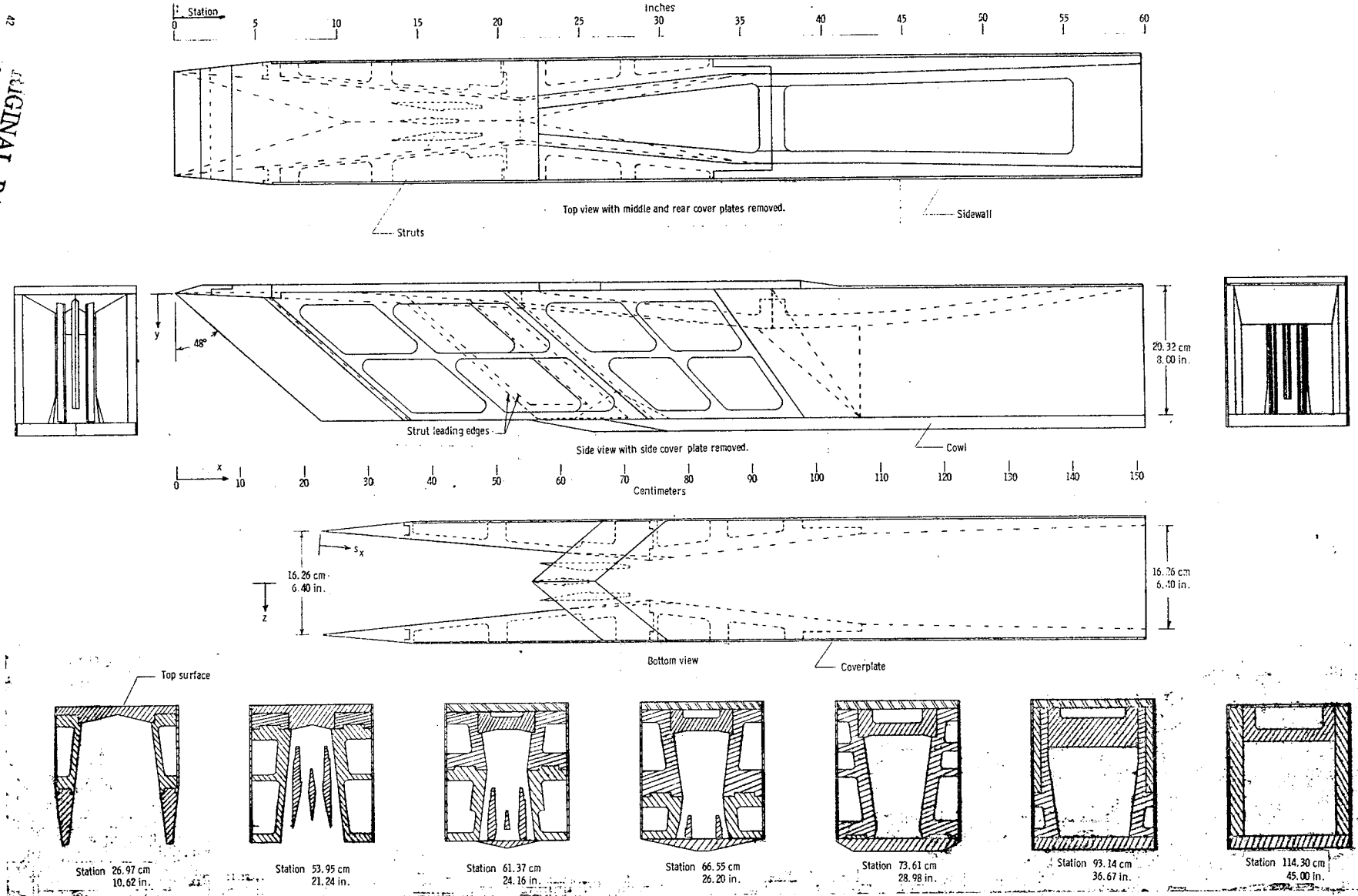


Figure 1.- An airframe-integrated scramjet concept.
(Details of two modules shown.)

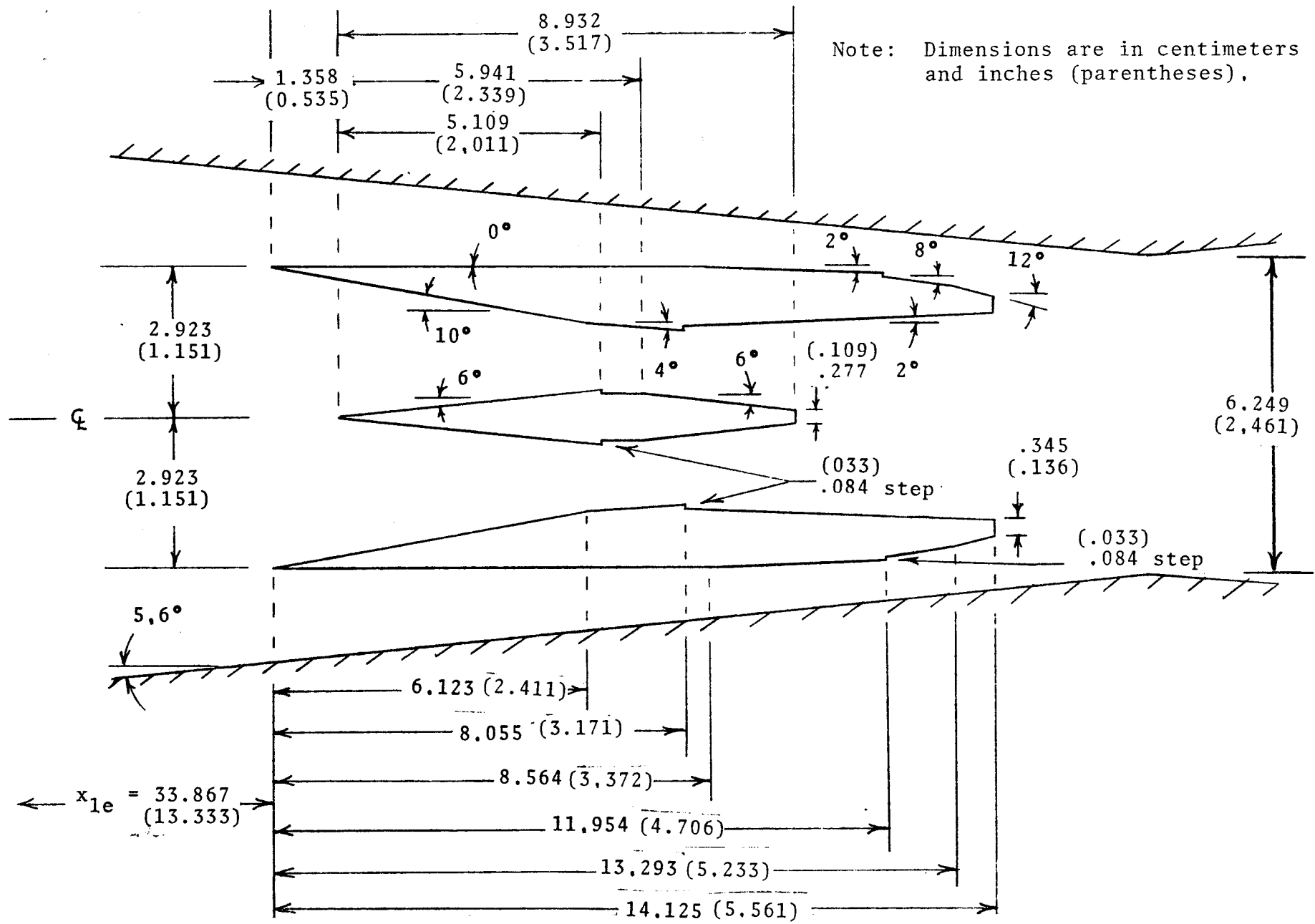
ORIGINAL PAGE IS
OF POOR QUALITY

ORIGINAL PAGE IS
OF POOR QUALITY



a. - Engine views.

Figure 2. - Hydrogen-burning scramjet engine model.



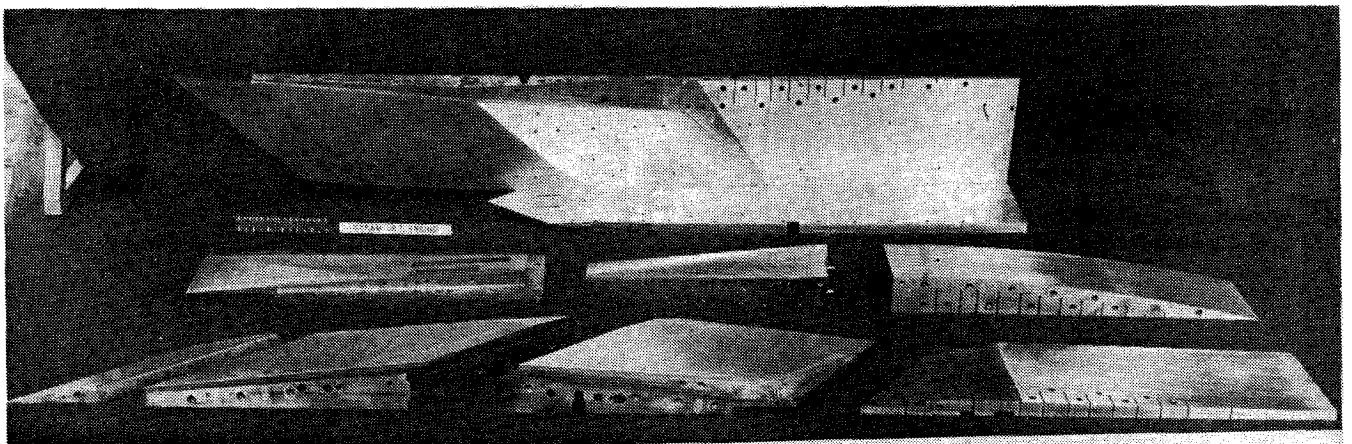
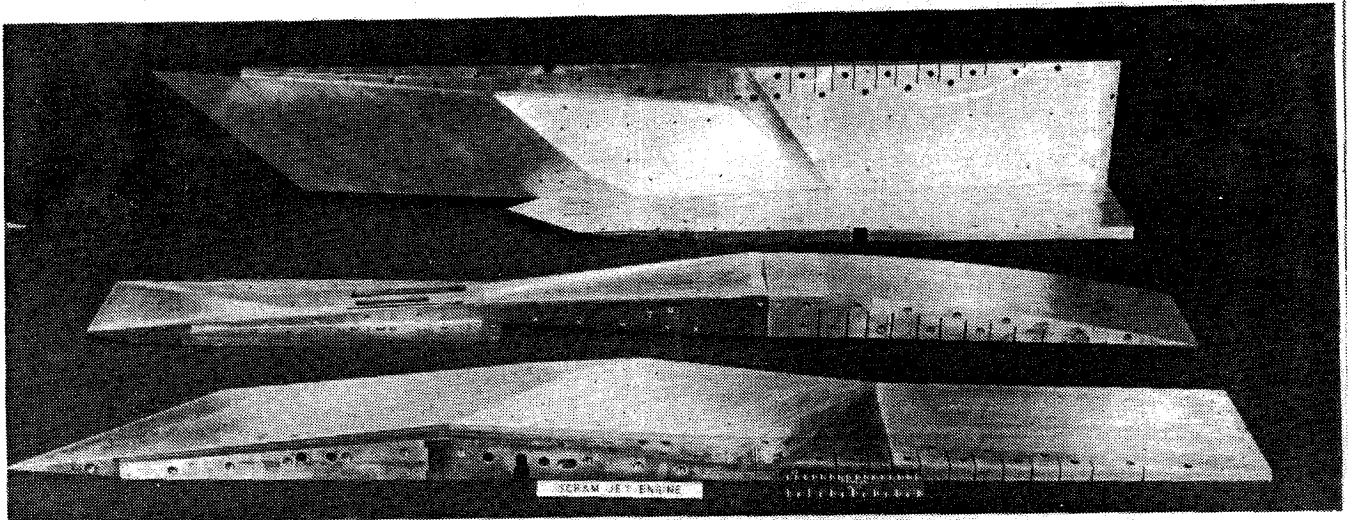
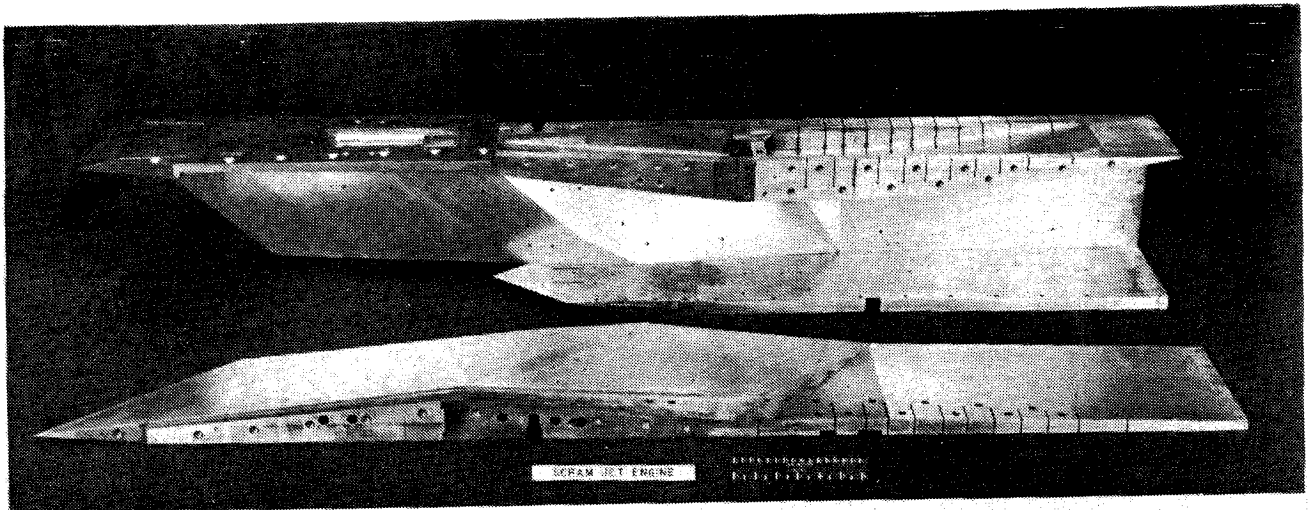
b.- Section views of fuel injection struts in plane parallel to the cowl plane.

Figure 2. - Concluded.



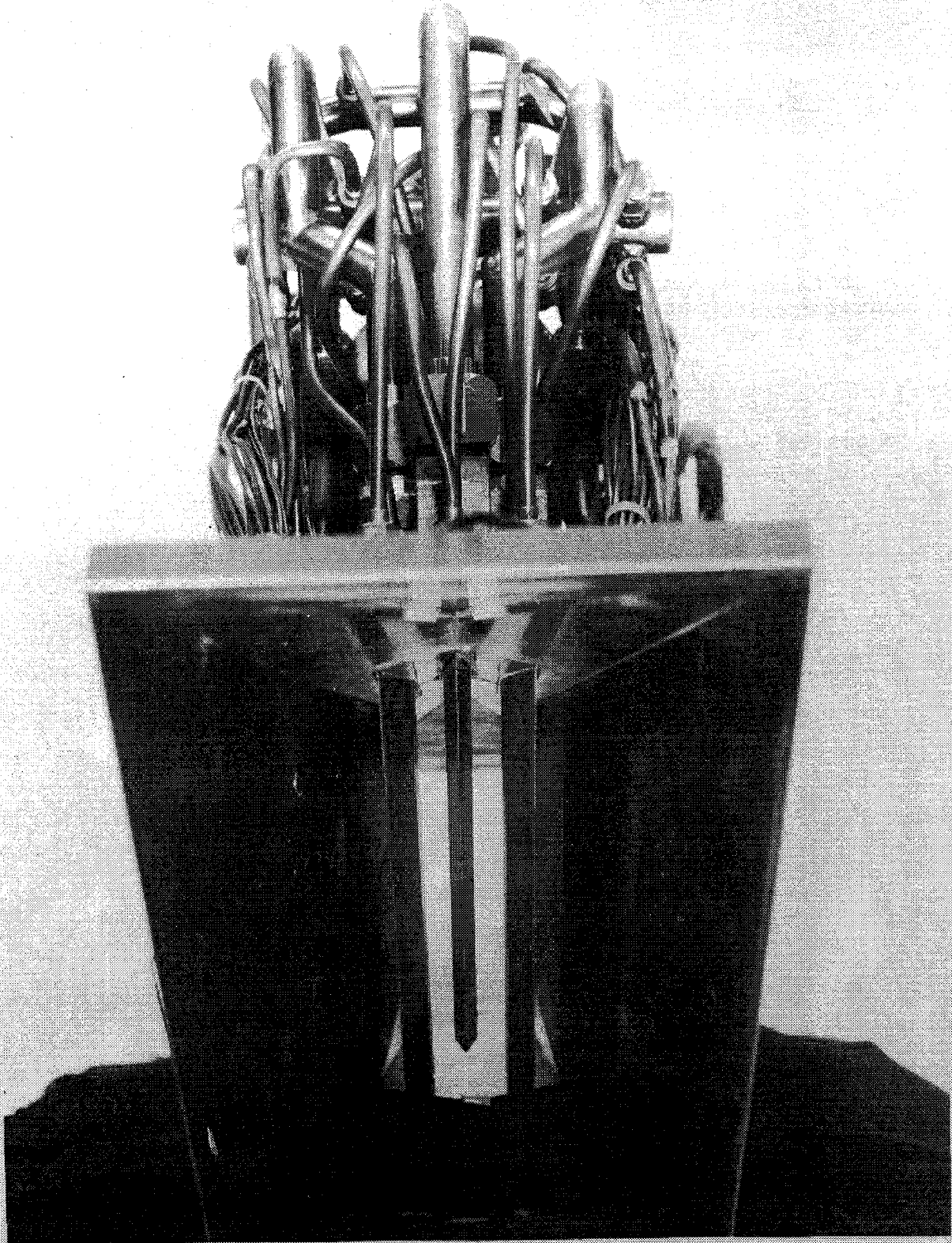
a. - View showing the assembled model.

Figure 3. - Photographs of the scramjet engine model.



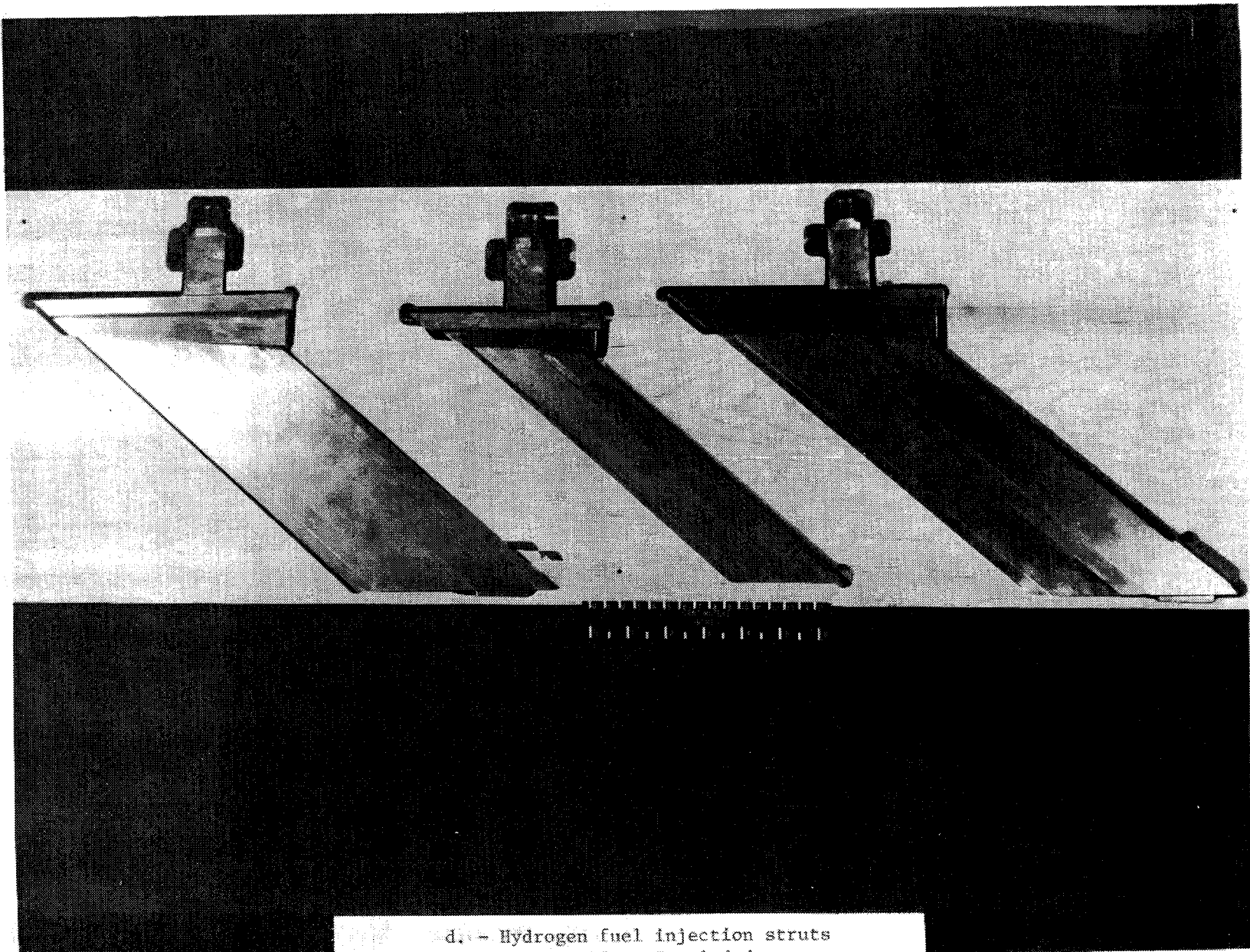
b.- Views showing the model components,
Figure 3.- Continued.

FINAL PAGE IS
FOR QUALITY

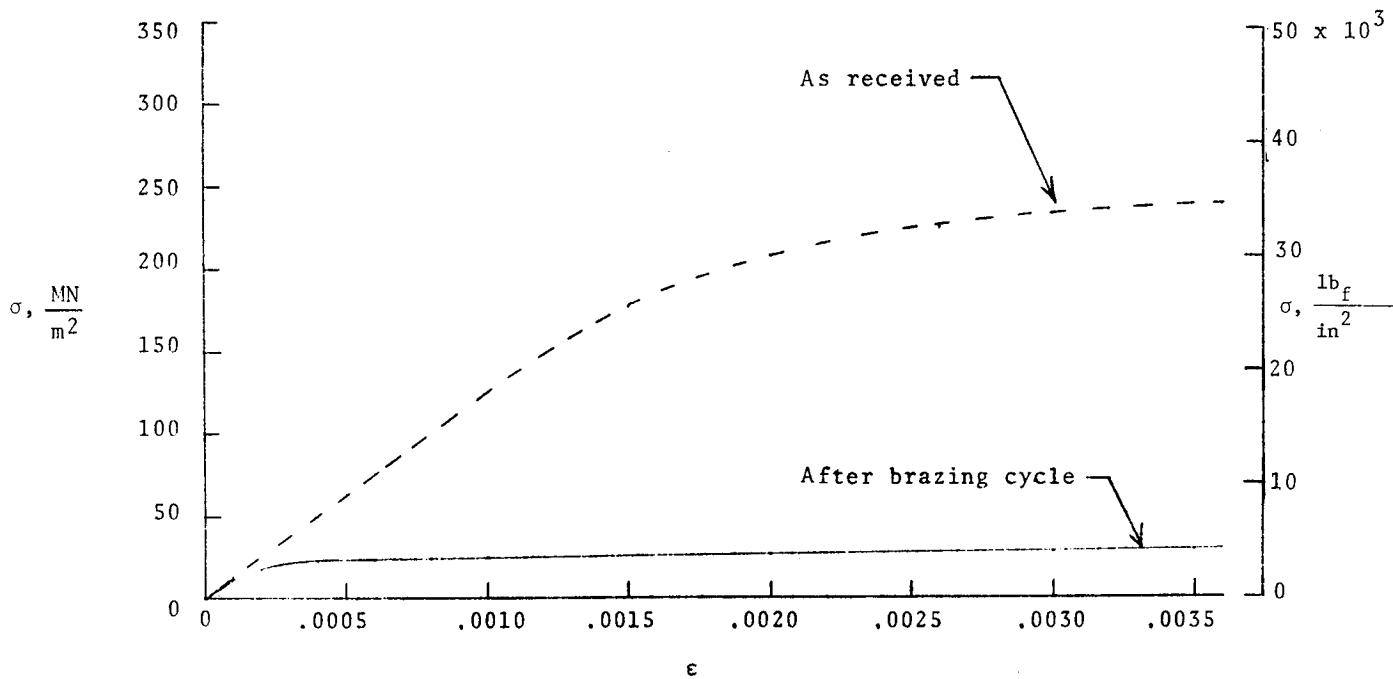


(c) View showing the fuel injection struts in the engine.
Figure 3. - Continued.

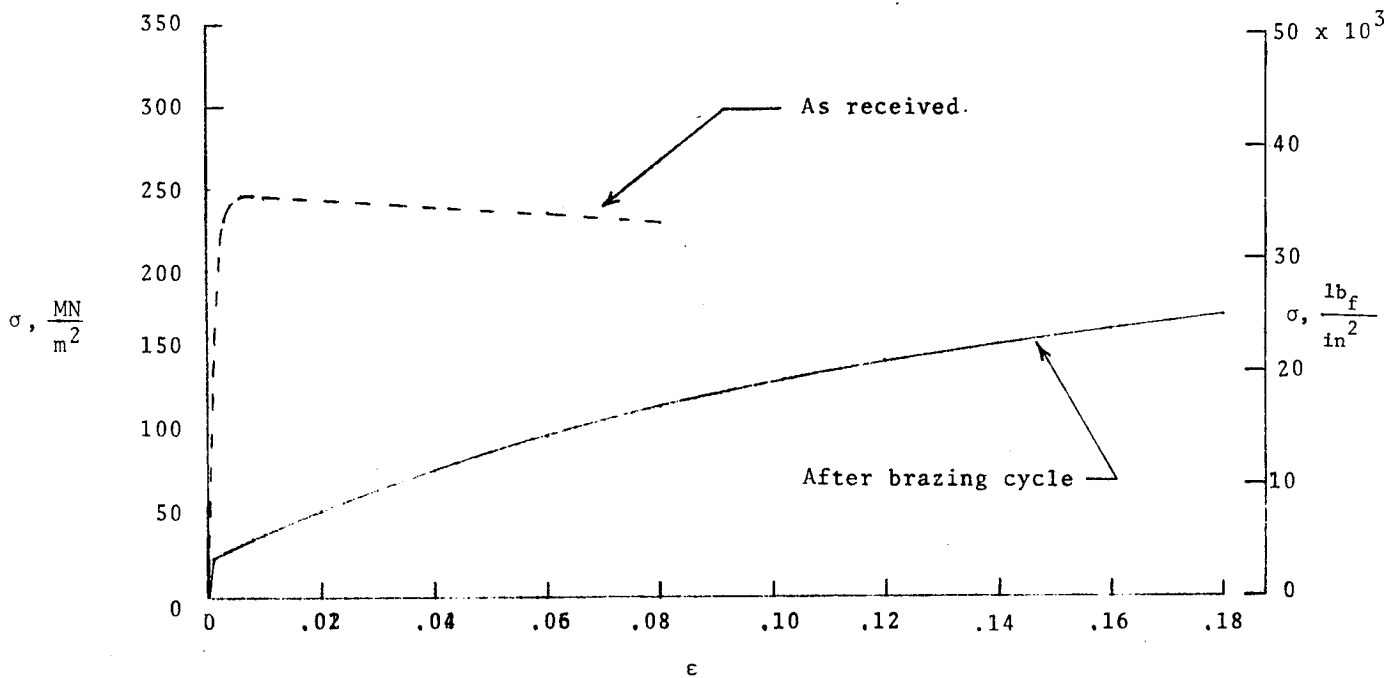
ORIGINAL PAGE IS
OF POOR QUALITY



3d. - Hydrogen fuel injection struts
Figure 3. - Concluded.



a.- Low strain range.



b.- Complete strain range.

Figure 4. - Oxygen-free, high-conductivity copper stress-strain diagram (test temperature = 295 K, 531 R).

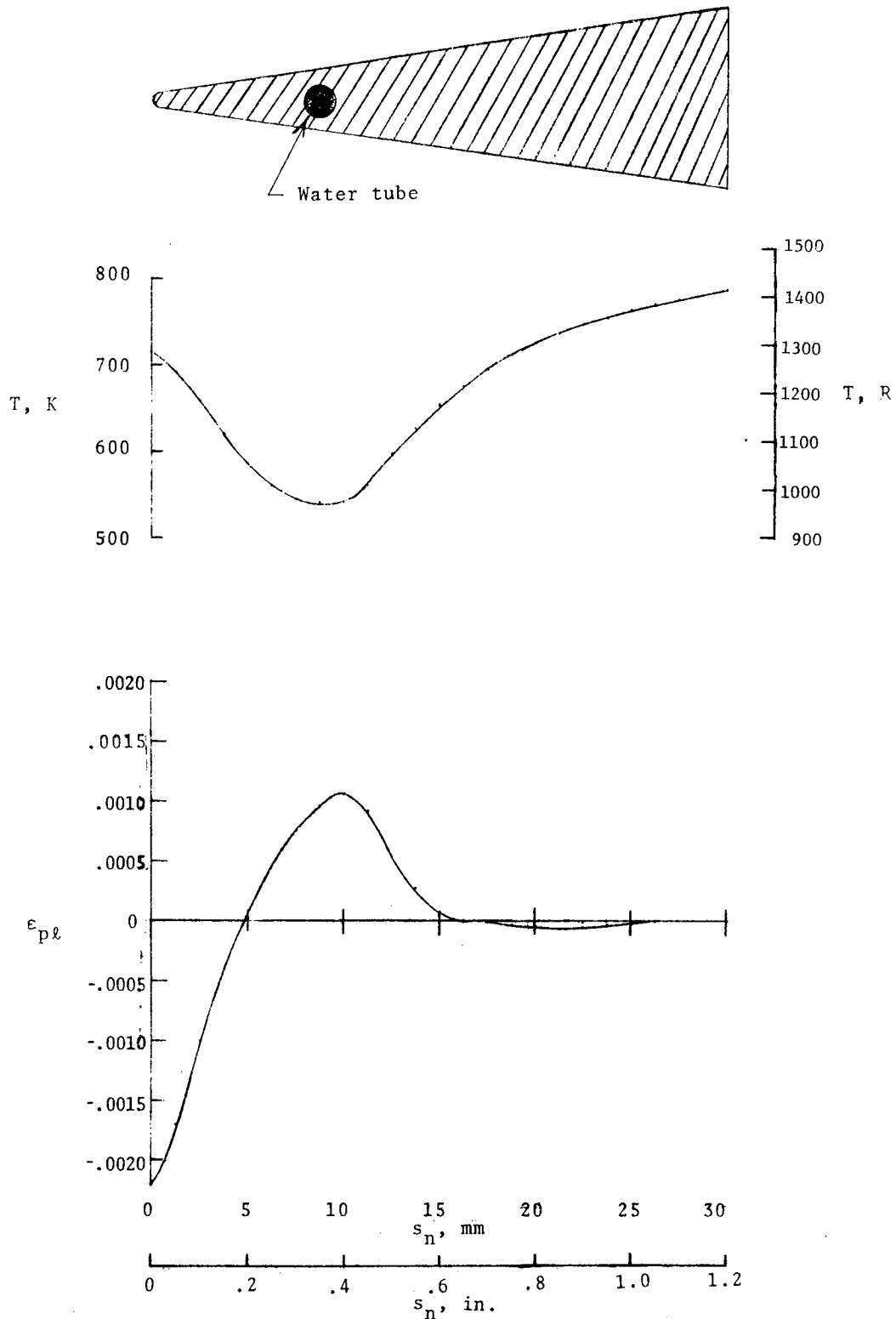
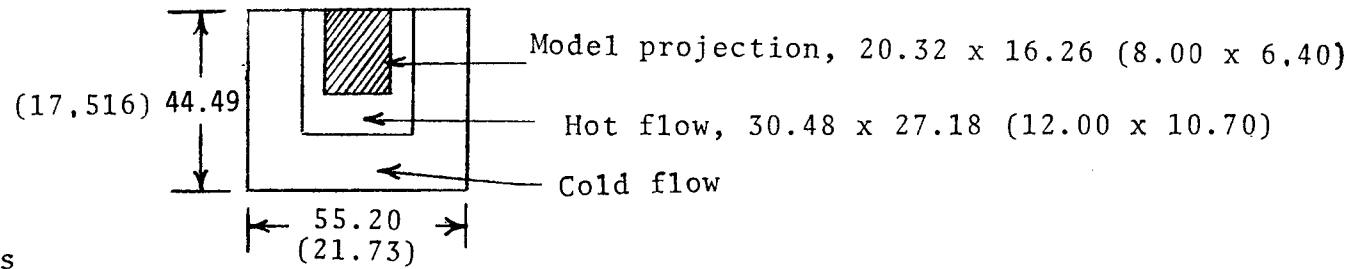


Figure 5.- Temperature and plastic thermal strain distributions from typical test reported in reference 15 (time = 8 sec).



Note:

Dimensions are in centimeters
and inches (parentheses).

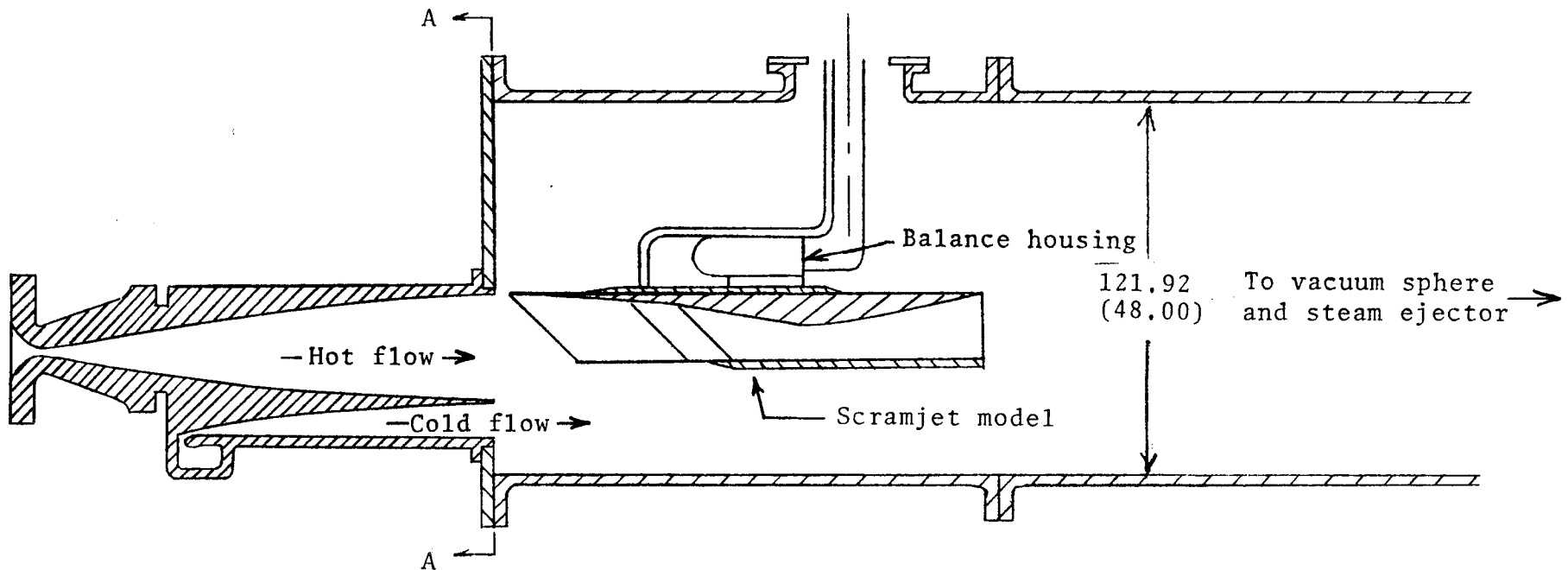


Figure 6. - The scramjet engine model in the testing position in the Scramjet Test Facility.

ORIGINAL PAGE IS
OF POOR QUALITY

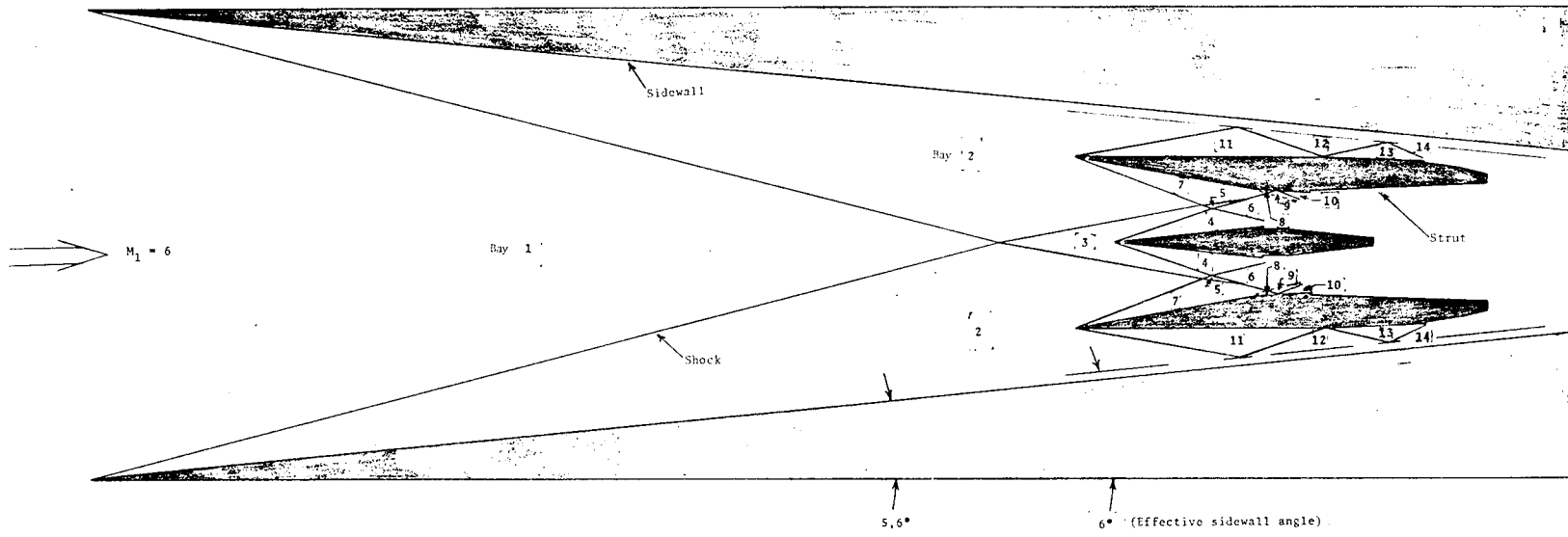
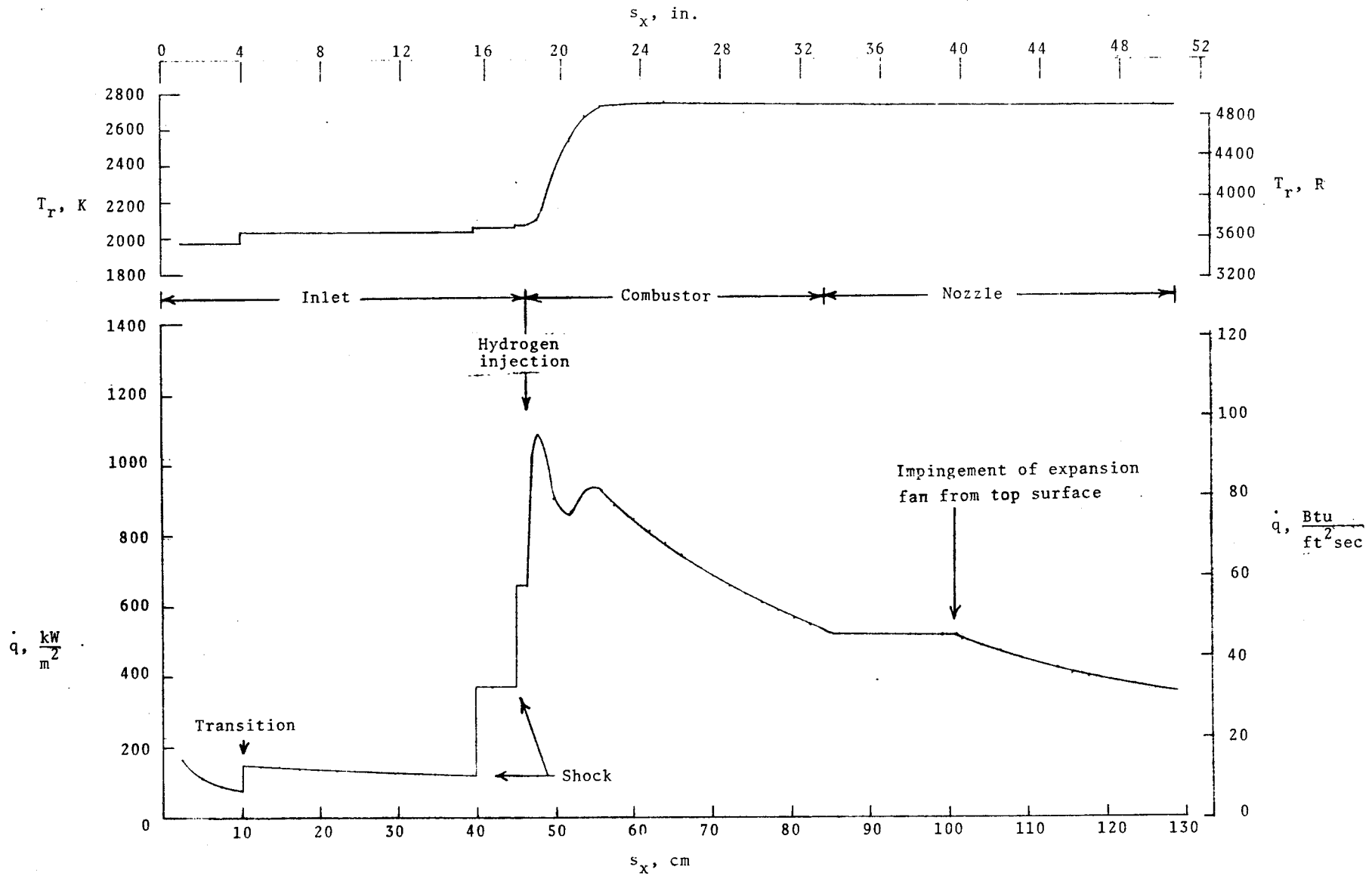


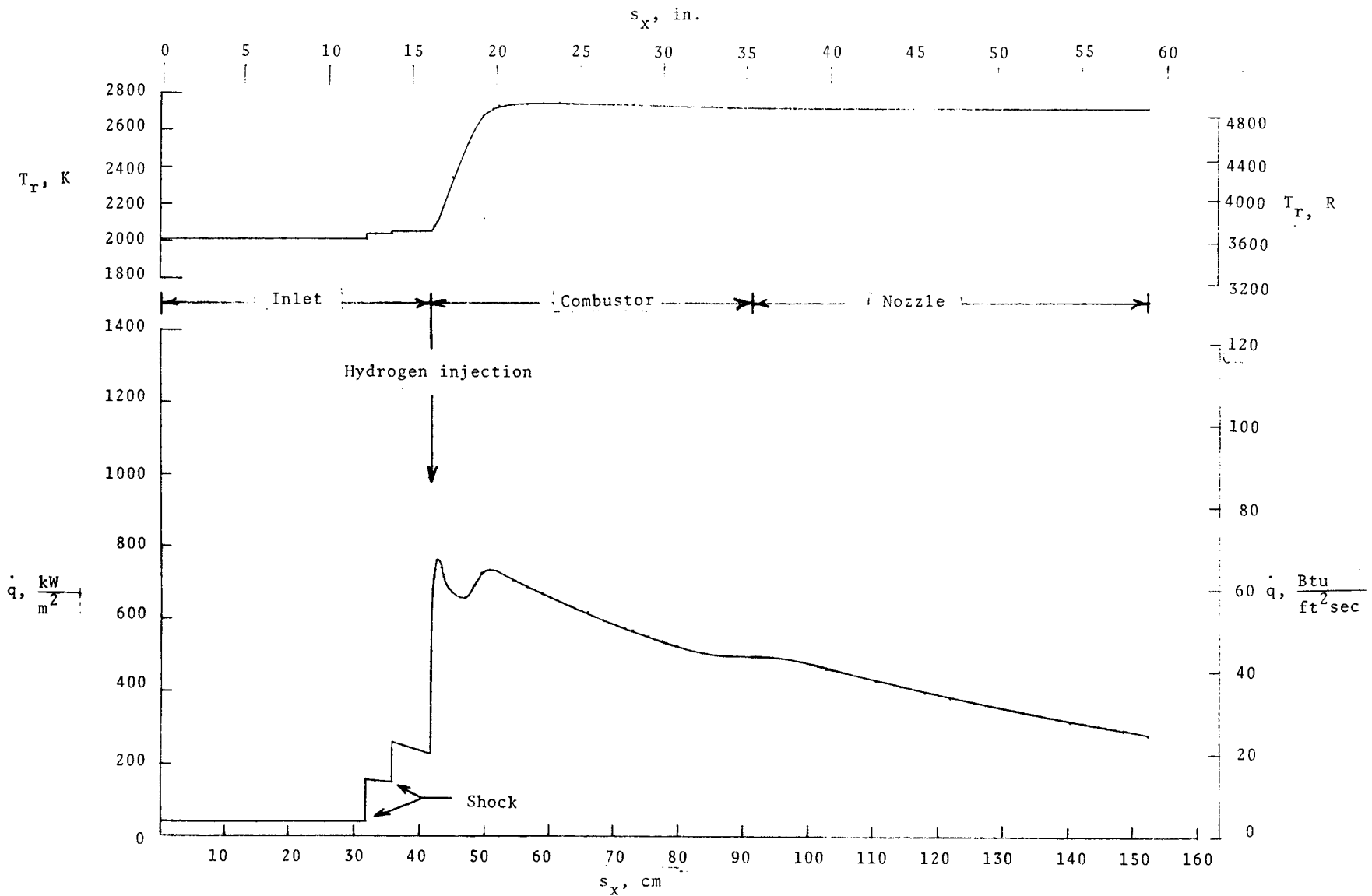
Figure 7. - Calculated wave patterns in the scramjet engine inlet at a Mach number of 6.



a. - Sidewall, $y=13.97$ cm (5.5 in.).

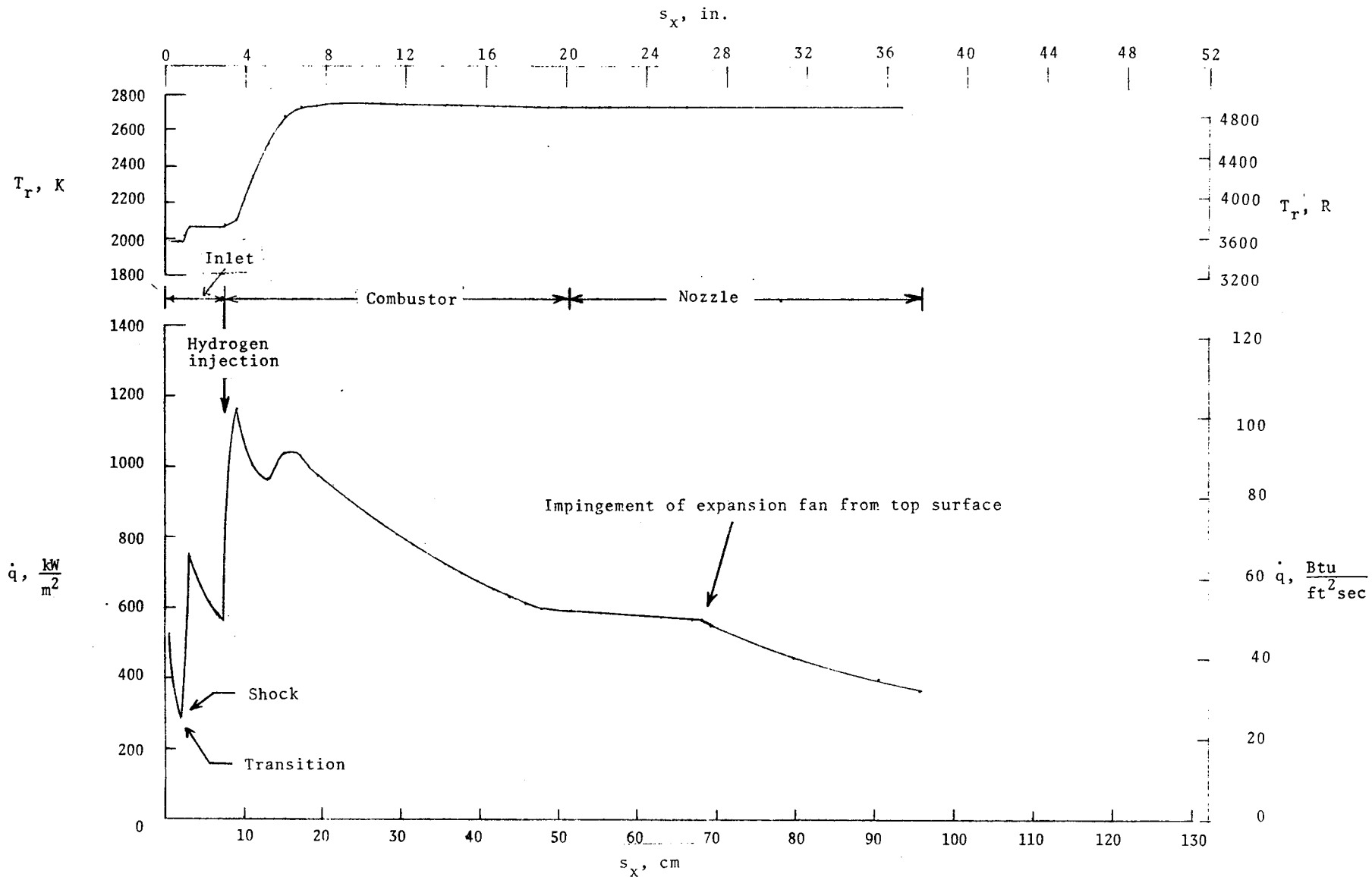
Figure 8. - Calculated heat transfer rate and recovery temperature distributions on the various scramjet engine components, $T_w = 290$ K (522 R), $\phi_f = 1.0$.

FINAL PAGE IS
OF QUALITY



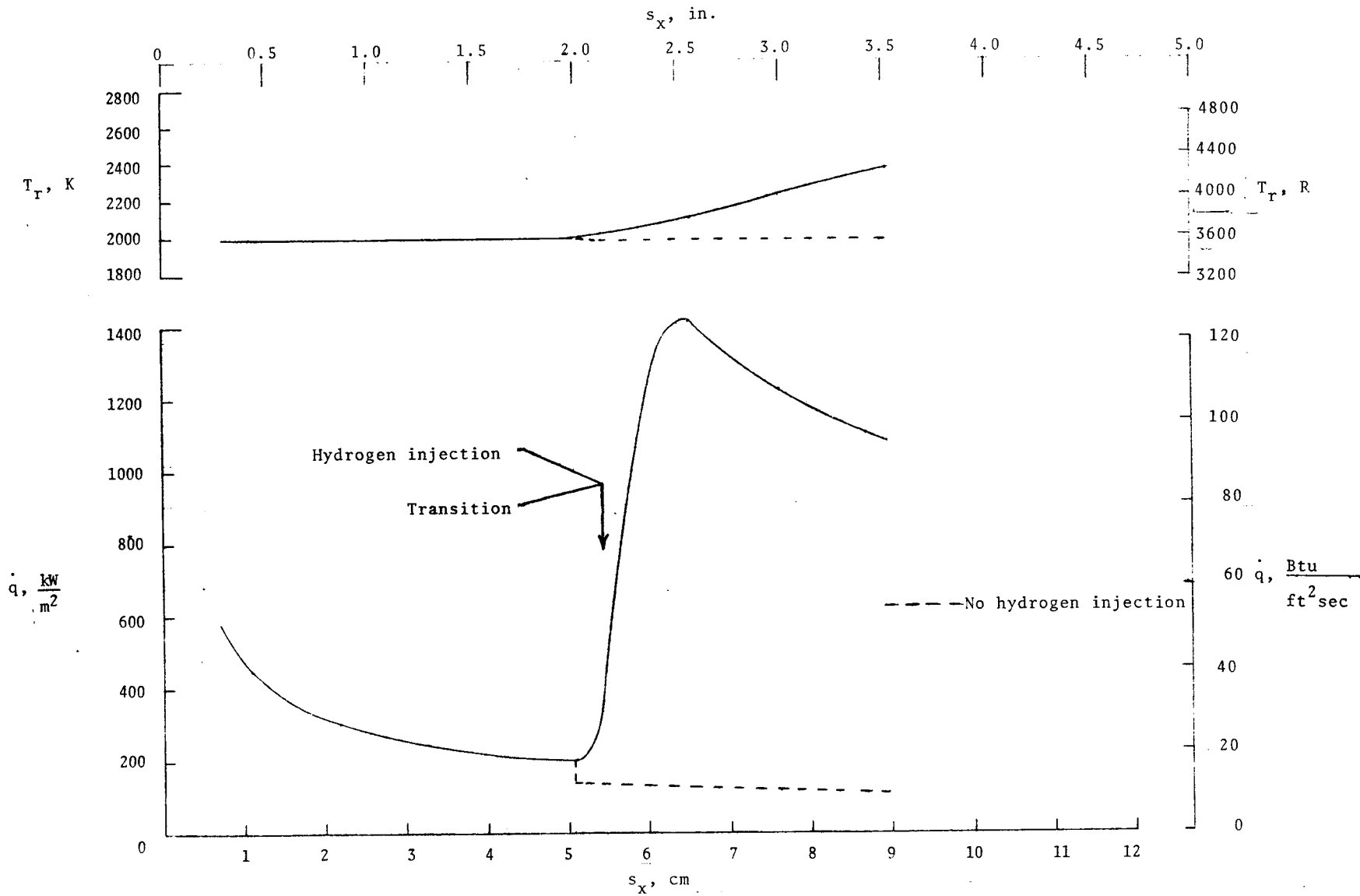
b.- Top surface (centerline), $z = 0$.

Figure 8. - Continued.



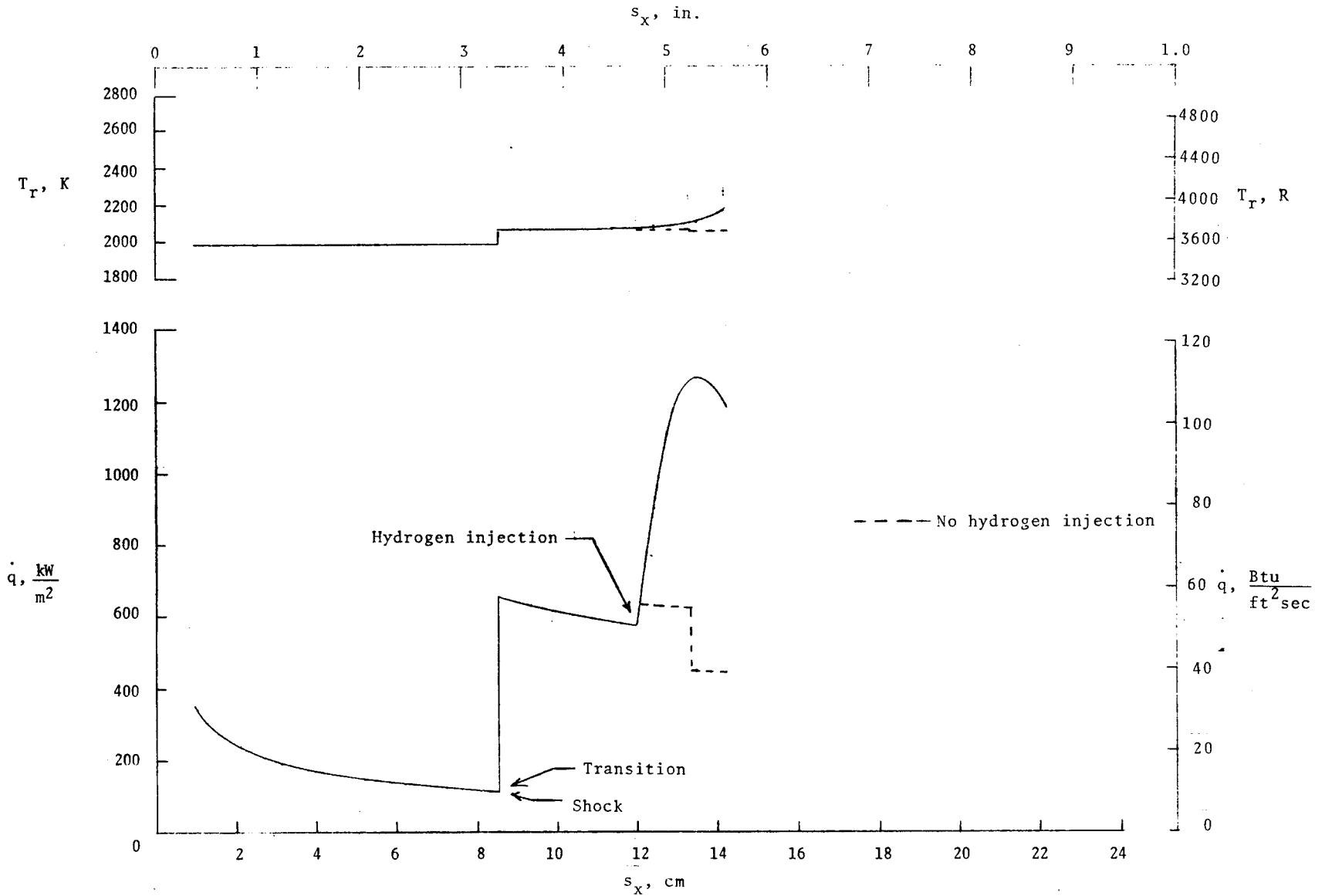
c. - Cowl (centerline), $z = 0$.

Figure 8. - Continued.



d. - Center strut, $y = 10.16$ cm (4.00 in.).

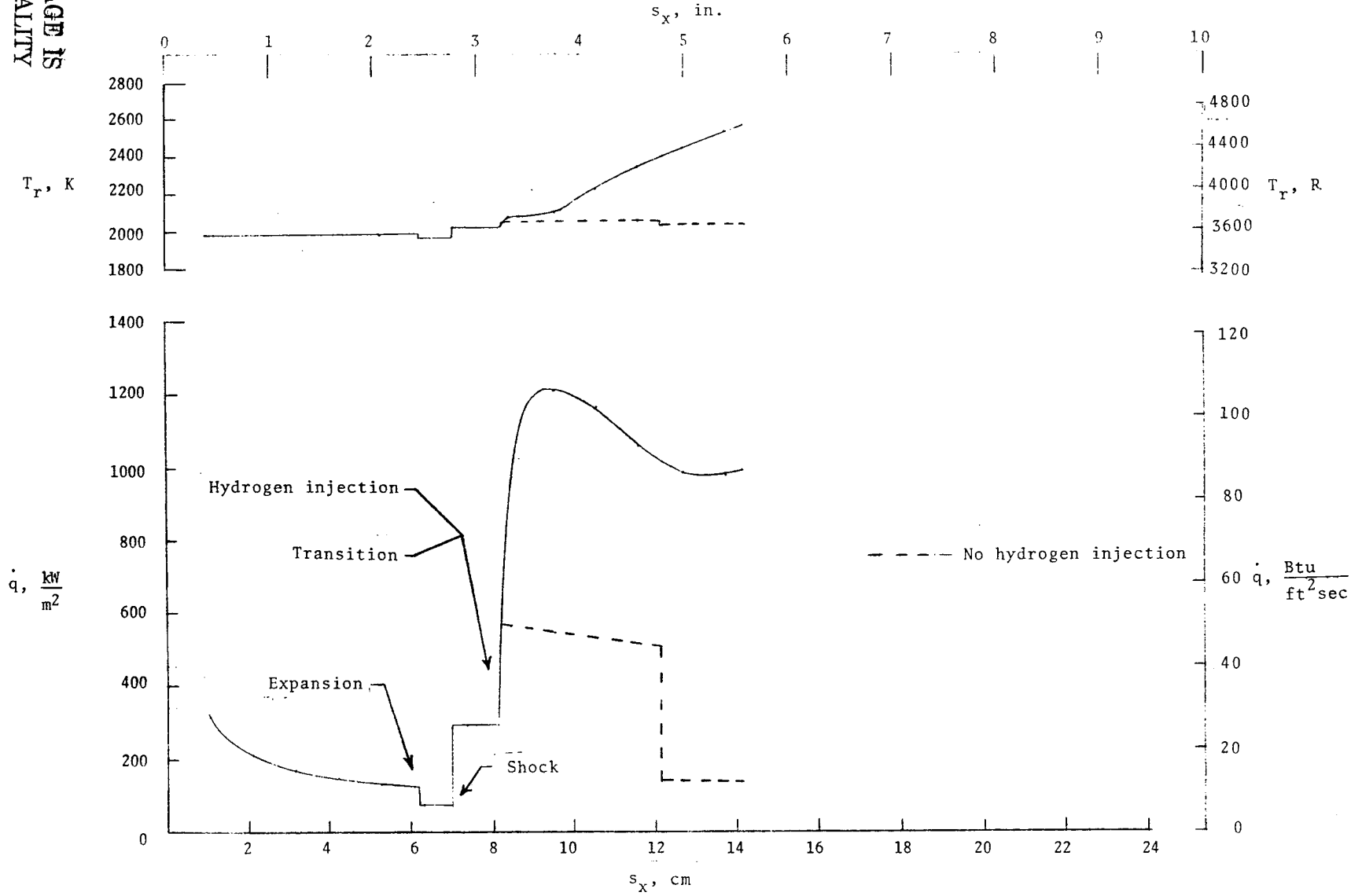
Figure 8. - Continued.



e. - Side strut, side passage, $y^* = 10.16$ cm (4.00 in.).

Figure 8. - Continued.

ORIGINAL PAGE IS
POOR QUALITY



f. - Side strut, center passage, $y = 10.16$ cm (4.00 in.).

Figure 8. - Concluded.

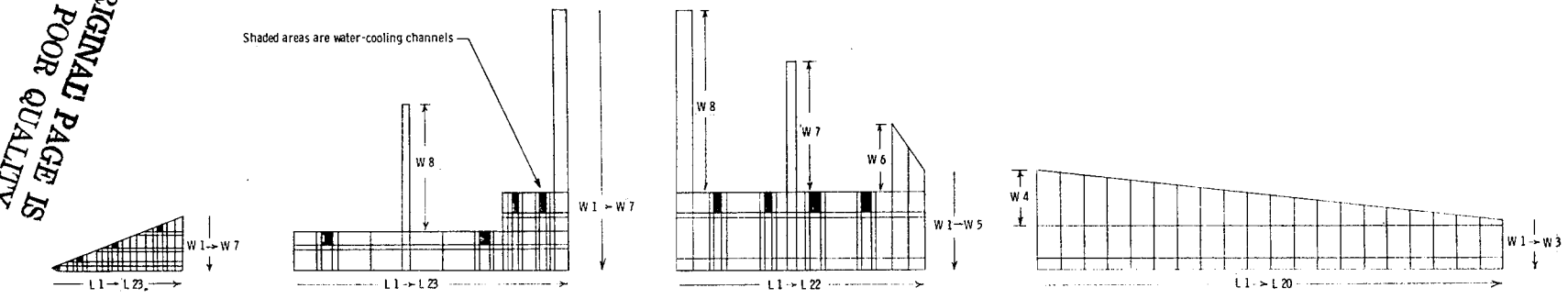
Element	Size	Element	Size
	mm in.		mm in.
L 1	0.011 0.0004	L 16	11.100 0.4370
2	.266 .0105	17	1.750 .0689
3	.266 .0105	18	8.980 .3535
4	3.520 .1386	19	.254 .0100
5	3.520 .1386	20	3.180 .1252
6	.254 .0100	21	.254 .0100
7	1.290 .0508	22	12.600 .4961
8	.254 .0100	23	12.600 .4961
9	10.400 .4094	W 1	5.540 .2181
10	1.730 .0681	2	.254 .0100
11	3.520 .1386	3	4.050 .1594
12	.254 .0100	4	.254 .0100
13	1.300 .0512	5	2.310 .0909
14	.254 .0100	6	.516 .0203
15	11.100 .4370	7	.381 .0150

Element	Size	Element	Size
	mm in.		mm in.
L 1	25.800 1.0157	L 17	0.254 0.0100
2	.254 .0100	18	12.700 .5000
3	9.530 .3752	19	.254 .0100
4	.254 .0100	20	6.350 .2500
5	32.900 1.2953	21	.254 .0100
6	32.900 1.2953	22	4.570 .1799
7	6.350 .2500	23	13.200 .5197
8	33.800 1.3307	W 1	44.500 1.7520
9	33.800 1.3307	2	5.080 .2000
10	.254 .0100	3	.381 .0150
11	9.530 .3752	4	4.060 .1598
12	.254 .0100	5	2.540 .1000
13	15.000 .5906	6	.381 .0150
14	4.570 .1799	7	6.600 .2598
15	.254 .0100	8	31.100 1.2244

Element	Size	Element	Size
	mm in.		mm in.
L 1	15.200 0.5984	L 16	36.300 1.4291
2	16.800 .6614	17	.254 .0100
3	.254 .0100	18	9.530 .3752
4	6.350 .2500	19	.254 .0100
5	.254 .0100	20	17.800 .7008
6	37.100 1.4606	21	14.800 .5827
7	.254 .0100	22	14.800 .5827
8	6.350 .2500	W 1	5.080 .2000
9	.254 .0100	2	5.080 .2000
10	14.000 .5512	3	.254 .0100
11	8.130 .3201	4	12.700 .5000
12	16.000 .6299	5	1.020 .0402
13	.254 .0100	6	16.500 .6496
14	9.530 .3752	7	31.800 1.2520
15	.254 .0100	8	44.500 1.7520

Element	Size	Element	Size
	mm in.		mm in.
L 1	22.400 0.8819	L 13	22.400 0.8819
2		14	
3		15	
4		16	
5		17	
6		18	
7		19	
8		20	
9		W 1	.571 .0225
10		2	10.200 .4016
11		3	1.270 .0500
12		4	12.700 .5000

ORIGINAL PAGE IS OF POOR QUALITY



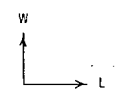
Leading edge segment (99 elements)
(Model is normal to sweep line)

Inlet segment (97 elements)
(Model is normal to sweep line)

Combustor segment (88 elements)
(Model is normal to sweep line)

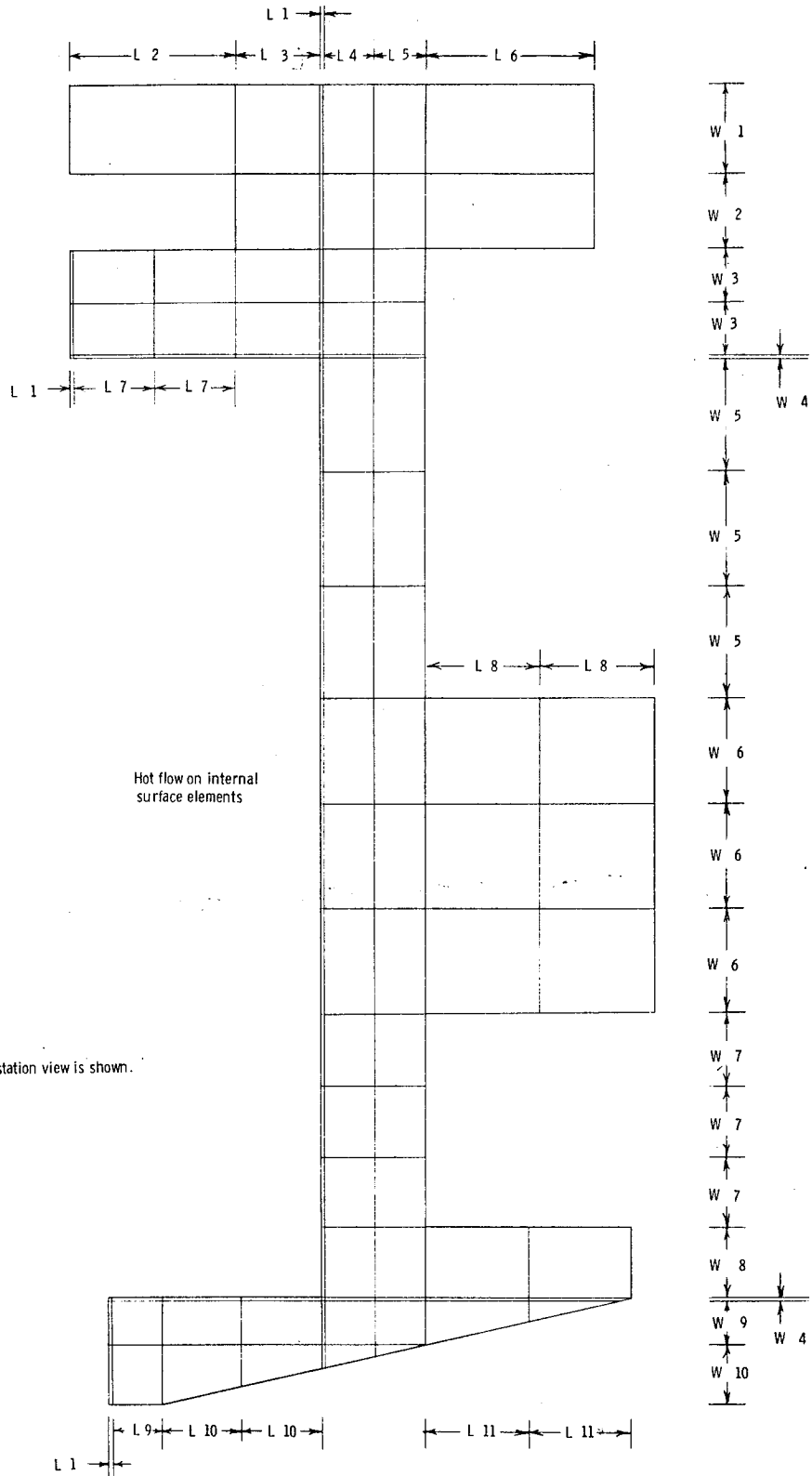
Nozzle segment (50 elements)
(Model is parallel to cowl plate)

Note: Drawings are not to scale.



a. - Segmented sidewall.

Figure 9. - Computer thermal models of the scramjet engine model.



Element	Size	
	mm	in.
L 1	0.305	0.012
2	29.800	1.173
3	14.900	.587
4	9.370	.369
5	7.590	.299
6	30.200	1.189
7	14.800	.583
8	20.600	.811
9	9.220	.363
10	14.300	.563
11	18.400	.724
W 1	15.600	.614
2	13.500	.531
3	9.370	.369
4	.305	.012
5	20.200	.795
6	18.600	.732
7	12.600	.496
8	12.700	.500
9	8.000	.315
10	10.700	.421

Note: 1. Only one-half of symmetrical station view is shown.
 2. Model has 95 elements.

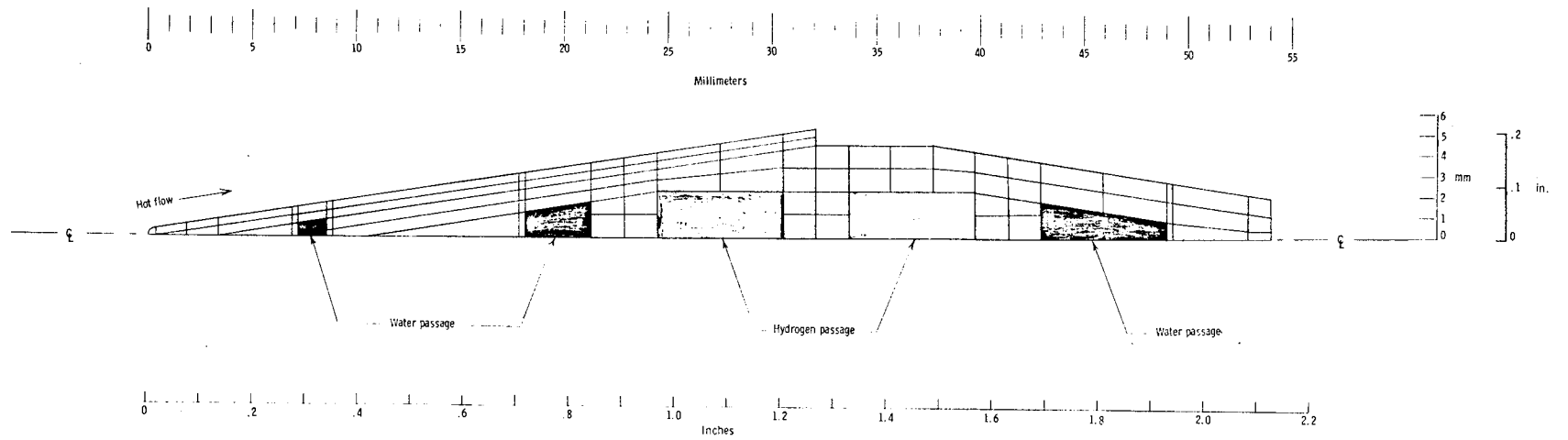
ORIGINAL PAGE IS
 OF POOR QUALITY

ORIGINAL PAGE IS
 OF POOR QUALITY

b. - Station 66.55 cm, 26.2 in.
 Figure 9. - Continued.

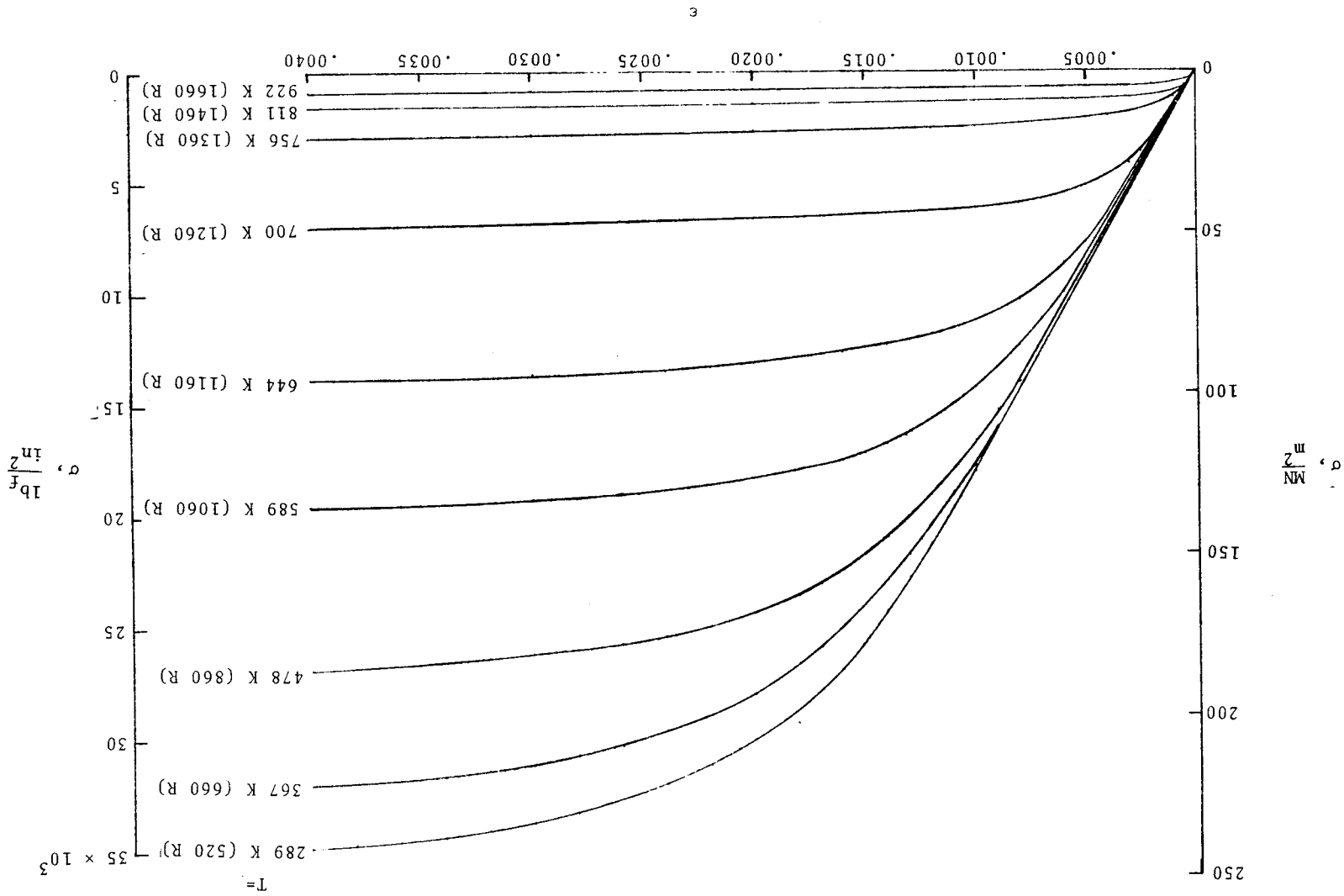
8

Note: 1. Half-section view of strut is normal to strut leading edge.
2. Drawing is to scale.
3. Model has 88 elements.

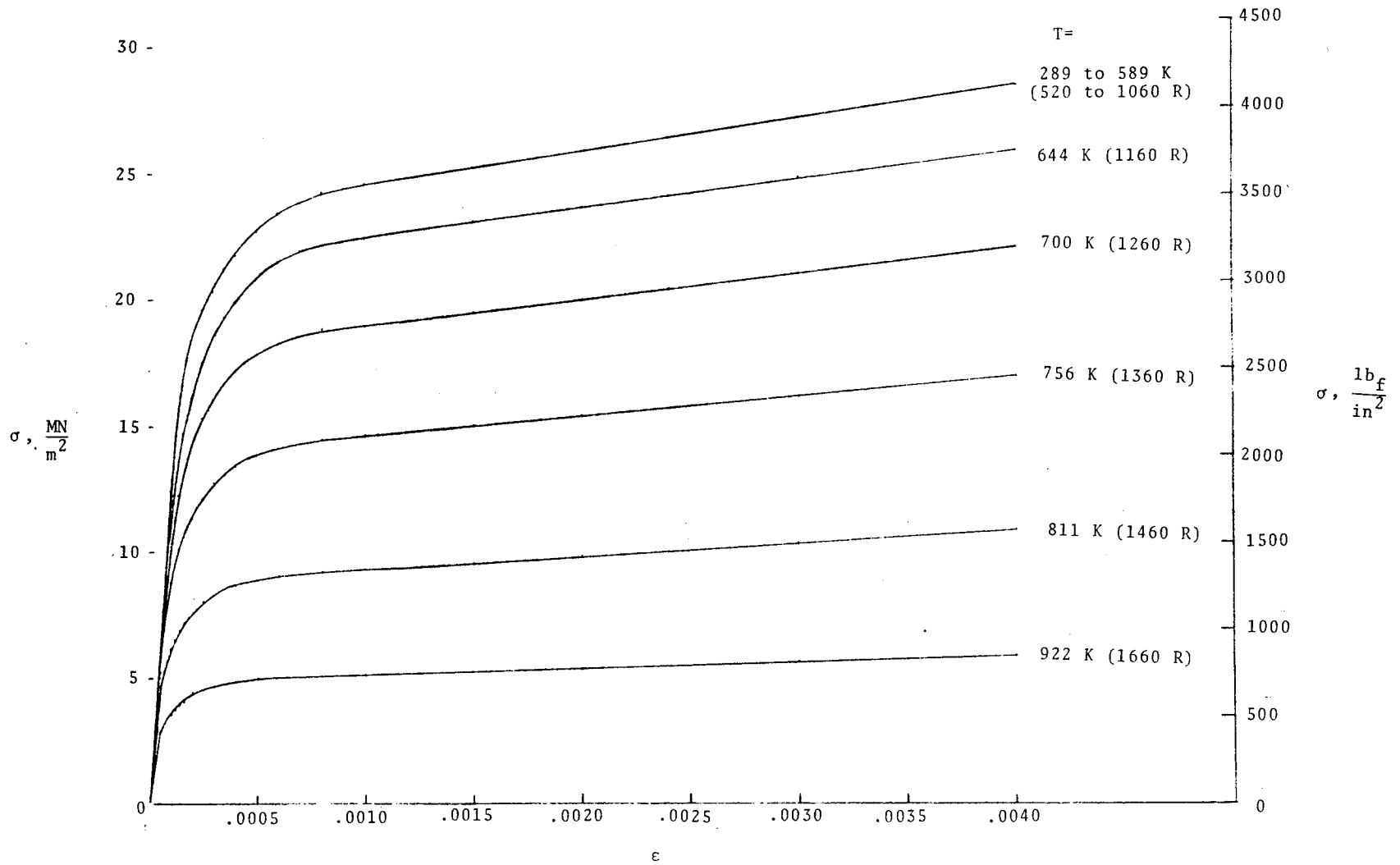


c - Center hydrogen strut.

Figure 9. - Concluded.



a. Unannealed copper.
 Figure 10. - Approximate stress-strain curves for oxygen-free, high-conductivity copper at several temperature levels.



b. Annealed copper.

Figure 10. - Concluded.

ORIGINAL PAGE IS
OF POOR QUALITY

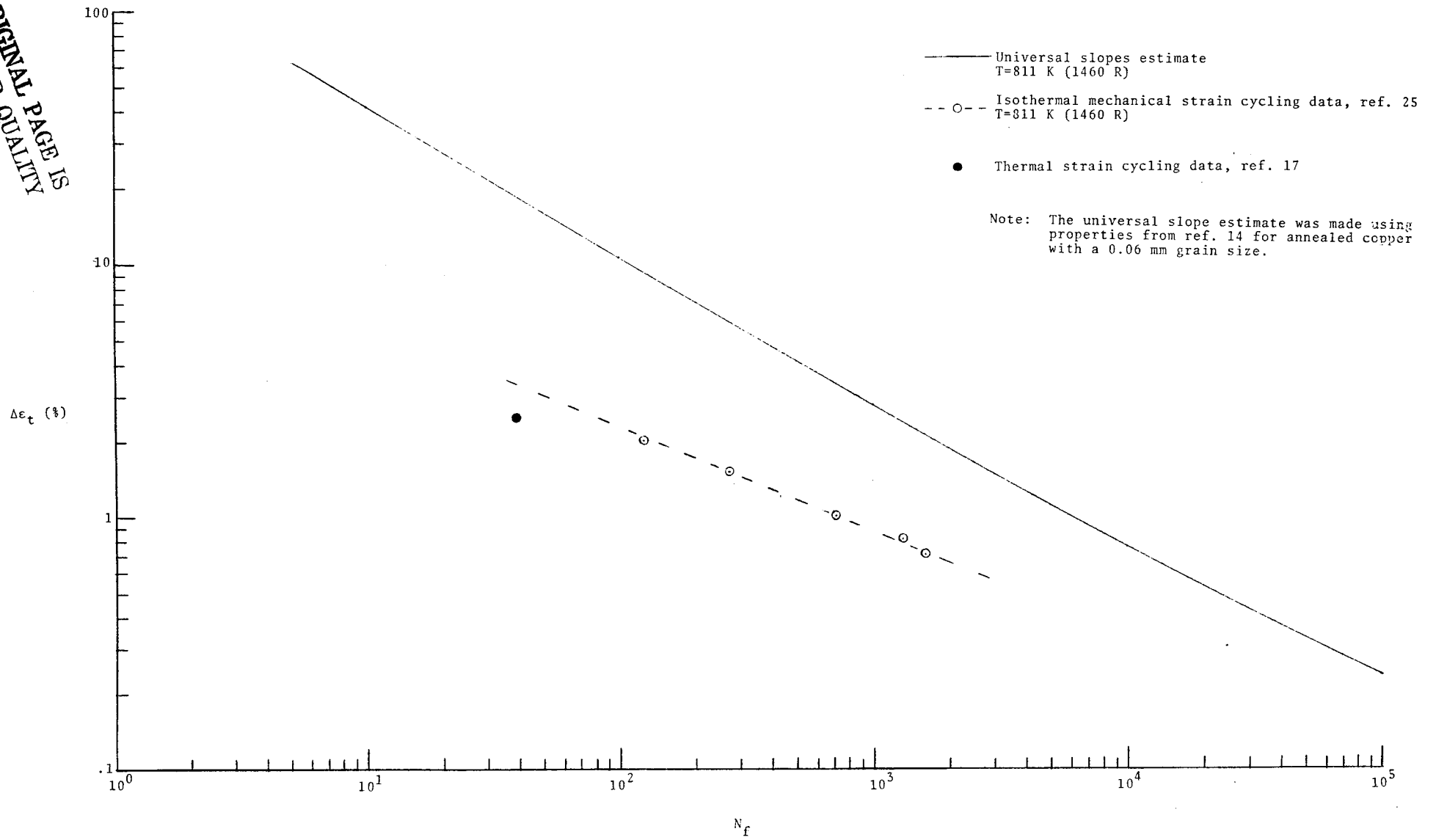


Figure 11. - Cycle life of annealed oxygen-free, high-conductivity copper.

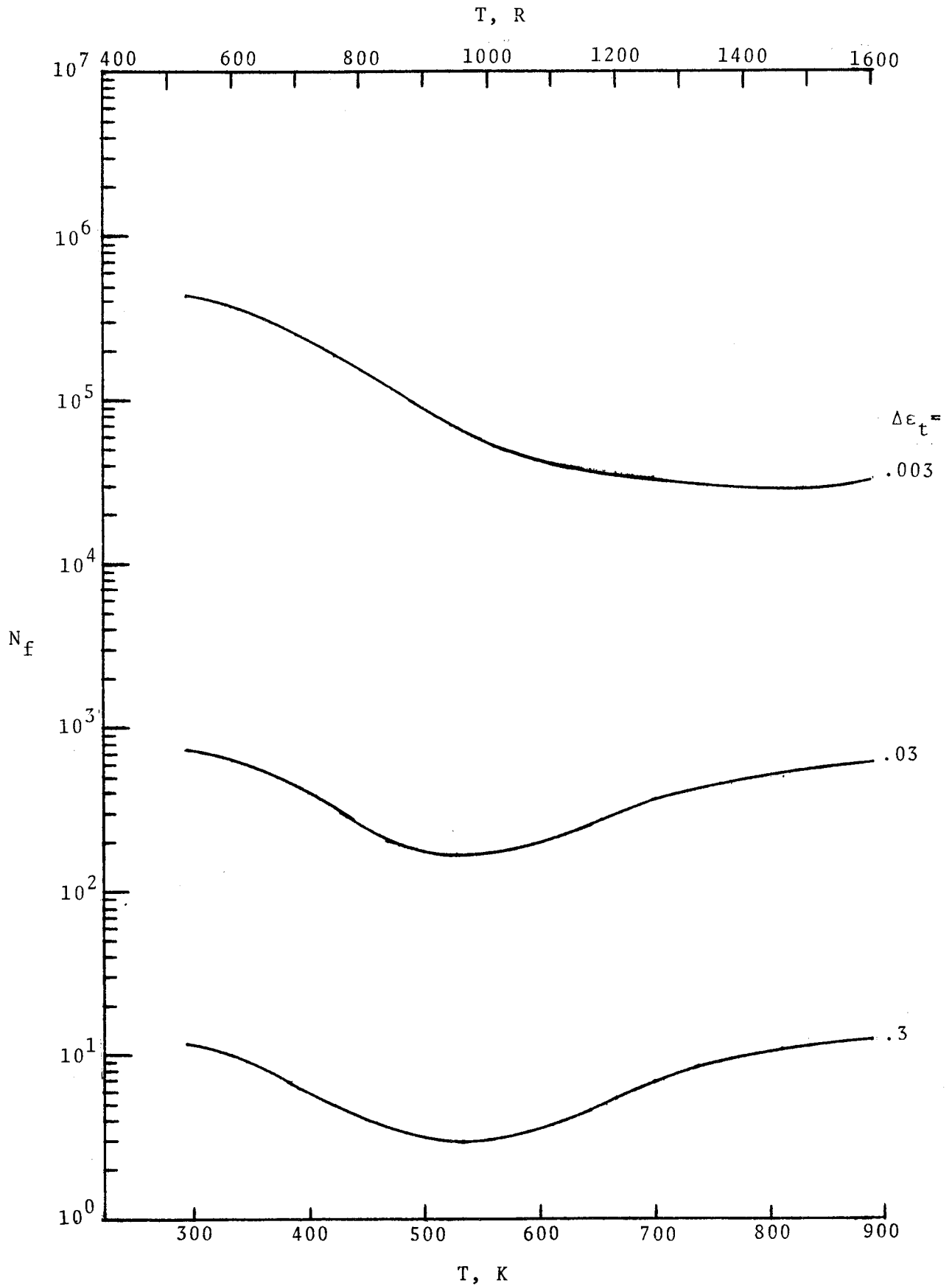
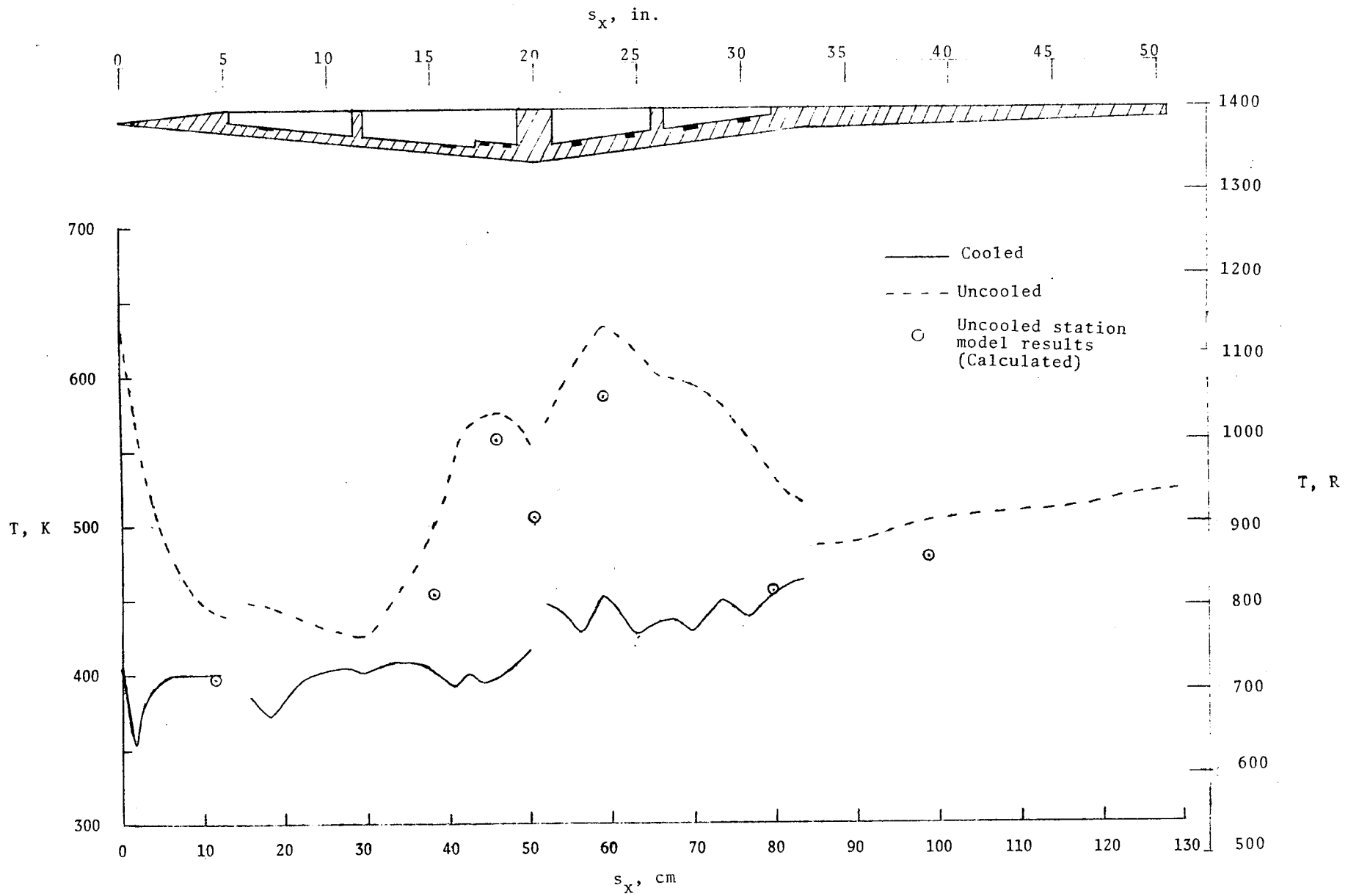
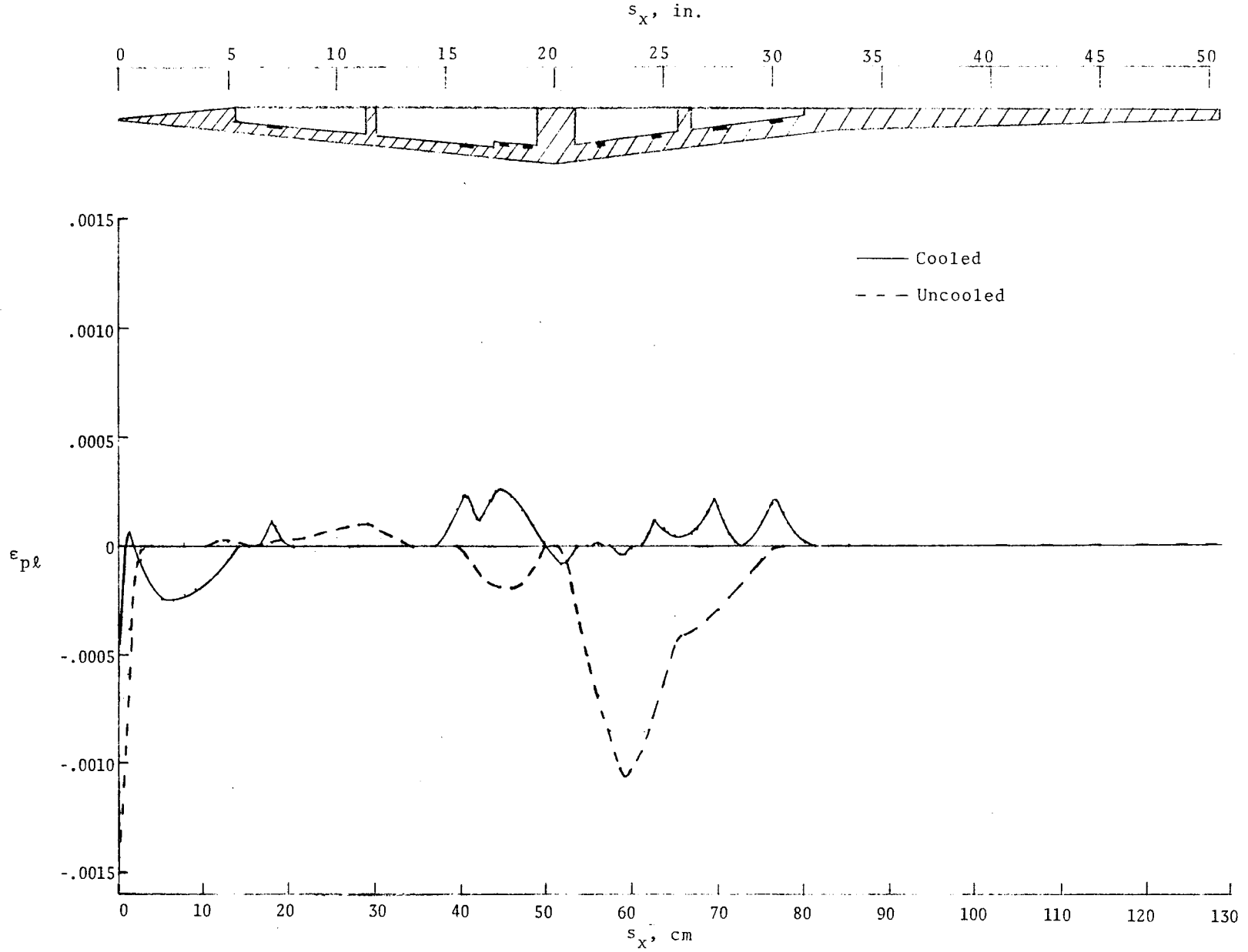


Figure 12. - Cycle life estimates for hard-drawn oxygen-free, high-conductivity copper using the universal slopes method.



a. - Temperature distribution.

Figure 13.- Calculated thermal condition of the sidewall of the scramjet model after 30 seconds of testing.



b. - Plastic strain distribution.

Figure 13. - Concluded.

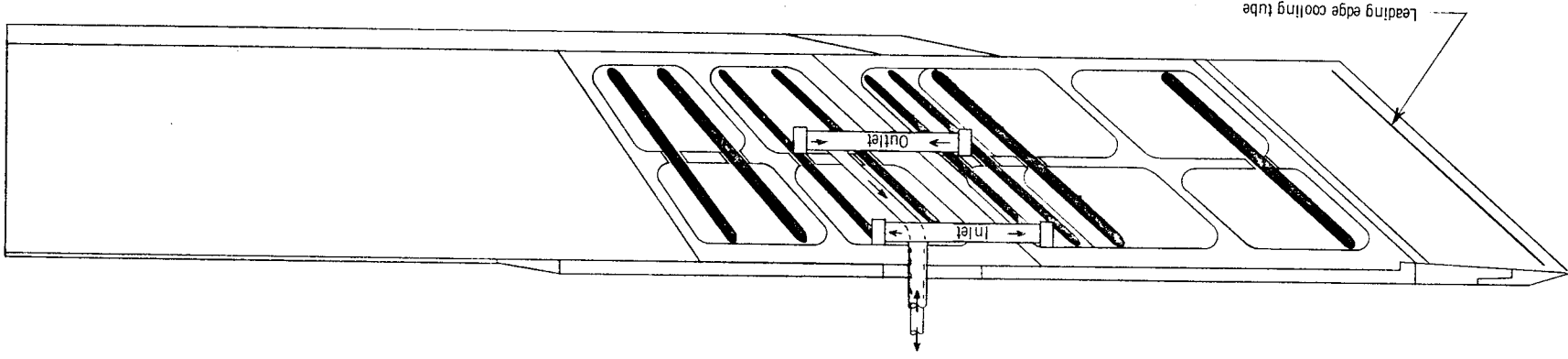


Figure 14. - Scramjet engine model sidewall cooling-water network.

Note: 1. Sidewall cover plate is removed.
 2. Individual cover plates over each cooling channel are removed.
 3. Water lines from the inlet and outlet manifolds to the cooling channels are not shown. However, cooling water enters at the tops of the channels and exits at the bottom where the flow rate is controlled by miniature valves on each channel.

ORIGINAL PAGE IS
 OF POOR QUALITY

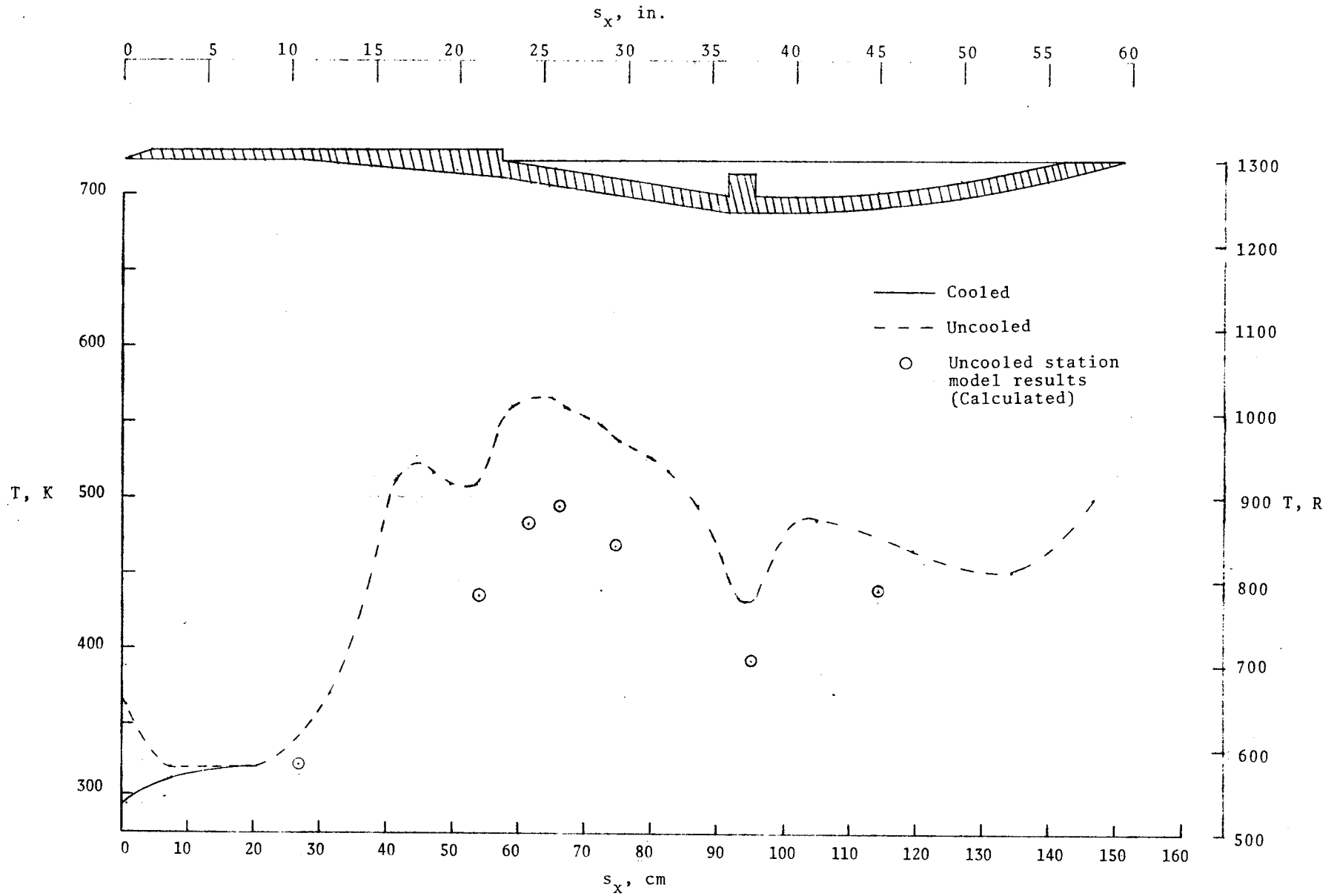


Figure 15.- Calculated temperature distribution along the centerline of the top surface of the scramjet model after 30 seconds of testing.

ORIGINAL PAGE IS
OF POOR QUALITY

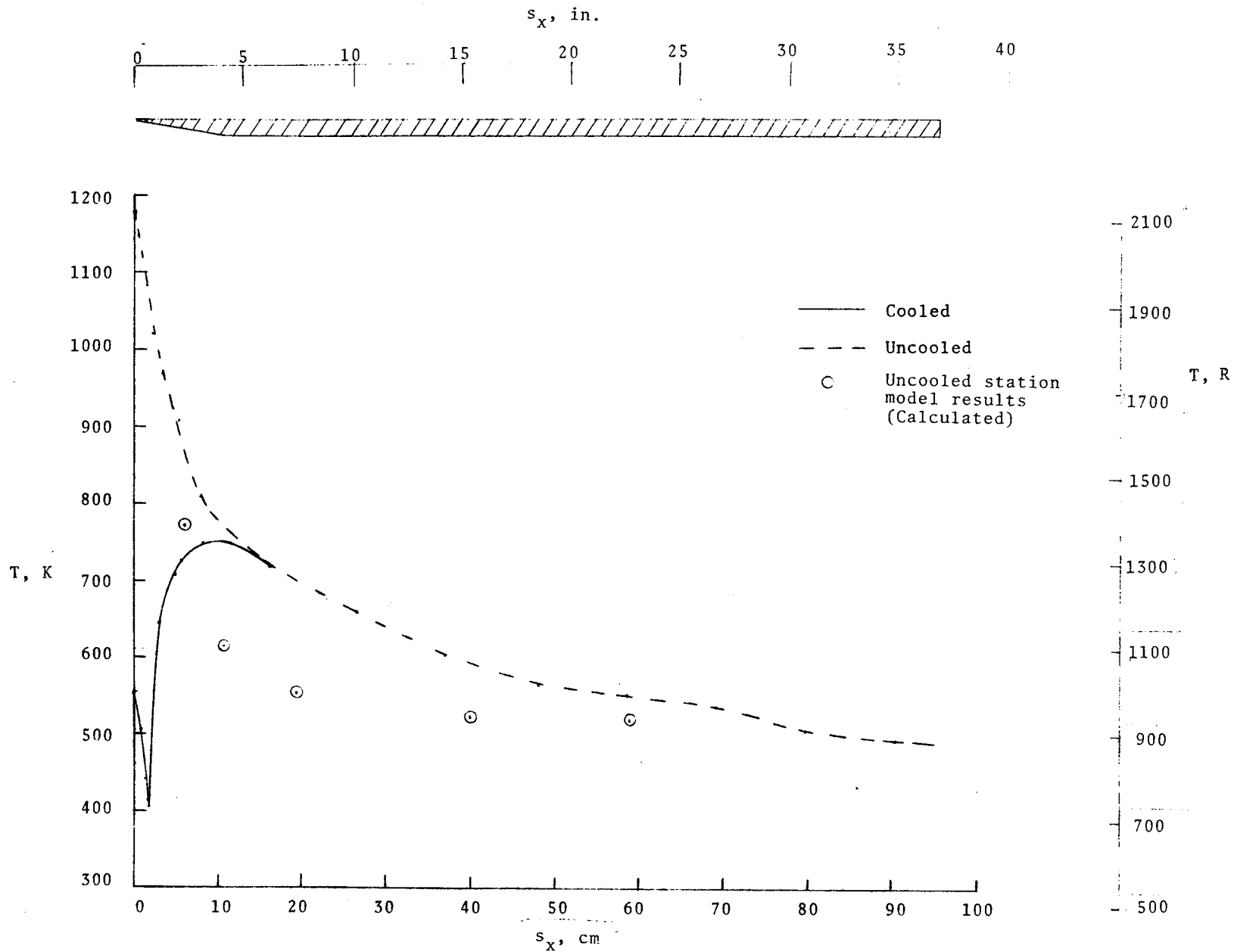
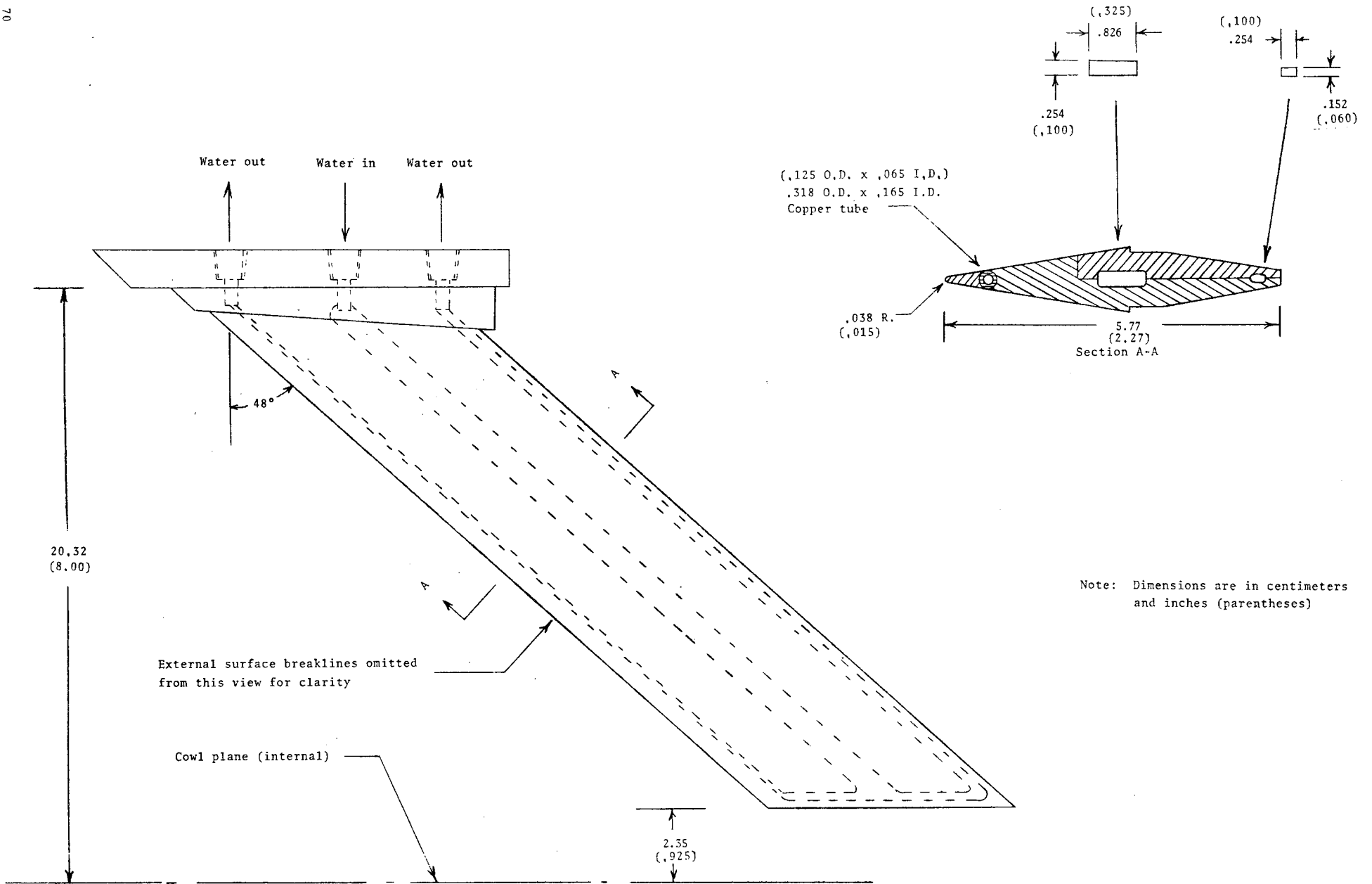
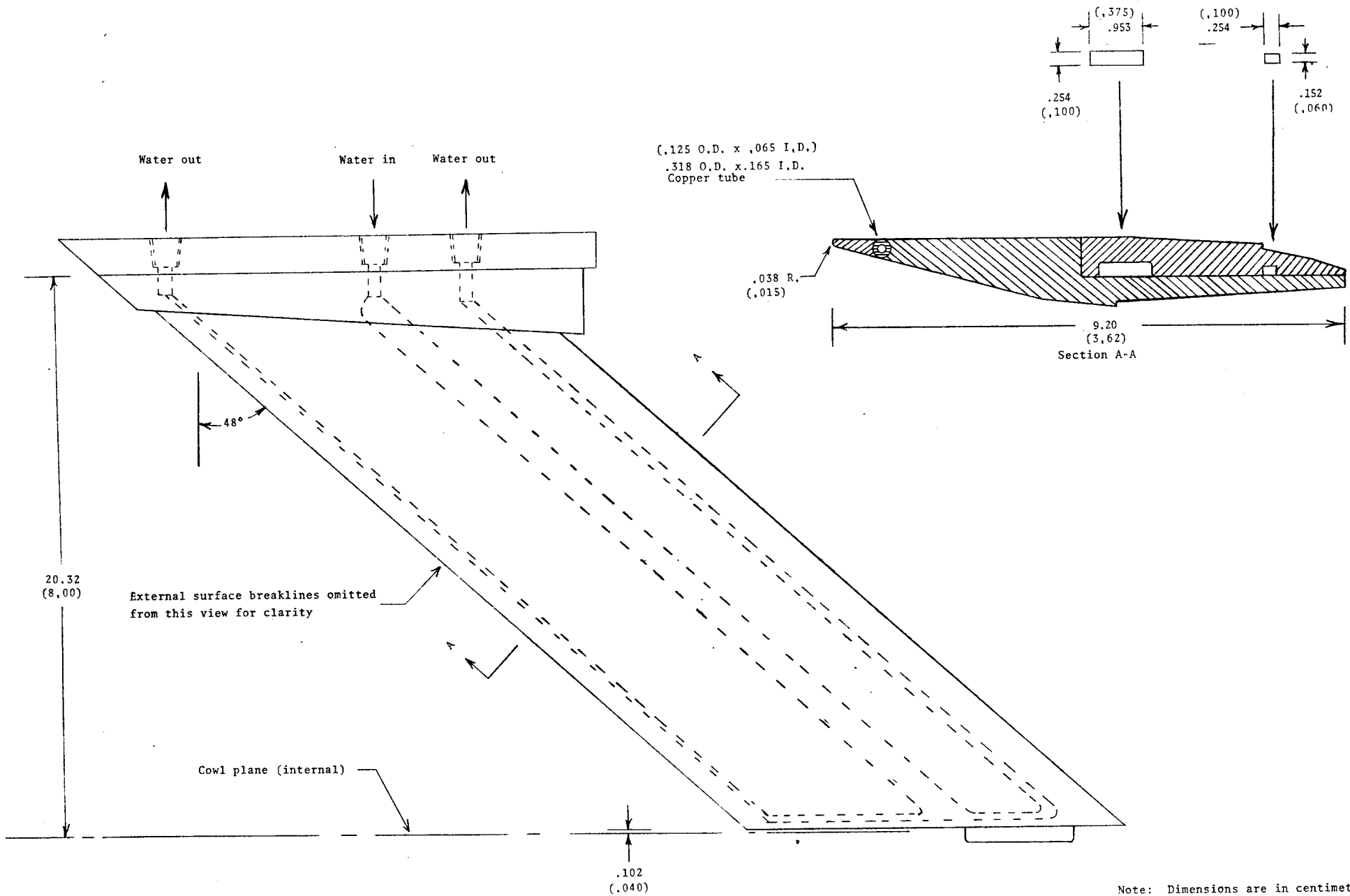


Figure 16. - Calculated temperature distribution along the centerline of the cowl of the scramjet model after 30 seconds of testing.



a.- Center strut.

Figure 17. - Coolant routing for the scramjet model struts.



Note: Dimensions are in centimeters
and inches (parentheses)

b.- Side strut.
Figure 17.- Concluded.

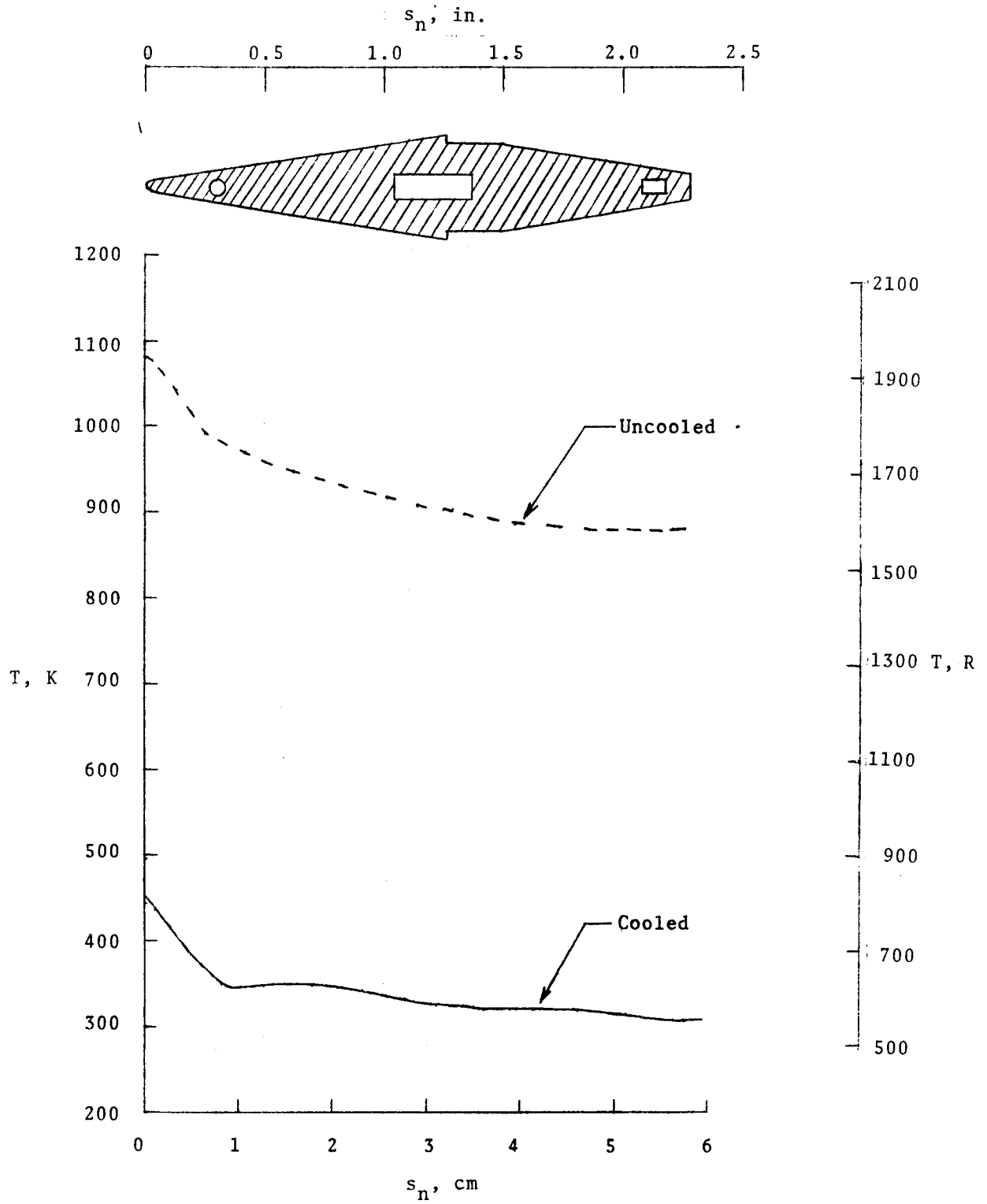


Figure 18.- Calculated temperature distribution along the center strut after 30 seconds of testing.

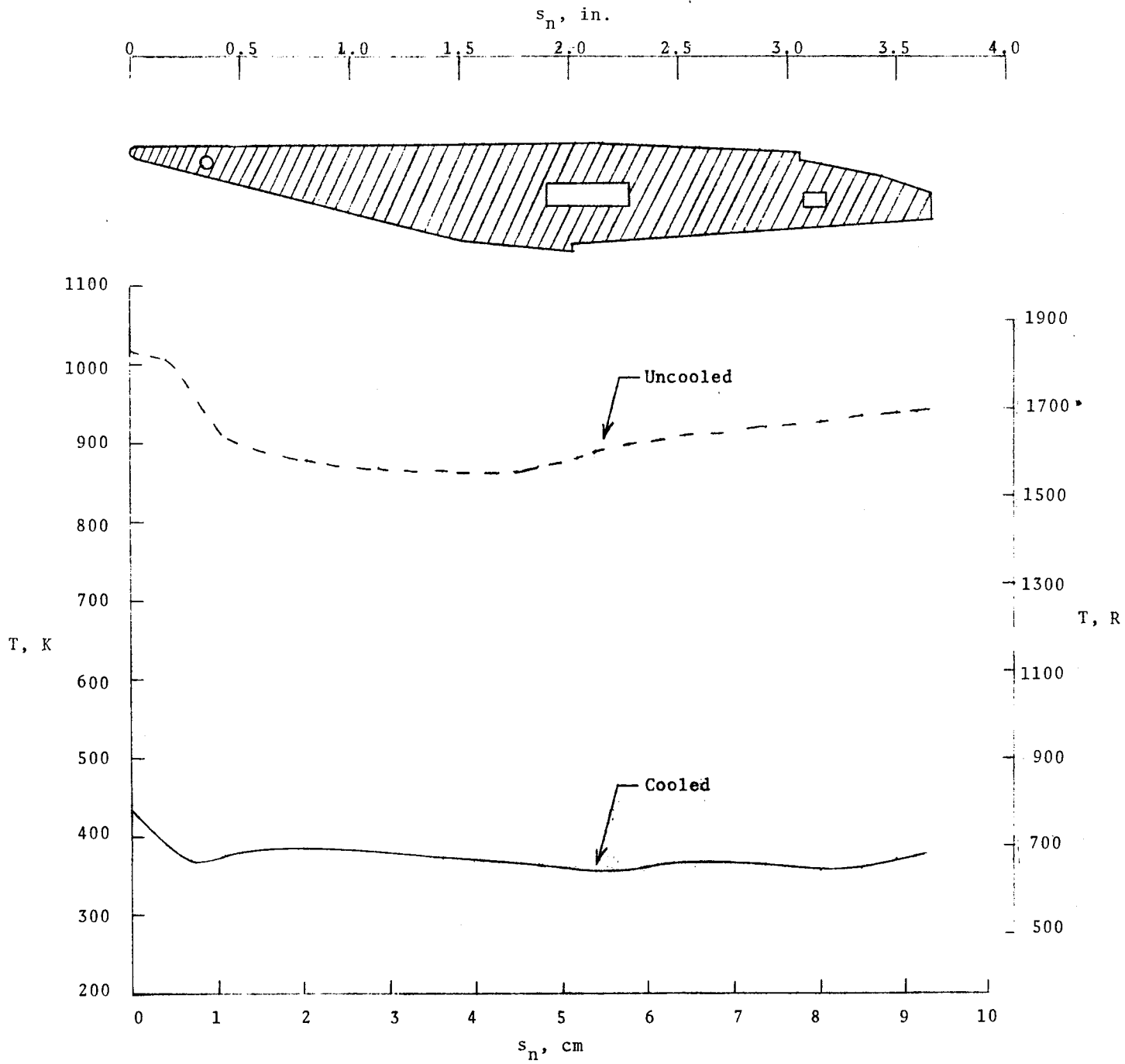
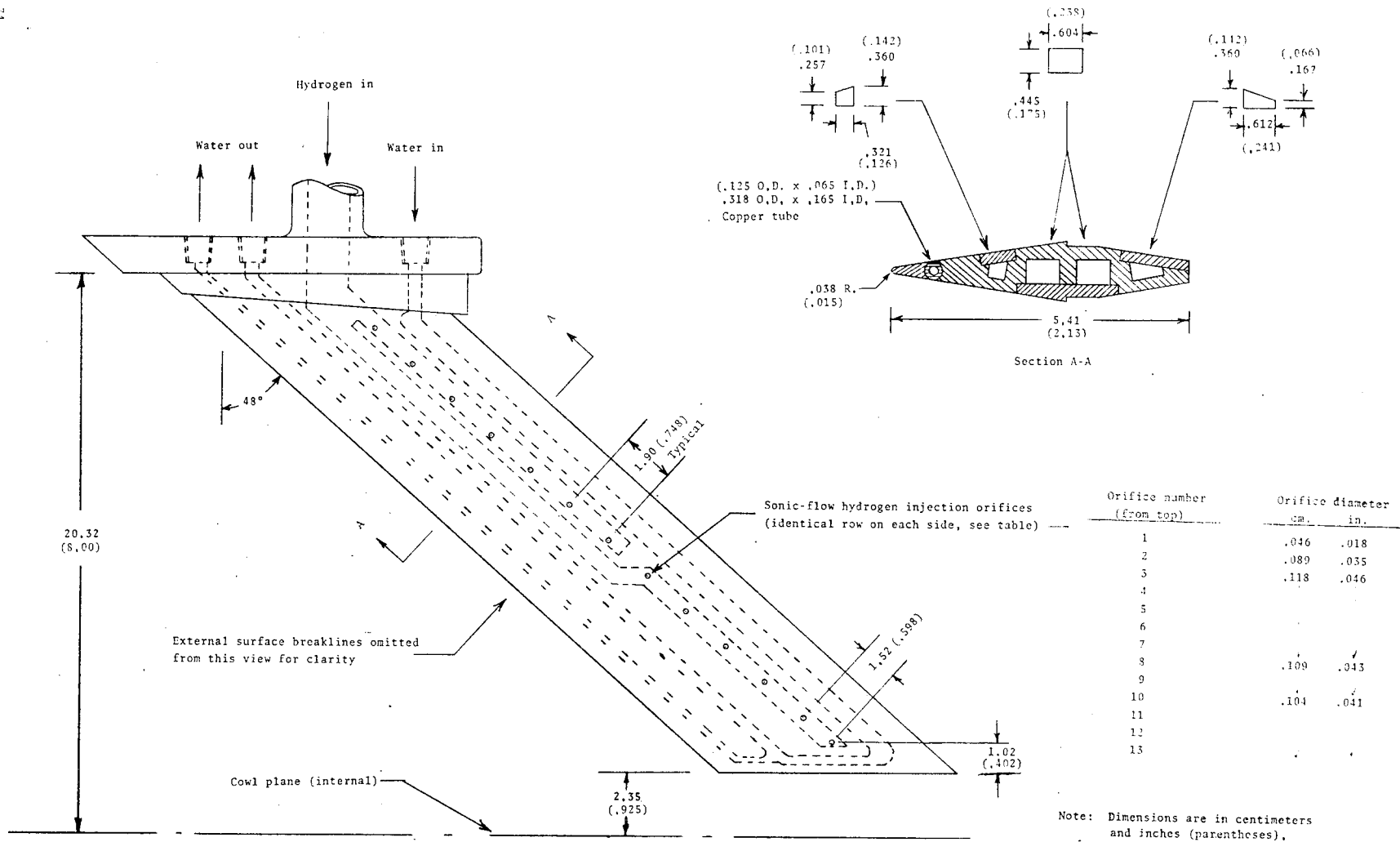


Figure 19.- Calculated temperature distribution along the side strut after 30 seconds of testing.

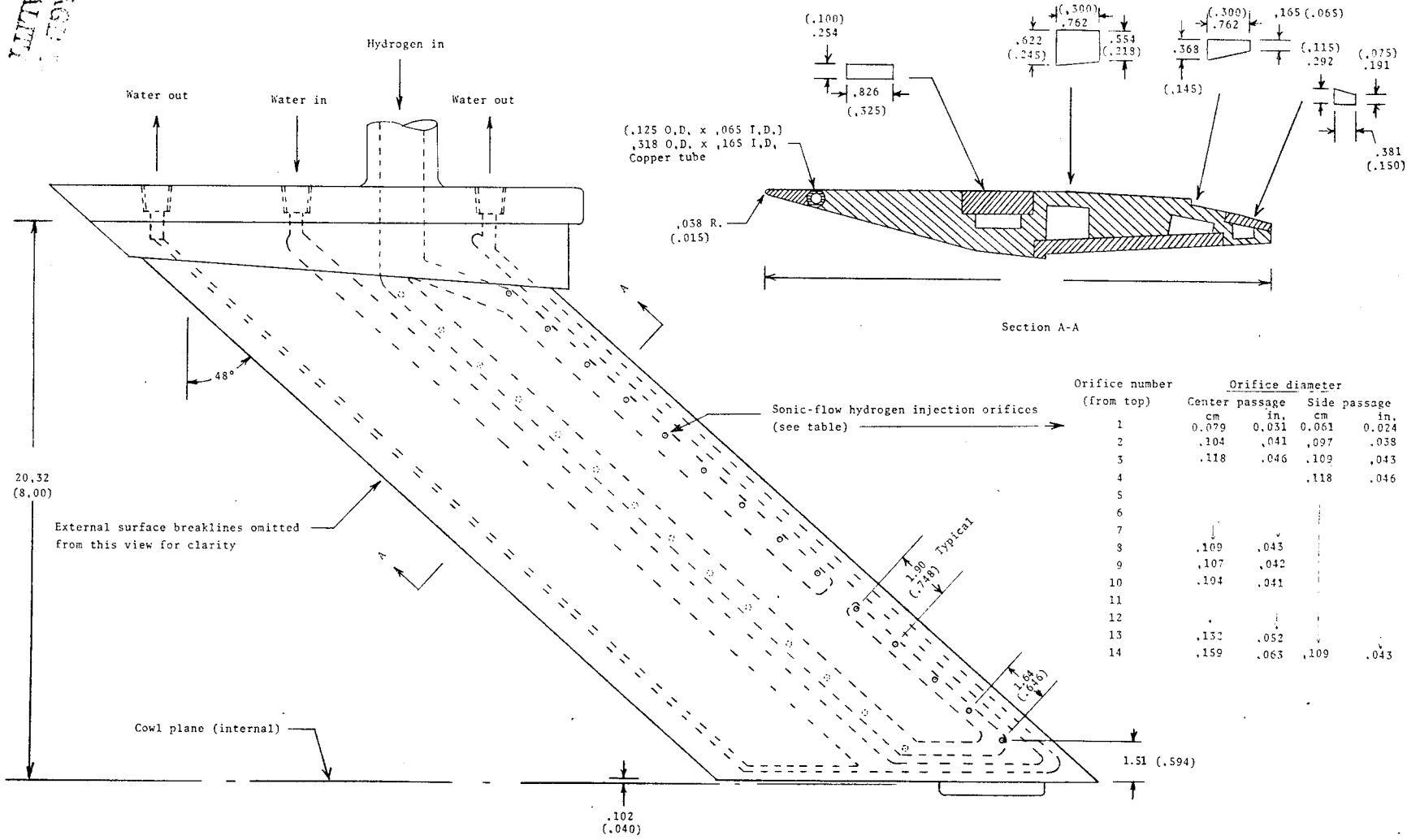
ORIGINAL PAGE IS
OF POOR QUALITY



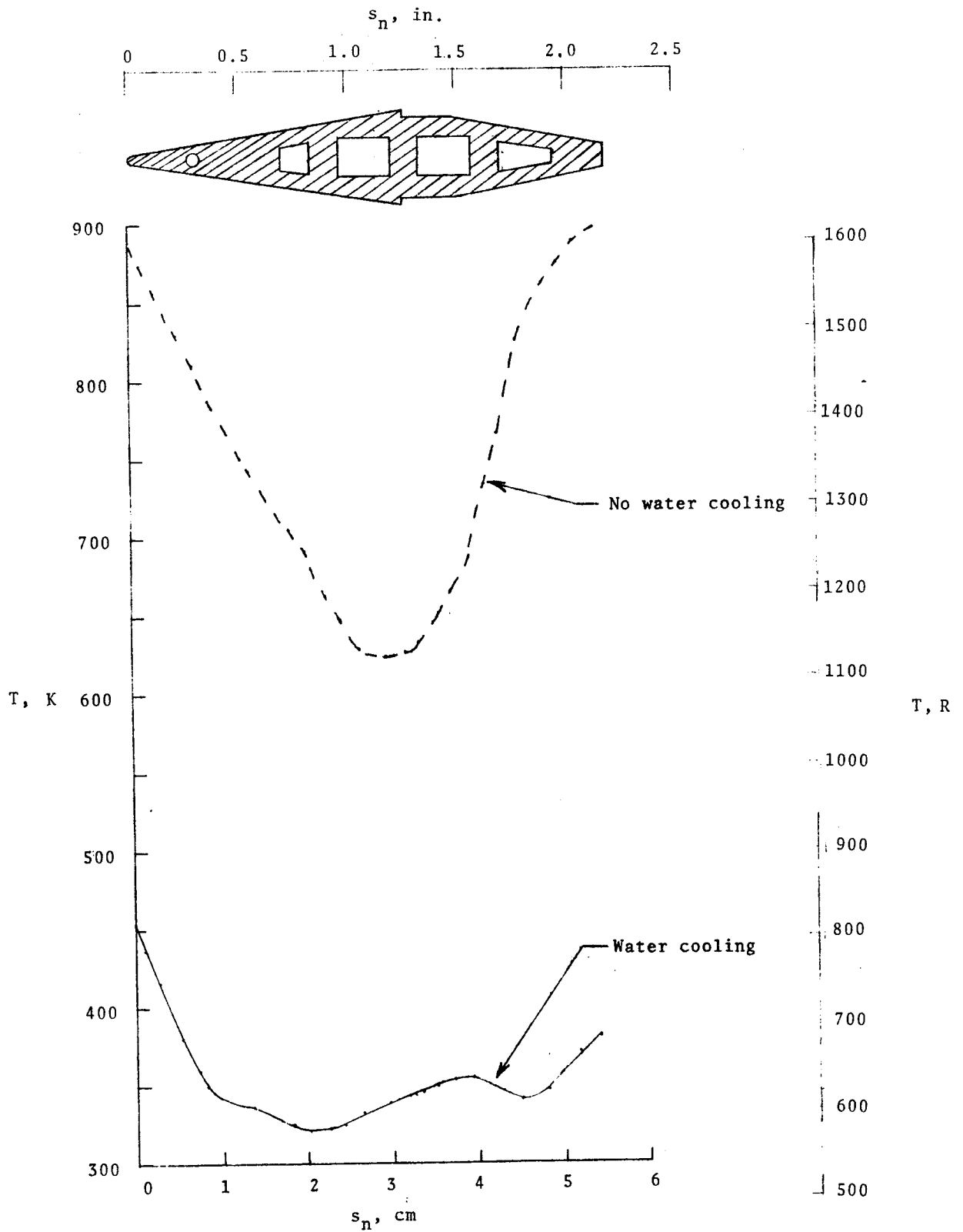
a.- Center fuel injection strut.

Figure 20.- Fuel and coolant routing for the scramjet model fuel injection struts.

ORIGINAL PAGE
OF POOR QUALITY

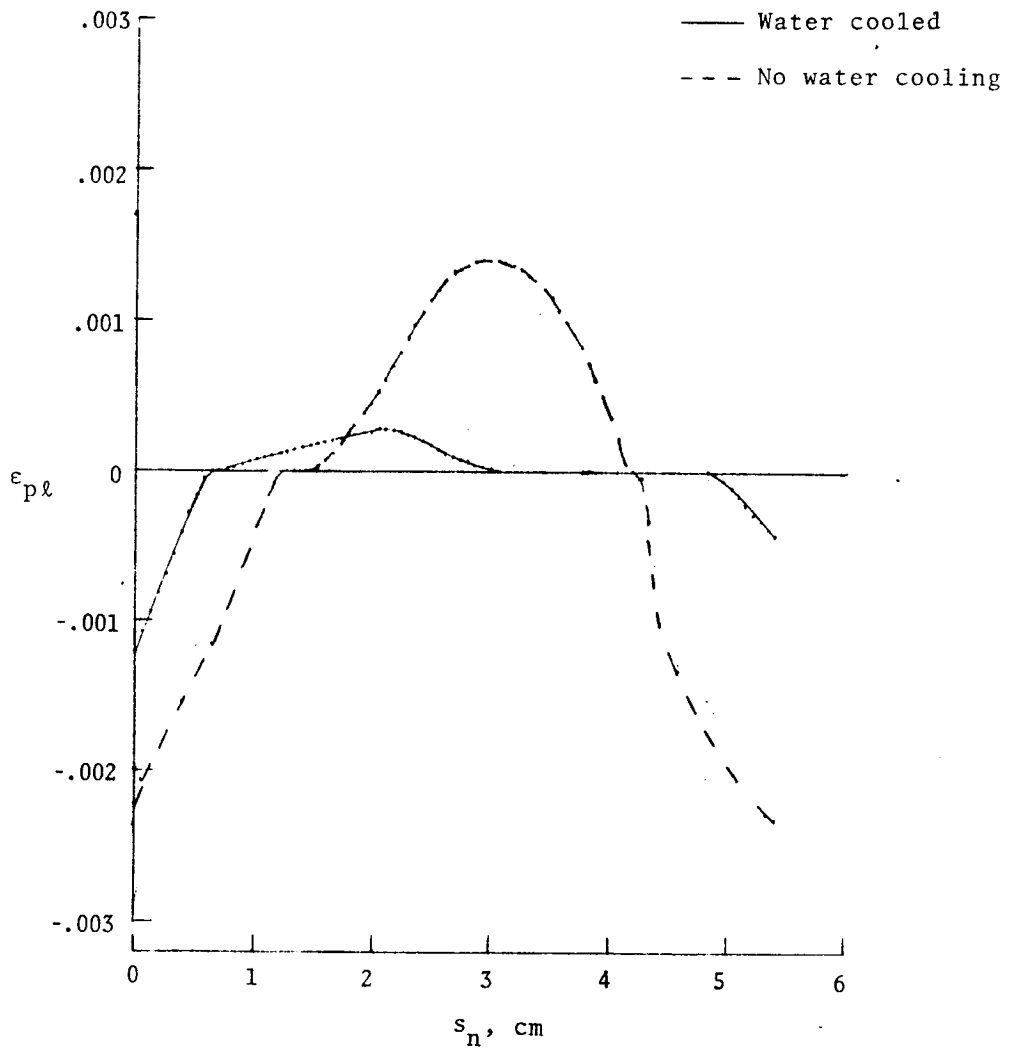
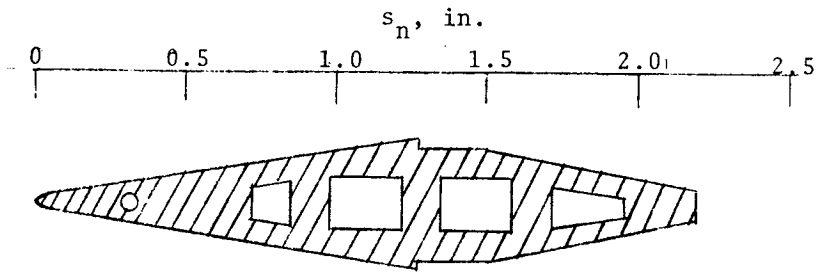


b.- Side fuel injection strut.
Figure 20.- Concluded.



a.- Temperature distribution.

Figure 21.- Calculated thermal condition of the center fuel injection strut after 30 seconds of testing.



b. - Plastic strain distribution.

Figure 21. - Concluded.

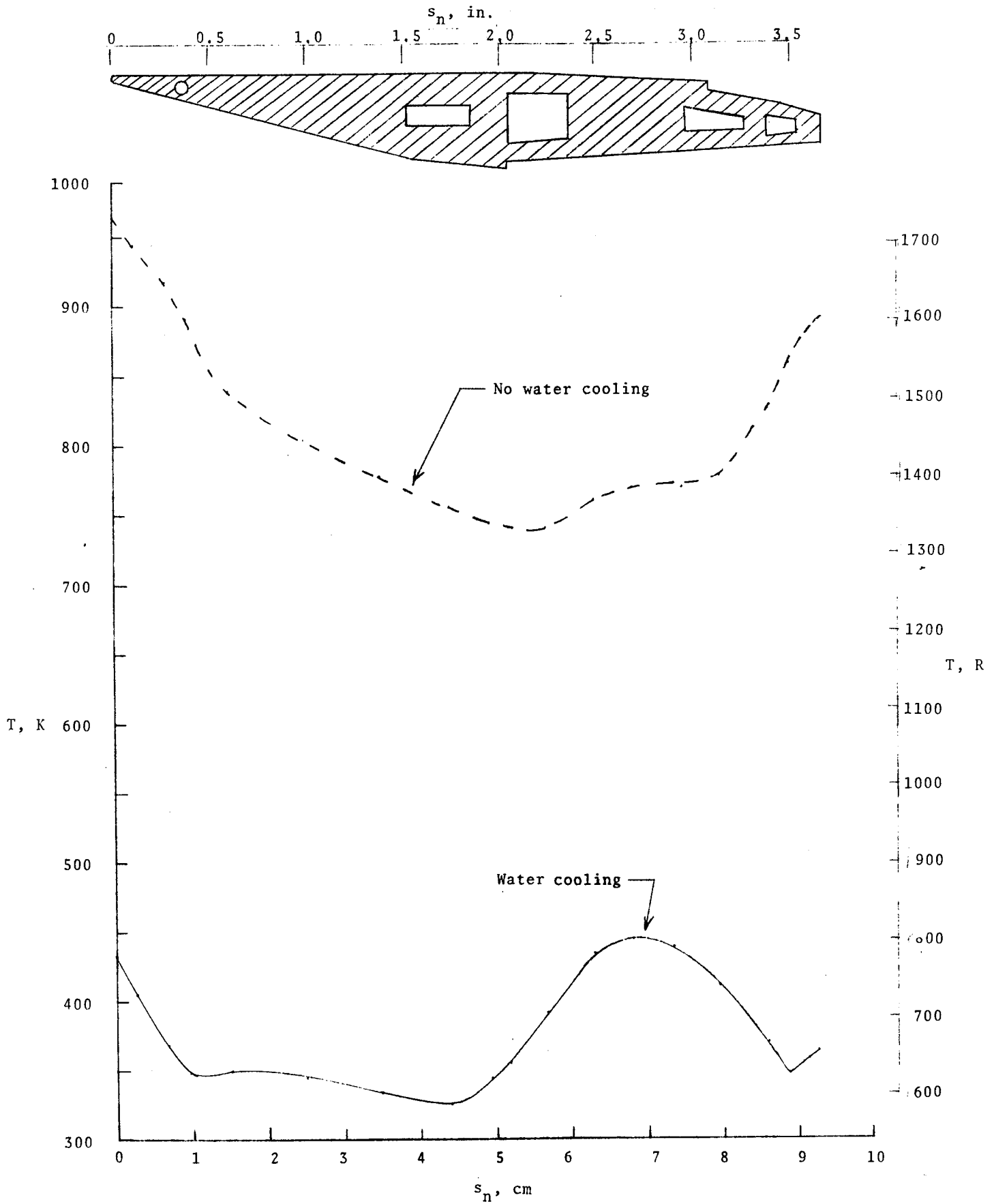
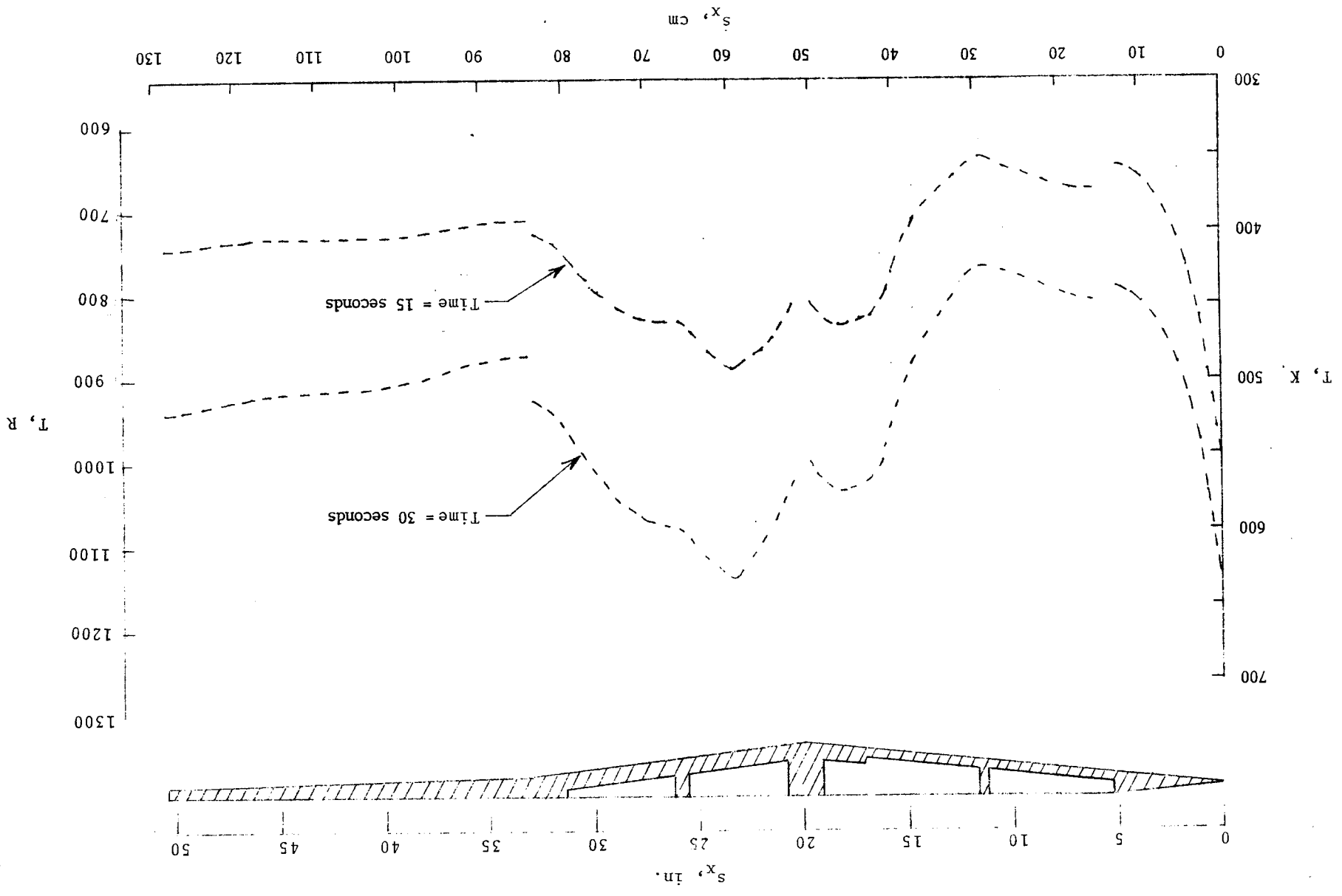


Figure 22.- Calculated temperature distribution along the side fuel injection strut after 30 seconds of testing.

Figure 23. Comparison of calculated sidewall temperature distributions with no water-cooling after 15 and 30 seconds of test time.



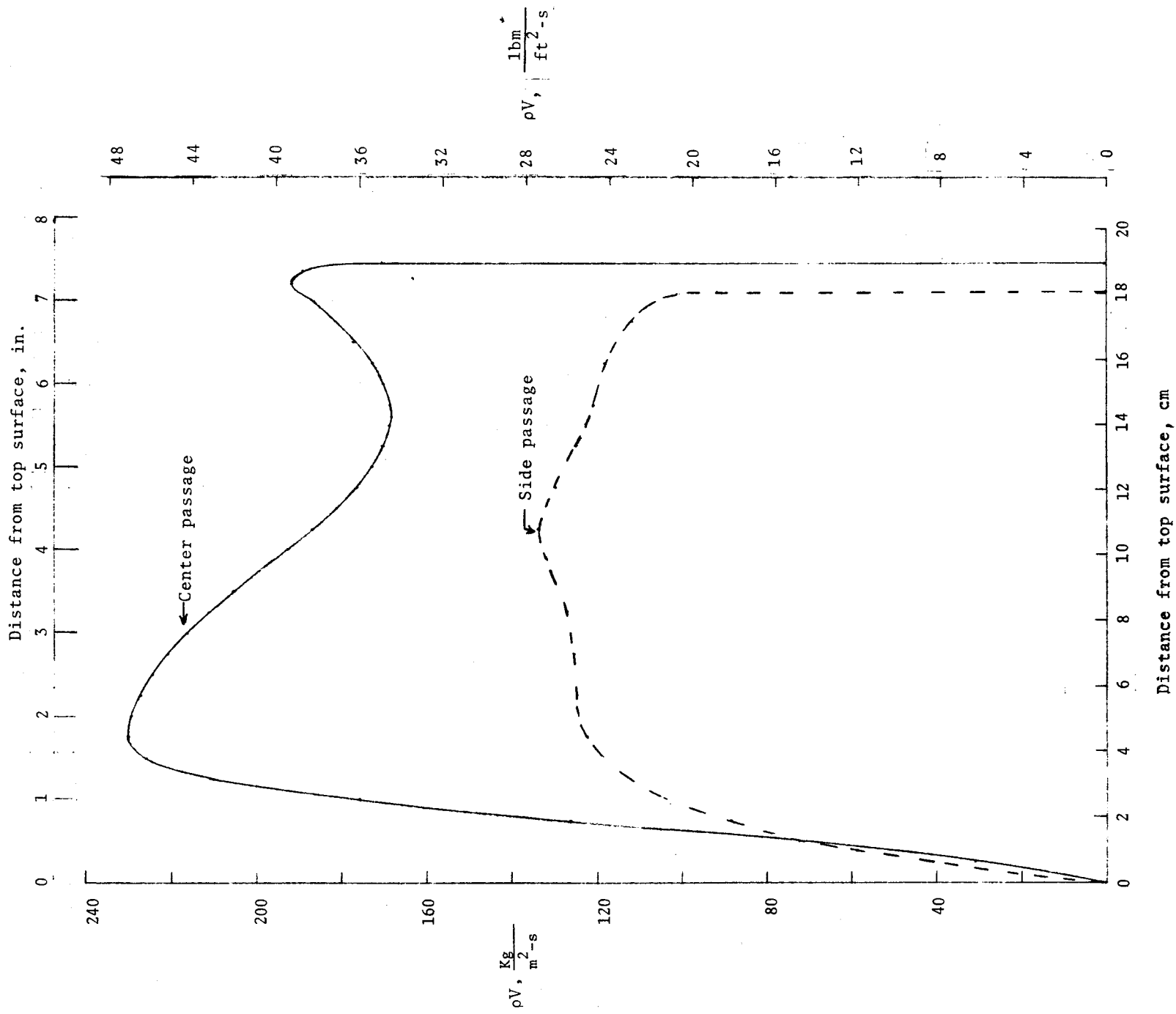


Figure 24. Air mass flow rate per unit area in strut fuel injection regions.

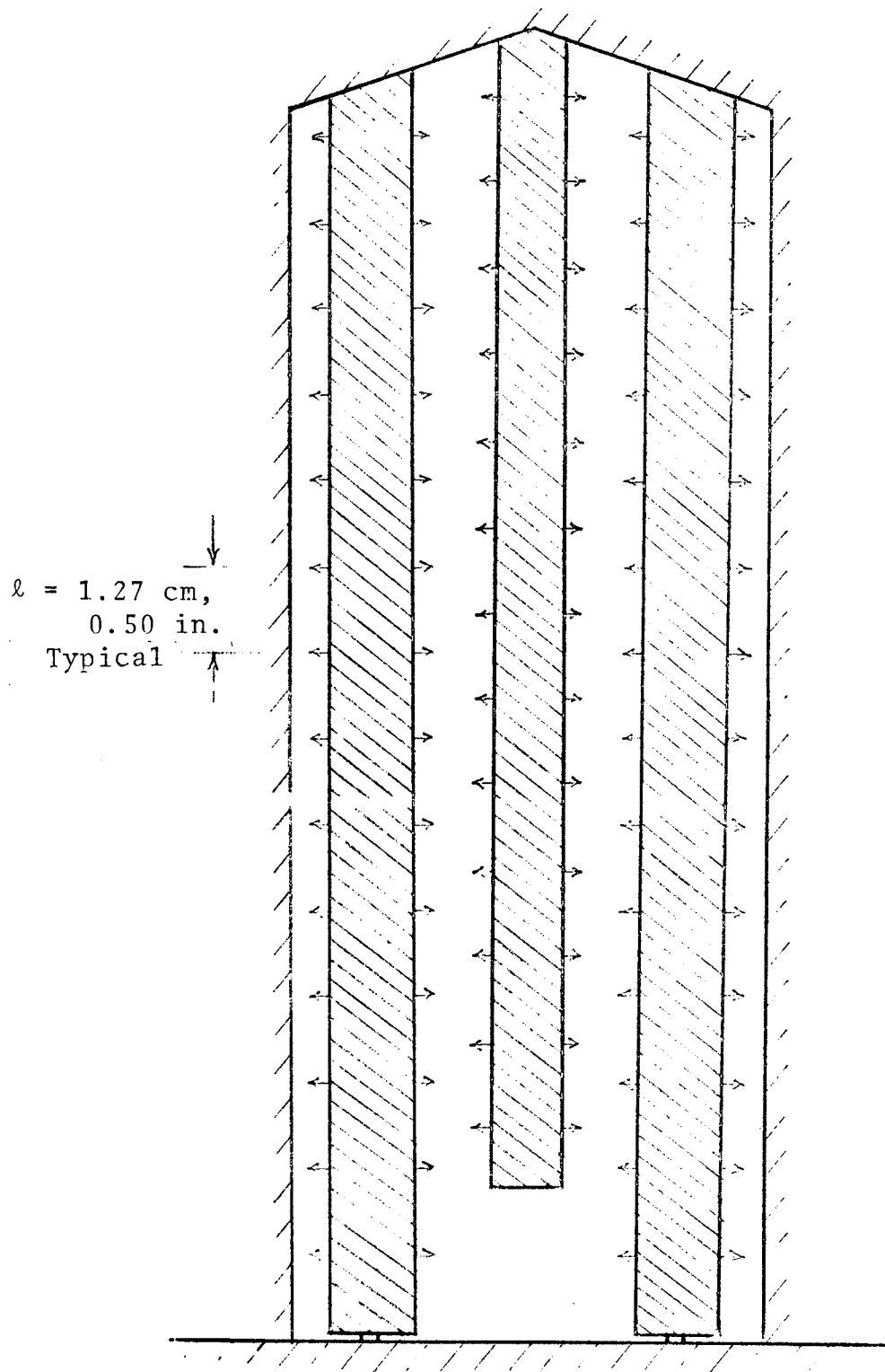


Figure 25. - Projected frontal view of scramjet throat region showing fuel injection distribution.